Measurement of neutrino oscillations in atmospheric neutrinos with the IceCube DeepCore detector

D i s s e r t a t i o n

zur Erlangung des akademischen Grades

d o c t o r r e r u m n a t u r a l i u m

(Dr. rer. nat.)

im Fach Physik

eingereicht an der

Mathematisch-Naturwissenschafltichen Fakultät I

der Humboldt-Universität zu Berlin

von

B.Sc. Juan Pablo Yáñez Garza

Präsident der Humboldt-Universität zu Berlin:

Prof. Dr. Jan-Hendrik Olbertz

Dekan der Mathematisch-Naturwissenschaftlichen Fakultät I:

Prof. Stefan Hecht, Ph.D.

Gutachter:
1. Prof. Dr. Hermann Kolanoski
2. Prof. Dr. Allan Halgren
3. Prof. Dr. Thomas Lohse

Tag der mündlichen Prüfung: 02.06.2014

Abstract

The study of neutrino oscillations is an active field of research. During the last couple of decades many experiments have measured the effects of oscillations, pushing the field from the discovery stage towards an era of precision and deeper understanding of the phenomenon. The IceCube Neutrino Observatory, with its low energy subarray, DeepCore, has the possibility of contributing to this field.

IceCube is a $1\,\mathrm{km}^3$ ice Cherenkov neutrino telescope buried deep in the Antarctic glacier. DeepCore, a region of denser instrumentation in the lower center of IceCube, permits the detection of neutrinos with energies as low as 10 GeV. Every year, thousands of atmospheric neutrinos around these energies leave a strong signature in DeepCore. Due to their energy and the distance they travel before being detected, these neutrinos can be used to measure the phenomenon of oscillations.

This work starts with a study of the potential of IceCube DeepCore to measure neutrino oscillations in different channels, from which the disappearance of ν_μ is chosen to move forward. It continues by describing a novel method for identifying Cherenkov photons that traveled without being scattered until detected (*direct photons*). These photons are used to reconstruct the incoming zenith angle of muon neutrinos. The total energy of the interacting neutrino is also estimated.

The data are used to populate a two-dimensional histogram with reconstructed energy and zenith angle in its axes, which is compared to histograms obtained from simulation sets with different oscillation parameters. The maximum likelihood method is used to determine which simulation set fits the data best.

In data taken in 343 days during 2011-2012, 1 487 neutrino candidates with an energy between 7 GeV and 100 GeV are found inside the DeepCore volume. Compared to the expectation from the atmospheric neutrino flux without oscillations, this corresponds to a deficit of about 500 muon neutrino events. The oscillation parameters that describe the data best are $\sin^2(2\theta_{23}) = 1\,(> 0.94$ at 68 % C.L.) and $|\Delta m^2_{32}| = 2.4^{+0.6}_{-0.4} \cdot 10^{-3}$ eV^2, which are in agreement with the results reported by other experiments. The simulation follows the data closely, resulting in a χ^2/d.o.f. of 48.8/54. The method and tools presented allow DeepCore to reach comparable precision with the current best results of on-going experiments once five years of data are collected.

Zusammenfassung

Neutrinooszillationen sind ein sehr aktives Forschungsfeld. In den letzten Jahrzehnten haben viele Experimente das Phänomen untersucht und sind inzwischen zu Präzisionsmessungen vorangeschritten. Mit seiner Niederenergieerweiterung DeepCore kann das IceCube-Experiment zu diesem Forschungsfeld beitragen.

IceCube ist ein $1\,\mathrm{km}^3$ großes Tscherenkow-Neutrino-Teleskop, welches das tiefe, antarktische Eis des Südpols als optisches Medium nutzt. DeepCore ist eine Erweiterung mit dichterer Instrumentierung im unteren Teil des IceCube-Teleskops. Diese dichte Instrumentierung ermöglicht den Nachweis von Neutrinos mit Energien ab einer Energieschwelle von etwa 10 GeV. Jedes Jahr werden Tausende von atmosphärischen Neutrinos oberhalb dieser Schwelle in DeepCore detektiert. Eine Bestimmung der Energie der Neutrinos und des durch sie zurückgelegten Weges durch die Erde ermöglicht die Messung von Neutrinooszillationen.

In dieser Arbeit werden zunächst die Möglichkeiten von DeepCore diskutiert, Oszillationen auf unterschiedliche Weise zu messen. Das Verschwinden von Myon-Neutrinos wird als erfolgsversprechender Prozess ausgewählt. Darauf folgt die Beschreibung einer Methode zur Identifizierung von Tscherenkow-Photonen, welche detektiert wurden, bevor sie gestreut wurden – sogenannte „direkte Photonen“. Mit Hilfe dieser Photonen kann der Zenitwinkel der Myon-Neutrinos bestimmmt werden. Auch die Energie der Neutrinos wird rekonstruiert.

Die Daten der ausgewählten Ereignisse werden in ein zweidimensionales Histogramm gefüllt, abhängig von ihren rekonstruierten Werten der Energie und des Zenitwinkels. Basierend auf Simulationen mit unterschiedlichen Oszillationsparametern werden ähnliche Histogramme erstellt. Die Maximum-Likelihood-Methode wird verwendet, um zu bestimmen, welche der Simulationen am besten mit den gemessenen Daten übereinstimmt.

In den Jahren 2011 und 2012 wurden innerhalb von 343 Tagen mit dieser Analyse 1 487 Neutrinokandidaten mit Energien zwischen 7 GeV und 100 GeV in DeepCore gefunden. Vergleicht man diese Zahl mit der erwarteten Zahl vom atmosphärischen Neutrinofluss ohne Oszillationen, so ergibt sich ein Defizit von etwa 500 Ereignissen. Am besten werden die Daten von den Oszillationsparametern $\sin^2(2\theta_{23}) = 1\,(> 0.94$ mit 68 % C.L.) und $|\Delta m^2_{32}| = 2.4^{+0.6}_{-0.4} \cdot 10^{-3}\,\mathrm{eV}^2$ beschrieben, was im Einklang mit anderen Experimenten steht. Simulation und Daten stimmen gut miteinander überein, was sich in einem χ^2 pro Freiheitsgrad von 48.8/54 zeigt. Es wird gezeigt, dass man bei Verwendung der vorgestellten Methoden und Werkzeuge in der Lage ist, mit fünf Jahren Daten von DeepCore eine mit den besten aktuellen Experimenten vergleichbare Genauigkeit zu erreichen.

Contents

1 Introduction

Neutrinos, together with photons, are the most abundant particles in the Universe. They are copiously produced in stars as well as inside living organisms, human beings included. However, because of their peculiar properties, their existence was only conceived when physicists started probing the phenomenon of radioactivity, discovered in the late 1800s [1, 2].

The first observations of *beta decay*, performed by Curie, Rutherford and Soddy among others, detected an unstable nucleus changing its constituents accompanied by the emission of one charged particle [2]. Meitner and Hahn subsequently measured the energy of the emitted charged particle, finding a continuous spectrum [3]. The observation was in conflict with the principle of energy-momentum conservation, which mandates that in any two body decay, the energy of the final state particles is constant. Pauli's conclusion was that a third particle had to be involved in the decay, which would allow for the observation of an energy spectrum instead of a single value[1] (see Fig. 1.1). The particle, which needed to be neutral otherwise it would have been observed, was shortly after named *neutrino* by Fermi. He made use of it to build the first attempt of a theory of beta decay [4].

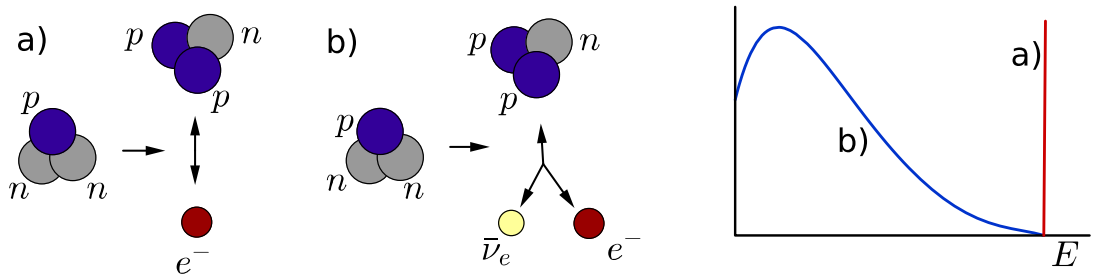

Figure 1.1: Beta decay of tritium into (a) an electron and helium and (b) into an electron, helium and a neutrino. The two energy spectra for the outgoing electron are compared.

Two decades after its prediction the neutrino was observed for the first time by Reines and Cowan [5]. Using a nuclear reactor as their source and water/cadmium chloride as their target they looked for signatures of antineutrino interactions with protons. The products of the reaction are a positron, which annihilates with the electrons of the medium producing back-to-back gamma-rays, and a free neutron, which can be captured by cadmium, emitting a single gamma-ray in the process,

$$\begin{aligned} p + \bar{\nu_e} &\rightarrow n + e^+ \\ e^+ e^- &\rightarrow \gamma\gamma \\ n + {}^{108}\mathrm{Cd} &\rightarrow {}^{109}\mathrm{Cd} + \gamma\,. \end{aligned} \tag{1.1}$$

The confirmation of the particle's existence was quickly followed by theoretical and experimental efforts to characterize its nature.

[1] Pauli made his proposal in an open letter directed to the attendants of a conference in Tübingen. An image of it can be found in http://www.library.ethz.ch/exhibit/pauli/neutrino_e.html

During the 1950s different attempts to directly measure the mass of the newly discovered particle found it to be compatible with zero, setting upper limits below the electron mass [6,7]. This motivated the hypothesis of a massless particle and theories started being built around this idea [8–10]. The theories of weak interactions that would become the foundations of the Standard Model of Particle Physics, those of Feynman and Gell-Mann [11], and Marshak and Sudarshan [12], contained massless neutrinos from the start.

Late in the same decade the discovery of oscillations in the neutral kaon system $K^0 \leftrightarrows \bar{K}^0$ prompted B. Pontecorvo to consider the same possibility for neutrinos, with oscillations between particle and antiparticle states $\nu \leftrightarrows \bar{\nu}$ [13,14]. He went as far as proposing oscillations into particles that could not be detected, i.e. sterile. In 1962 the existence of a new neutrino type was discovered [15], which motivated Maki, Nakagawa and Sakata to propose the existence of neutrino oscillations between flavor states that differ from the *true* neutrino states [16].

By the early 1970s Pontecorvo and Gribov developed phenomenological theories to describe neutrino mixing and oscillations in vacuum [17]. The main idea was that neutrinos, like other fundamental fermions, were massive. Also, the neutrinos made use of the possibility of states being mixed between physical representations, a freedom present in gauge theories. From these theories it already stands out that neutrino oscillations, if existent, would be essentially different from the ones in the kaon system: the mass differences of the neutrinos would be involved.

Experimental evidence of missing neutrinos came next. The Homestake experiment was the first to find a deficit of neutrinos upon measuring the Sun's flux and comparing it to the expectations from the Standard Solar Model [18]. Their findings were later confirmed by the SAGE [19], GALLEX/GNO [20], Super-Kamiokande [21] and SNO experiments [22]. After atmospheric neutrinos were detected in the mid-60s [23,24] experiments started using them to test the oscillations hypothesis. At the Neutrino Conference in 1998, Super-Kamiokande presented results on their atmospheric neutrinos measurements [25]. A deficit of muon neutrinos was found (see Fig. 1.2), which could be best explained by oscillations. Their findings were the first conclusive evidence for the existence of the phenomenon and its implications, mixing of massive neutrinos [25].

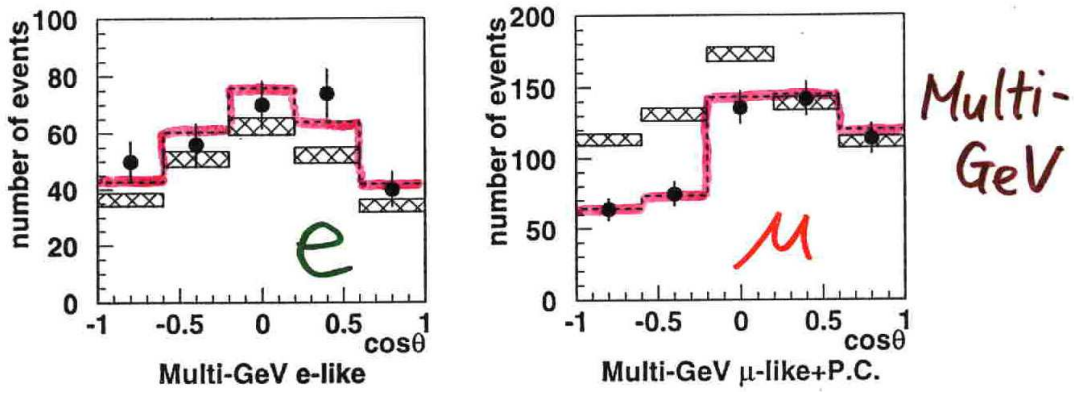

Figure 1.2: Neutrino oscillations results reported by Super-Kamiokande at the Neutrino'98 conference [25]. The zenith angle distributions for multi-GeV atmospheric electron and muon neutrino events are shown. Dots with error bars are data; histograms correspond to predictions without (shaded boxes) and with (dotted line) neutrino oscillations.

Mixed neutrino states can be accommodated in the original Standard Model as long as it is extended to account for the existence of neutrino masses. How the neutrino flavor states are mixed and how heavy the massive states are is not constrained. Like for the other fermions, these values can only be obtained from measurements.

With the discovery phase over, and confirmation of the existence of a third neutrino flavor [26], the field of neutrino oscillations saw the arrival of precision oscillation experiments, like MINOS, T2K, Borexino and Daya Bay, whose details are presented later. As the previous experiments, they used atmospheric, solar and reactor neutrinos, but also neutrinos from accelerator beams, a controlled source. Their results have confirmed the standard oscillations interpretation and improved the knowledge of the parameters involved. We know of the existence of three massive states, all of which mix, some very strongly, and that one of them has a rather different mass scale when compared with the others.

Because of the solid theoretical and experimental ground where oscillations stand, they are a potential tool for probing deeper into both the nature of the neutrino and the underlying structure of the Standard Model. However, getting to that point may require measurements with higher precision and confirmation of the universality of the oscillations hypothesis.

The work presented here is a measurement of the disappearance of atmospheric muon neutrinos with the IceCube DeepCore detector. Two more general problems are addressed in its development: a study of the possible measurements of neutrino oscillations that the detector can perform in different channels, and the development of reconstruction tools and an analysis method suitable for the experiment. One year of data are analyzed to retrieve the oscillation parameters that describe it best. Since the detector will acquire data for a period of, at least, ten times longer, projections for future sensitivity are also given.

Chapter 2 starts with a brief overview of the place of neutrinos in the original formulation of the Standard Model and how their interactions are described. The theory of neutrino oscillations is derived in Chapter 3, where the cases of propagation in vacuum and through matter are explored. In Chapter 4 selected experimental results on oscillations are presented. Chapter 5 is a discussion on how to conduct such a measurement with the IceCube detector, while Chapter 6 is dedicated to the details of how the neutrino events are reconstructed. The selection of the neutrino sample is dealt with in Chapter 7, including the fit of the neutrino oscillations model to the data. Results are presented and discussed in Chapter 8, leading to the summary and outlook contained in Chapter 9.

2 Neutrinos in the Standard Model

Most of the known phenomena in elementary particle physics are explained by the Standard Model. The fact that neutrinos have mass is, up to now, the only discovery that has been made beyond it. The Standard Model can, nevertheless, be expanded to account for the existence of neutrino masses, as long as the nature of the particle is given as an input.

In the following Chapter a very short introduction to the Standard Model is offered first, focusing on weak interactions and the role of neutrinos in the model. The concepts developed are then used to go into a more careful description of the neutrino properties. The neutrino-nucleon interactions which are relevant for this work ($E_\nu \geqslant 10\,\mathrm{GeV}$) are discussed last. Throughout this and the following chapters natural units are used ($\hbar = c = 1$).

2.1 The Standard Model of Particle Physics

The Standard Model of Particle Physics (SM) is a relativistic quantum field theory that describes the interactions between elementary particles[1]. In the model an interaction takes place when mediators are exchanged between matter particles, described by Dirac-type fermion fields. The mediators are vector bosons that correspond to the generators of the local symmetry group $SU(3) \otimes SU(2) \otimes U(1)$ upon which the SM is founded.

The number and properties of the vector bosons in the SM are fixed by its symmetries and by three *coupling constants*, one from each underlying group. The values of these constants have to be determined from experiments. Possible scalar bosons and fermions, on the other hand, have the only restriction that they should belong to a representation of the symmetry group; their number and properties are free. The original SM formulation postulates the existence of one scalar field, the Higgs, and twelve fermion fields. The representation of the fermion fields under each of the single symmetry groups that give rise to the Standard Model can be found in Table 2.1.

Table 2.1: Irreducible fermionic representations in the Standard Model: $(I_{SU(3)}, I_{SU(2)})_{U(1)}$. The subscripts R and L stand for right- and left-handed chirality. Paired fields explicitly show the $SU(2)$ structure. The superscript i corresponds to the $SU(3)$ group. Reproduced from [29].

$(\vec{1},\vec{2})_{-1}$	$(\vec{3},\vec{2})_{1/3}$	$(\vec{1},\vec{1})_{-2}$	$(\vec{3},\vec{1})_{4/3}$	$(\vec{3},\vec{1})_{-2/3}$
$\begin{pmatrix}\nu_e \\ e\end{pmatrix}_L$	$\begin{pmatrix}u^i \\ d^i\end{pmatrix}_L$	e_R	u^i_R	d^i_R
$\begin{pmatrix}\nu_\mu \\ \mu\end{pmatrix}_L$	$\begin{pmatrix}c^i \\ s^i\end{pmatrix}_L$	μ_R	c^i_R	s^i_R
$\begin{pmatrix}\nu_\tau \\ \tau\end{pmatrix}_L$	$\begin{pmatrix}t^i \\ b^i\end{pmatrix}_L$	τ_R	t^i_R	b^i_R

[1] The presentation of the Standard Model follows closely that of Griffiths [27] and Giunti [28].

2.1.1 Strong force

The $SU(3)$ group describes the strong force. Its conserved quantity is known as *color* and has eight generators to exchange it, the eight colored gluons. The gluons have the peculiarity that, unlike the mediators of the other forces in the SM, they can interact among themselves.

Another property of the strong force is that it only permits colored particles to exist inside bound states, and not in isolation. This phenomenon is known as color confinement. The strength of the strong force does not drop off when the distance between the colored particles increases, but rather when it decreases. When the particles are close together, as the quarks in a proton are, the force has little effect on them and they behave as if they were free within their confinement. This effect is known as asymptotic freedom.

Neutrinos do not experience the strong force; they have a unique representation under the $SU(3)$ group, as shown in Table 2.1. However, neutrinos can interact with nucleons, where the effects mentioned take place. These interactions are introduced at the end of this Chapter, and are used all throughout this work.

2.1.2 Electroweak force

In the SM the direct product $SU(2)\otimes U(1)$ describes electroweak interactions. Independently, $SU(2)$ conserves *weak isospin* and has three generators, $W^{\pm,0}$. This group has a peculiar structure, with the mediators interacting with the different pieces of a fermion field unevenly.

A fermion field ψ can be specified in terms of its chiral components by using the operator

$$\frac{1}{2}\left(1 \pm \gamma^5\right)\,\psi\,, \tag{2.1}$$

where γ^5 is the product of the four Dirac matrices. The fields that result from using different signs are known as *right-handed* and *left-handed*. In this chiral representation the distinct behavior of the $SU(2)$ group of the SM can be observed best: only the left-handed component of fermion fields are affected nontrivially.

The other group involved, $U(1)$, conserves *weak hypercharge* and has only one mediator, B. In the most general case, the two neutral generators of the product of $SU(2)\otimes U(1)$ are a linear combination of B and W^0. The degree of mixing between them is quantified by the *weak mixing angle*, θ_W.

The symmetry breaking Higgs field

The existence of a scalar field known as the *Higgs field* induces a mechanism that gives mass to the charged $W^{\pm}$ and to one of the mixed neutral states, labeled Z^0. The remaining mixed state, the photon γ, is left massless. The measured values for the masses of these mediators are shown in Table 2.2.

Table 2.2: Properties of the mediators of the electromagnetic and weak forces [30]. The zero mass of the photon is a property of the SM; experimental limits in parentheses.

Mediator	Q (e)	Mass (GeV)
$W^{\pm}$	± 1	80.385 ± 0.015
Z^0	0	91.1876 ± 0.0021
γ	0	$0\ \left(< 10^{-27}\right)$

Massive vector bosons break the symmetry of the electroweak force. Massive mediators have a limited range of action, which makes their exchange rather different from the one of the massless photon. The outcome is that the electroweak force is effectively divided into two seemingly disconnected forces:

- the electromagnetic force, whose mediator is γ and exactly conserves *electric* charge, and
- the weak force, whose mediators are the $W^{\pm}$ and the Z^0, and has been observed to conserve the *lepton number*.

The fact that the weak interaction conserves lepton number is an empirical one. Since the symmetry is lost because of its massive mediators, an exact conservation law cannot be derived. For the case of the photon the situation is different. Since the particle remains massless the symmetry of its group is not lost and an exact conservation law follows.

Another consequence of the existence of the Higgs field is the appearance of masses in the fermion sector, whose best measured values can be found in Table 2.3. By writing the Lagrangian for interactions between leptons and the Higgs field in the chiral representation the mass term can be understood as the coupling between the left- and right-handed components of a fermion field,

$$\mathcal{L}_{H,l} = -\sum_{\alpha} m_{\alpha} \bar{\psi}_{\alpha,L} \psi_{\alpha,R} + \text{h.c.}\,, \tag{2.2}$$

where α stands for any lepton flavor.

Table 2.3: List of fundamental and measured properties of the lepton fields in the SM. The conserved quantities after symmetry breaking are shown. Neutrinos in the SM have no mass; the values shown come from direct experimental searches that used the indicated flavor. Compiled from [30].

Particle	$Q\,(e)$	L_e	L_μ	L_τ	Mass (MeV)
$e^{\pm}$	±1	±1	0	0	$0.510998928 \pm (0.011 \cdot 10^{-6})$
$\mu^{\pm}$	±1	0	±1	0	$105.6583715 \pm (3.5 \cdot 10^{-6})$
$\tau^{\pm}$	±1	0	0	±1	1776.82 ± 0.16
$\nu_e(\bar{\nu}_e)$	0	±1	0	0	$< 2 \cdot 10^{-6}$
$\nu_\mu(\bar{\nu}_\mu)$	0	0	±1	0	$< 190 \cdot 10^{-3}$
$\nu_\tau(\bar{\nu}_\tau)$	0	0	0	±1	< 18.2

The Lagrangian of weak interactions

The Lagrangian for the weak interaction can be written down in terms of the vector boson that is exchanged. The term involving the $W^{\pm}$ is known as charged current (CC), and has the form

$$\mathcal{L}_{CC} = -\frac{g}{\sqrt{2}} \sum_{l=e,\mu,\tau} (\bar{\nu}_{lL} \gamma^{\mu} e_{lL} W^{+}_{\mu} + \bar{e}_{lL} \gamma^{\mu} \nu_{lL} W^{-}_{\mu}), \tag{2.3}$$

where the subscript L denotes again the left-handed chiral components of the fermion fields and g determines the strength of the coupling. The two terms inside the parenthesis transform charged leptons e_l into neutrinos of the same flavor ν_l and vice versa. A process mediated by

Z^0 exchange is known as neutral current (NC) and the interaction Lagrangian has the form,

$$\mathcal{L}_{NC} = -\frac{g}{2c_W^2} \sum_{l=e,\mu,\tau} \left(\bar{\nu}_{lL}\gamma^\mu \nu_{lL} + (2s_W^2 - 1)\,\bar{e}_L\gamma^\mu e_L + 2s_W^2\,\bar{e}_R\gamma^\mu e_R\right) Z_\mu^0, \tag{2.4}$$

where s_W^2 and c_W^2 are the sine and cosine squared of the weak mixing angle θ_W and the subscript R denotes the right-handed chiral component, which was missing in the CC part[1].

Note that the CC Lagrangian only contains left-handed particles; the $W^\pm$ mediators retain the chiral properties of the $SU(2)$ group. In contrast, the NC Lagrangian exhibits the mixing $SU(2)\otimes U(1)$ by coupling right-handed particles. The coupling has a different strength than for left-handed particles, which depends on the value of the electroweak mixing angle.

Another feature of the weak Lagrangian is that fermions have the freedom to enter the interaction as linear combinations of mass eigenstates. In other words, a fermion in the flavor basis can be identified with a mixture of the states with definite masses, but does not need to have a definite mass itself. The flavor of charged leptons is uniquely defined by their masses, so such a mixture cannot take place for them. Quarks, on the other hand, have been observed to enter weak interactions in this fashion. For SM neutrinos this possibility does not exist. Being massless, they exclusively have the flavor representation.

2.2 Neutrino properties

We now turn to the neutrino and its properties. Some were already introduced in order to formulate the weak Lagrangian; they are revisited in this Section, making reference to their experimental motivation. The explanation follows closely that of [29].

2.2.1 Quantum numbers

A neutrino is an electrically neutral spin $\frac{1}{2}$ fermion. The particle carries the empirically defined lepton number, resulting in three different flavor states, ν_e, ν_μ and ν_τ, which interact weakly (see Table 2.3). Since the particle has no color information it is unaffected by the complicated dynamics of the strong force.

The flavor of a neutrino is defined as the one of the charged lepton to which it couples in a $W^\pm$ exchange (CC interaction, see Eq. 2.3). It follows that no flavor can be assigned for a neutrino either in propagation or interacting via Z^0 exchange.

2.2.2 Number of families

The flavor independence of the NC Lagragian (Eq. 2.4) allows determining the number of neutrino families that exist in Nature from the study of Z^0 decays. A Z^0 can decay into hadrons, with decay width Γ_h, and neutral or charged leptons, with decay widths Γ_ν or Γ_l, respectively. Every particle-antiparticle lepton pair opens a new decay channel, so the probability of the process scales with the number of families.

As the neutrinos can escape the detector unobserved, the width Γ_ν cannot be measured directly. However, this "invisible decay" Γ_{inv} can be derived from the relation between Γ_l

[1] The CC and NC weak Lagrangians given in Eqs. 2.3, 2.4 are in the chiral representation. If written explicitly, terms of the form $\bar{\psi}\gamma^5\frac{1}{2}\left(1 \pm \gamma^5\right)\psi$ appear. The term $\bar{\psi}\gamma^\mu\psi$ is a vector, while $\bar{\psi}\gamma^\mu\gamma^5\psi$ is an axial-vector. Because of this feature the theory was first known as $(V - A)$ and the couplings were given in terms of the objects they affected, as g_V and g_A.

and the total hadronic cross-section σ_h, both of which can be measured[1]. This results in a prediction for the number of neutrino families of

$$N_\nu = \frac{\Gamma_{\text{inv}}}{\Gamma_l} \left(\frac{\Gamma_l}{\Gamma_\nu} \right)_{\text{SM}} , \tag{2.5}$$

where the ratio Γ_l/Γ_ν as calculated from the SM is used.

Figure 2.1 shows the result of precision measurements of the Z^0 decay into hadrons at the LEP e^+e^- collider. The expectations for different number of neutrino families are also given. The best fit to the data is obtained with $N_\nu = 2.9840 \pm 0.0082$ [31], in agreement with the three lepton families discovered so far. This result, although stringent, only applies for neutrinos with a mass below half of the Z^0 mass (often called "light") which interact weakly. Heavy neutrino-like particles with properties outside the SM are not excluded by it.

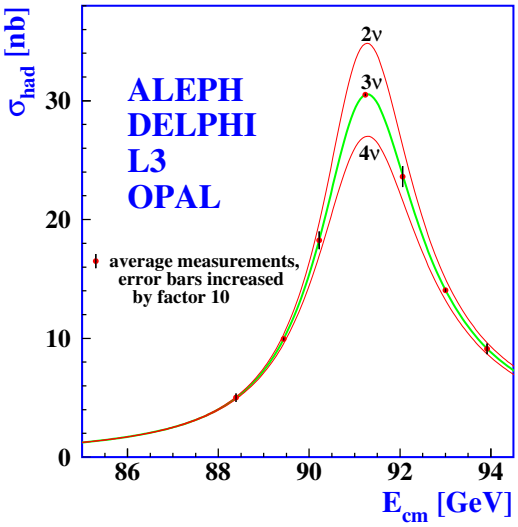

Figure 2.1: Invisible decay width of the Z^0 boson measured at LEP. The prediction for 3 neutrino families is shown in green. Expectation for 2 and 4 families in red. Taken from [31].

2.2.3 Chirality, helicity and mass

The relation between the chirality of a particle and its mass in the SM can be understood by the term shown in Eq. 2.2, where the two chiral components of a fermion field are coupled by their mass term. It follows that a massless particle can be described by a single chiral component. Simultaneously, a massive particle needs both chiral components to be fully described.

The SM only postulates the existence of left-handed neutrinos. They are, then, masless particles. The reason for this comes from the experimental results on mass and chirality obtained by the time the model was proposed.

Neutrino helicity

The helicity of a particle is defined as the projection of its spin $\vec{s}$ onto its momentum $\vec{p}$, as

$$h = \frac{\vec{s} \cdot \vec{p}}{|\vec{s} \cdot \vec{p}|} . \tag{2.6}$$

[1] The full derivation of the formulas can be found, together with the LEP results, in [31].

In general, the quantity is not invariant, as the sign of h changes when an observer overtakes the particle. However, for massless particles, which travel at the speed of light and cannot be overtaken by an observer, the helicity is conserved and equal to the particle's chirality. The equality is approximately fulfilled by highly relativistic particles.

The helicity of the neutrino was first measured by Goldhaber *et al.* in 1957 [32]. The experiment used electron capture in an unpolarized nucleus of ^{152}Eu, which leads to the reaction

$$^{152}\mathrm{Eu} + e^- \rightarrow ^{152}\mathrm{Sm}^* + \nu_e \rightarrow ^{152}\mathrm{Sm} + \gamma + \nu_e\,. \tag{2.7}$$

As ^{152}Eu has $J = 0$, the angular momentum of the initial state is given by the electron spin, of $\pm\frac{1}{2}$. When the photon and the neutrino are emitted *back-to-back*, the total angular momentum of the system can be obtained by the sum of the polarization of the photon and the spin of the neutrino, which has to be equal to the total angular momentum of the initial state. It follows that measuring the photon polarization also gives the neutrino spin, and since the sign of the neutrino momentum is known, the helicity can also be obtained.

The outcome of the experiment was a unique polarization for the photons, which in turn means a helicity for the neutrinos of $-\frac{1}{2}$. Only left-handed particles were observed, therefore massless. By *CP* invariance, the helicity of antineutrinos is $\frac{1}{2}$.

Neutrino mass

The conclusion from helicity measurements that neutrinos are massless is in agreement with the attempts to measure the neutrino mass directly, which have not been successful to date. The current best limit comes from the measurement of the tail of the energy spectrum of the outgoing electron in tritium β decay,

$$\mathrm{H}^3 \rightarrow {}^3\mathrm{He} + e^- + \bar{\nu}_e\,. \tag{2.8}$$

The maximum energy that can be given to the electron depends on the mass of the neutrino that accompanies the process (see in Fig. 2.2). By measuring this spectrum, experiments have placed limits on the mass of the neutrino produced in this specific decay. The most stringent ones come from the Mainz [33] and Troitsk [34] groups:

$$m_{\beta\nu} < 2.2\,\mathrm{eV}\ \text{(Mainz)}, \quad m_{\beta\nu} < 2.1\,\mathrm{eV}\ \text{(Troitsk)}. \tag{2.9}$$

The KATRIN experiment, currently under construction, will perform the same measurement, but its design is expected to reach a sensitivity of 200 meV [35].

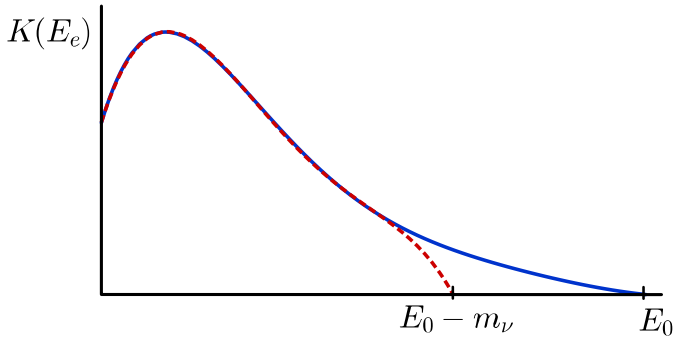

Figure 2.2: Energy spectrum of the electron emitted in β decay. Both the cases of massive (dotted) and massless neutrinos (solid) are shown.

The mass of the neutrino can also be studied indirectly from cosmological data, such as the distribution of galaxies. The results, however, depend on the details of the model used to interpret the data. Because of this, they are not discussed in this work. The curious reader is encouraged to have a look at [36].

2.3 Neutrino interactions with matter

Neutrino interactions are successfully described by the Standard Model. However, the complexity of the possible targets can complicate the problem, making a unified treatment difficult. Because of this it is convenient to study the interactions on individual regions of the parameter space, where simplifications can be carried out. In this Section we focus on CC interactions at neutrino energies of $\mathcal{O}(\text{GeV})$ (laboratory frame), following closely the review work from [28] and [37]. These interactions are the ones of interest for this work, where a neutrino sample with $E_\nu \geqslant 10\,\text{GeV}$ is analyzed. Neutral currents are shortly mentioned.

The dominant interaction of GeV neutrinos with normal matter is neutrino-nucleon scattering. Nucleons, i.e. protons and neutrons, are composite objects made out of quarks. For the weak force, quarks and leptons behave the same way. This means that by making the appropiate substitutions ($\nu, e \to q$'s), the Lagrangians in Eqs. 2.3 and 2.4 can also be used to describe the dynamics of neutrino-quark interactions.

2.3.1 CC Neutrino-quark scattering

The form of the cross-section for neutrino-quark scattering depends on the spin configuration of the initial states. Since neutrinos and antineutrinos have unique helicities in the SM (see Sec. 2.2.3), the cross-section can be divided in particle-particle and particle-antiparticle interactions.

Particle-particle interaction

Take the particular process

$$\nu_\mu + q_i \to \mu^- + q_f \tag{2.10}$$

depicted in Fig. 2.3, where a muon neutrino with four-momentum p_ν scatters off a free quark with four-momentum p_{q_i} at rest in the laboratory frame. The interaction produces a muon and a different quark, with four-momenta k_μ and k_{q_f}, respectively. From here it is useful to define variables that are invariant under Lorentz transformations:

$$s \equiv (p_\nu + p_{q_i})^2 \quad \text{(center-of-mass energy)}, \tag{2.11}$$

$$-Q^2 = q^2 \equiv (p_\nu - k_\mu)^2 \quad \text{(momentum transfer)}, \tag{2.12}$$

$$y \equiv \frac{p_e \cdot q}{p_e \cdot p_\nu} \quad \text{(inelasticity)}. \tag{2.13}$$

For the cases when $|q^2| \ll M_W^2$, q^2 can be ignored, which we do here for simplicity. Also, we assume that $E_\nu \gg m_\mu$ in order to avoid production threshold effects. Under these conditions, the differential and total cross-sections as a function of the center of mass energy s are given by

$$\frac{d\sigma^\nu}{d\Omega} = \frac{G_F^2 s}{4\pi^2}, \qquad \sigma^\nu = \frac{G_F^2 s}{\pi}, \tag{2.14}$$

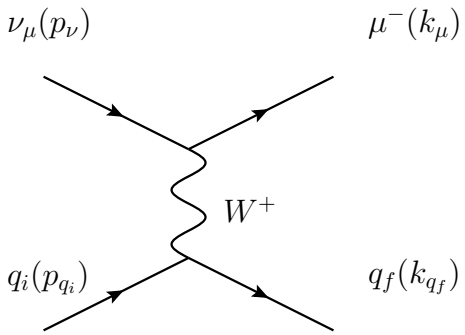

Figure 2.3: Feynman diagram of charged current neutrino-quark scattering.

where the coupling strength is dictated by the Fermi constant G_F:

$$G_F = \frac{g^2}{4\sqrt{2}M_W^2} = 1.1663788(7) \times 10^{-5}\,\text{GeV}^{-2}. \tag{2.15}$$

Note that the cross-section grows linearly with the center-of-mass energy. In the laboratory frame, with the quark at rest, the cross-section depends linearly on the neutrino energy. This is a general feature of neutrino interactions. Also, the cross-section has no dependence on the scattering angle θ^* between ν_μ and μ^-. In the center-of-mass frame the initial state has vanishing angular momentum, and by helicity conservation, so does the final state. Since the angular momentum is always zero, all scattering angles are equally likely.

Particle-antiparticle interaction

Take a similar process to that of 2.10, but with an antineutrino in the initial state,

$$\bar{\nu}_\mu + q_i \to \mu^+ + q_f\,. \tag{2.16}$$

The particles now have mixed helicities, and an extra factor of $(1+\cos\theta^*)^2$ enters the cross-section. The appearance of this dependence is explained in Fig. 2.4, where the component of total spin along the axis defined by the neutrino momentum is equal to +1 for the initial state. The same total spin component for the final state depends on the scattering angle, and can take any value between [-1, +1]. Since angular momentum has to be conserved, the configuration with the lepton produced in the opposite direction as the incoming neutrino, with an angular momentum of -1, is supressed.

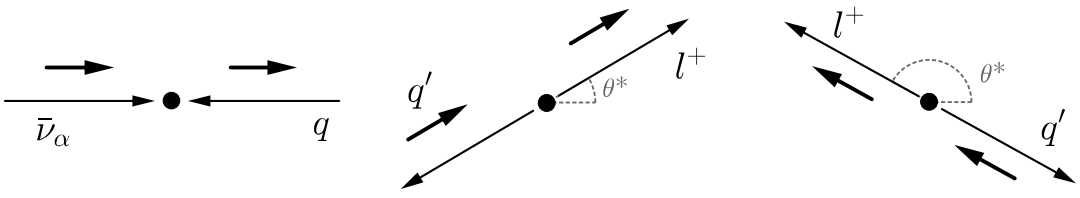

(a) Initial state **(b)** Final state **(c)** Final state

Figure 2.4: Configuration of the initial state of the process in Eq. 2.16 in the center-of-mass frame in (a). The thin and thick arrows represent momentum and spin, respectively. The angular momentum component along the neutrino direction is equal to +1. Possible final states in the same process for different angles θ^* shown in (b) and (c).

Note that the scattering angle θ^* and the y variable defined in 2.13 are connected. In the center-of-mass frame $y = (1-\cos\theta^*)/2$, while in the laboratory frame $y = 1-E_l/E_\nu$, which is the fraction of the energy transferred to the outgoing quark. The cross-sections of the mixed helicity case can be written as a function of the angle or y, but y has the advantage of being an observable even if the neutrino direction is not known.

The differential and total cross-sections, as function of θ^* and y, are then

$$\frac{d\sigma^{\bar{\nu}}}{d\Omega} = \frac{G_F^2 s}{16\pi^2}(1+\cos\theta^*)^2, \quad \frac{d\sigma^{\bar{\nu}}}{dy} = \frac{G_F^2 s}{\pi}(1-y)^2, \\ \sigma^{\bar{\nu}} = \frac{G_F^2 s}{3\pi}. \tag{2.17}$$

Comparing the total cross-section in Eq. 2.14 with the result above gives a ratio $\sigma^{\nu}/\sigma^{\bar{\nu}} = 3$. The suppression is entirely due to the helicities of the states involved.

Neutrino-quark interactions are described by one of the two exchanges described. To calculate interactions with nucleons, one needs to sum the specific scattering amplitudes for different processes. However, thus far we have assumed that the particles involved are free, which is not the case for quarks in nature. Only for high enough neutrino energies, discussed in the next Section, such approximation is valid.

2.3.2 CC Deep Inelastic Scattering (DIS)

A very energetic neutrino can resolve the structure of a nucleon and interact with a single quark (see Fig. 2.5). The process is known as "Deep Inelastic Scattering" (DIS), and is written as

$$\overset{(-)}{\nu}_l + N \to l^{\pm} + X\,, \tag{2.18}$$

where N denotes the target nucleon and X any set of final state hadrons. The four-momenta vectors of the neutrino, charged lepton, nucleon and the sum of the final state hadrons are p_ν, p_l, k_N and k_X respectively. The variables defined in 2.13 can be used to describe these processes, given that the subscripts are appropriately changed. An additional invariant quantity can be defined to simplify the calculations:

$$x \equiv \frac{Q^2}{s - m_N^2}. \tag{2.19}$$

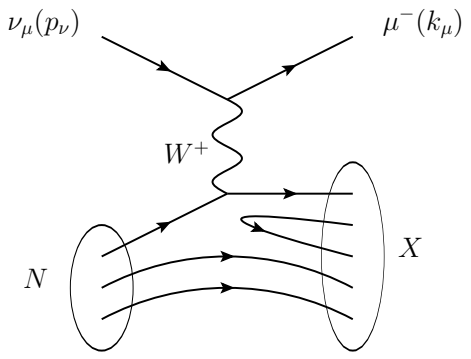

Figure 2.5: Feynman diagram of CC neutrino-nucleon deep inelastic scattering.

The DIS regime is realized when three conditions are met,

$$\begin{aligned} Q^2 &\gg m_N^2, \\ p_N{\cdot}q &\gg m_N^2, \quad \text{and} \\ s &\gg m_N^2. \end{aligned} \tag{2.20}$$

The first two demand a large momentum transfer and the third requires the center-of-mass energy of the process to be large with respect to the nucleon mass of about 1 GeV. For calculating an interaction probability it is necessary to know the internal structure of the nucleon and the different cross-sections for the possible neutrino-quark interactions.

Nucleon structure

The interpretation of DIS processes makes use of the *quark-parton* model of hadrons for understanding their internal configuration. In this model a nucleon is composed by three valence quarks and a sea of gluons and quark-antiquark pairs. A neutrino can interact with any of these quarks; all of these possibilities have to be computed. Each elementary process contributes according to the probability density $f_{q_i}^N(x)$ of finding the quark q_i in question, information encoded in the *parton distribution functions* (PDF) of the nucleon[1]. Assuming that the PDFs are known, the interaction probability can be calculated by convoluting them with the cross-sections in Eqs. 2.14 and 2.17.

The possible interactions for neutrinos and antineutrinos are:

$$\begin{aligned} &\text{(i)} \quad \nu_l + q_{d,s,b} \to l^- + q_{u,c,t}\,, \qquad \text{(iii)} \quad \nu_l + q_{\bar{u},\bar{c},\bar{t}} \to l^- + q_{\bar{d},\bar{s},\bar{b}}\,, \\ &\text{(ii)} \quad \bar{\nu}_l + q_{\bar{d},\bar{s},\bar{b}} \to l^+ + q_{\bar{u},\bar{c},\bar{t}}\,, \qquad \text{(iv)} \quad \bar{\nu}_l + q_{u,c,t} \to l^+ + q_{d,s,b}\,. \end{aligned} \tag{2.21}$$

Since we have been ignoring the masses of the leptons, i.e. using the extreme relativistic limit, these processes can be grouped in two elementary diagrams: one where all the particles have the same helicity, processes (i) and (ii), and one where the helicity at each vertex is different, processes (iii) and (iv).

DIS cross-section

For simplicity, in the following we neglect the existence of the third and heaviest quark generation. Assuming that the target has equal number of protons and neutrons simplifies the problem further. Under the conditions stated above, the cross-section for neutrino-nucleon scattering is given by

$$\begin{aligned} \frac{d^2\sigma_{CC}^{\nu N}}{dxdy} &= 2x\sigma_0 \left(\sum_{d,s} f_q^N(x) + (1-y)^2 \sum_{\bar{u},\bar{c}} f_{\bar{q}}^N(x) \right), \\ \frac{d^2\sigma_{CC}^{\bar{\nu} N}}{dxdy} &= 2x\sigma_0 \left(\sum_{\bar{d},\bar{s}} f_{\bar{q}}^N(x) + (1-y)^2 \sum_{u,c} f_q^N(x) \right), \end{aligned} \tag{2.22}$$

where σ_0 is

$$\sigma_0 = \frac{G_F^2}{2\pi} s \left(1 + \frac{Q^2}{m_W^2} \right)^{-2}. \tag{2.23}$$

[1] The calculation of PDFs uses DIS as input. This research topic is a field on its own, and out of the scope of this work. For further details see [38].

The leading interactions for neutrinos are those between neutrinos and valence quarks. This yields, to a good approximation, a neutrino-nucleon cross-section independent of y, while for the antineutrino case it has a $(1-y)^2$ dependence. This feature will be further discussed in the experimental section of this work.

Measurements of the inclusive CC cross-section for muon neutrinos have been carried out by many experiments, recently NOMAD, NuTev and MINOS. Their results, compared to historical data, are shown in Fig. 2.6. Above a neutrino energy of 8 GeV the measurements have an accuracy of a few percent and have a linear dependence on neutrino energy, confirming the predictions of the quark-parton model.

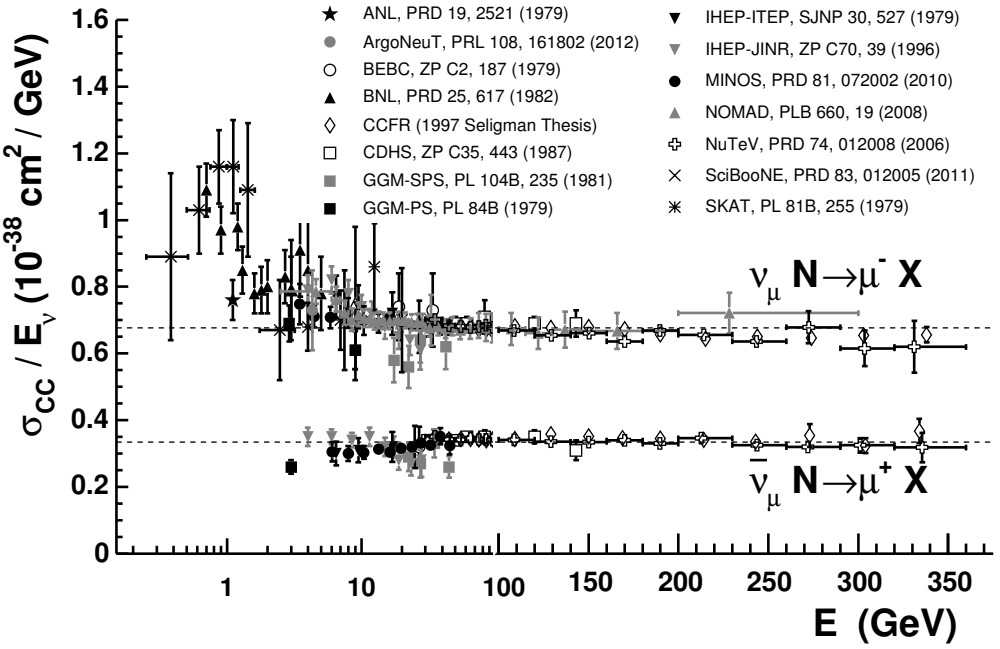

Figure 2.6: Measurements of $\nu_\mu - N$ CC inclusive cross-section as a function of neutrino energy. Note the change between logarithmic and linear scales at $E = 100$ GeV. Compilation taken from [30].

2.3.3 Interactions below the DIS threshold

For neutrino interactions in the DIS regime the constituents of the nucleon are considered individually. The nucleus as a whole is not taken into account. In contrast, below energies of $\mathcal{O}(100$ MeV) the interactions are calculated by modeling the nucleus as a coherent structure. These approaches are successful in explaining the measurements at the cost of keeping two disjointed regimes.

As it can be expected from such theoretical situation the transition between the two domains, $E_\nu \sim 0.1 - 10$ GeV, is very poorly understood. New processes start appearing, like quasi-elastic scattering and resonant, coherent and multi-pion production, with no clear way of combining them. Also, measurements at these energies are challenging, complicating advances in the modeling (see Section V in [37] and references therein). Figure 2.7 compares predictions and cross-section measurements in this energy region.

Interactions below the DIS threshold still need to be studied at a fundamental level. The effects of the nucleus both as a mixture of disconnected quarks and as a coherent entity require a unified treatment in order to understand the relative importance of their contributions.

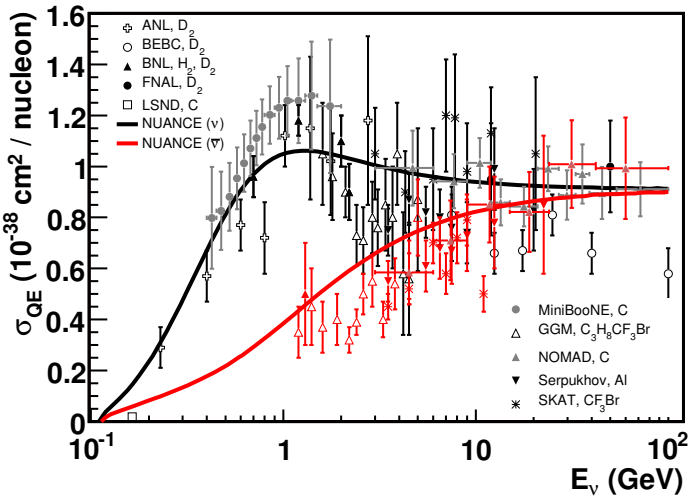

Figure 2.7: Cross-section measurements of ν_μ (black) and $\bar{\nu}_\mu$ (red) quasi-elastic scattering per nucleon as a function of neutrino energy. Taken from [30].

Even though this energy region could give access to some of the phenomena described in Chapter 5, it might as well bring large uncertainties into any potential measurement.

This Chapter explores the nature of neutrinos, as they stand in the original formulation of the Standard Model. One of the properties assigned to the particles, however, is now known to be incorrect: they are not all massless. The following Chapter follows how this small modification leads to neutrino oscillations, a phenomenon absent in the original SM.

3 Neutrinos beyond the Standard Model: mass, mixing and oscillations

In Chapter 2 it was repeatedly pointed out that neutrinos in the SM are massless particles. We now know, however, that this is not the case. Experiments have proven that neutrinos oscillate, and that the phenomenon can be fully explained by granting mass to the particles[1]. This Chapter begins by defining the phenomenon and addressing how it arises. From there, the mathematical formulation of the problem follows, where the case of neutrinos traveling freely and some special cases of neutrinos passing through matter are covered.

3.1 Why do neutrinos oscillate?

The term *oscillations*, as used throughout this work, refers to the periodic change on the probability of an elementary particle created in an eigenstate α to be detected as an eigenstate β, where $\alpha \neq \beta$. For such an phenomenon to occur, the particle must propagate in a basis different to that in which it interacts, and interference among the states should occur during propagation.

Even though the case of neutrinos is the one of interest for this work, the phenomenon is in principle not restricted to them. Any other particle family could also exhibit oscillations, as long as the conditions presented next are met. At the end of this Section, the conditions for charged lepton oscillations are evaluated.

3.1.1 Mixing of massive states

The first condition for oscillations to appear is that the particles involved must have different masses. In the SM, there are two ways in which neutrinos can acquire mass. They depend on the nature of the particle:

Dirac. Terms of the form shown in Eq. 2.2 can enter for SM neutrinos if the particle content of the model is expanded to include right-handed Dirac-type neutrino singlets. The coupling between the left- and right-handed parts of the field is understood as the mass of the particles, just as for the charged leptons.

Majorana. Neutral fermions can have their right-handed state identified with the antiparticle of the left-handed state, as proposed by Majorana [39]. This removes half of the degrees of freedom of the states, and violates the empirical lepton number conservation law.

As there is no evidence for favoring either of the possibilities, both have to be considered.

The next requirement is that the particles under study should have interaction eigenstates α which do not have a one-to-one correspondence to the mass eigenstates k, but are instead a mixture of them. The SM allows for this mixing to occur in weak interactions, as discussed

[1] Cosmological observations also support the hypothesis, favoring a non-zero sum of neutrino masses [36].

in Sec. 2.1.2. Neutrinos only interact weakly, and they do so as flavor eigenstates ν_α, which are defined by the charged lepton involved in the interaction vertex: e, μ or τ (see Sec. 2.2.1). The relation between neutrino mass and flavor eigenstates can be expressed as

$$\nu_\alpha = \sum_{k=1..3} U^*_{\alpha k}\, \nu_k \,. \tag{3.1}$$

Here $U_{\alpha k}$ are the elements of a matrix $\mathbf{U}$ where the mixing between mass and flavor states k and α is encoded[1].

Mixing three neutrino states requires $\mathbf{U}$ to be a 3×3 complex matrix. In the most general case the matrix can have $2N^2$ independent parameters. After applying unitarity constraints and using the freedom to rotate the fermion fields, the parameters are reduced to three real numbers and one or three complex phases[2]. The number of complex phases in the matrix depends on whether neutrinos are Dirac, with one phase permitted, or Majorana particles, with three phases allowed.

Following the parameterization advocated by the Particle Data Group,

$$\mathbf{U} = \begin{pmatrix} 1 & 0 & 0 \\ 0 & c_{23} & s_{23} \\ 0 & -s_{23} & c_{23} \end{pmatrix} \begin{pmatrix} c_{13} & 0 & e^{-i\delta} s_{13} \\ 0 & 1 & 0 \\ -e^{i\delta} s_{13} & 0 & c_{13} \end{pmatrix} \begin{pmatrix} c_{12} & s_{12} & 0 \\ -s_{12} & c_{12} & 0 \\ 0 & 0 & 1 \end{pmatrix} \begin{pmatrix} e^{i\rho_1} & 0 & 0 \\ 0 & e^{i\rho_2} & 0 \\ 0 & 0 & 1 \end{pmatrix}. \tag{3.2}$$

Here s and c stand for the sine and cosine functions, respectively. The arguments are three angles θ, whose subscripts denote the mass eigenstates that they mix. The complex phase δ appears both in the Dirac and Majorana cases[3], while ρ_1 and ρ_2 are exclusive to Majorana neutrinos.

Since neutrinos only interact weakly, they are produced as flavor eigenstates. These states, ν_e, ν_μ and ν_τ, are then a superposition of the mass eigenstates ν_1, ν_2, and ν_3. This can be seen by substituting Eq. 3.2 in Eq. 3.1, which gives

$$\begin{pmatrix} \nu_e \\ \nu_\mu \\ \nu_\tau \end{pmatrix} = \begin{pmatrix} U_{e1} & U_{e2} & U_{e3} \\ U_{\mu 1} & U_{\mu 2} & U_{\mu 3} \\ U_{\tau 1} & U_{\tau 2} & U_{\tau 3} \end{pmatrix} \begin{pmatrix} \nu_1 \\ \nu_2 \\ \nu_3 \end{pmatrix}. \tag{3.3}$$

The $U_{\alpha k}$ elements represent the amplitude that each mass eigenstate has in a flavor eigenstate. By taking the square of each element, the average mass composition for a neutrino with flavor α can be calculated.

The mixing, as formulated thus far, assumes that whatever the process in which a neutrino is produced, the energy available is at least equal or larger than the sum of the neutrino masses m_1, m_2 and m_3, so that all of the mass eigenstates can be produced. As mentioned in the previous Chapter, the neutrino masses are known to be of $\mathcal{O}(1\,\mathrm{eV})$ or smaller, which makes this assumption valid for most practical purposes.

3.1.2 Interference and oscillations

A description that renders the full phenomenology of neutrino oscillations require that the emission and detection processes are considered, and that the particles are described as wave

[1] The subscript *PMNS* is sometimes added to $\mathbf{U}$ to give credit to Pontecorvo, Maki, Nakagawa and Sakata, pioneers of the idea of oscillations.

[2] The full exercise can be found in [28, p. 106].

[3] The fact that δ appears together with θ_{13} is a consequence of the parameterization chosen. There is no physical connection between the two parameters.

packets. Such a description is mathematically complicated, and it is not within the scope of this work[1]. Instead, a discussion of the main ideas follows.

Coherent production of mass eigenstates

A neutrino produced in a weak decay is described by a wave packet. The wave packet has a momentum p_ν which is related to the neutrino energy E_ν and the neutrino mass m_ν by

$$E_\nu^2 = p_\nu^2 + m_\nu^2 \,. \tag{3.4}$$

By measuring the energy and momenta of the other particles in the decay, it is possible to determine the energy and momentum of the neutrino. These quantities, nevertheless, will have intrinsic quantum-mechanical uncertainties σ_E and σ_p [41,42]. Because of this, the mass of the neutrino can be derived only up to an uncertainty $\sigma_{m_\nu^2}$, given by

$$\sigma_{m_\nu^2} = \left[(2E\sigma_E)^2 + (2p\sigma_p)^2\right]^{1/2} , \tag{3.5}$$

where it has been assumed that σ_E and σ_p are uncorrelated. According to [43], σ_E and σ_p are approximately equal, and σ_E is essentially given by the decay widht of the parent particle Γ^0/γ, where γ is the Lorentz factor. Then, Eq. 3.5 can be approximated by

$$\sigma_{m_\nu^2} \simeq 2\sqrt{2}\, E\, \Gamma^0/\gamma \,. \tag{3.6}$$

Take $m_{j,k}$ to be the eigenvalue of the j,k-th neutrino mass eigenstate. If the condition

$$\sigma_{m_\nu^2} \geqslant |m_k^2 - m_j^2| \tag{3.7}$$

is fulfilled, then it is impossible to determine which neutrino mass eigenstate has been emitted. Instead, a coherent superposition of the different mass eigenstates has to be considered [41, 42,44]. An analogy can be drawn from the double-slit experiment: when there is not enough information to determine the path of a particle, the coherent sum of all possibilities has to be taken into account.

According to [41], the condition in Eq. 3.8 can be expressed in terms of the uncertainty either on the neutrino source or the detection point Δx, as

$$\Delta x > \frac{2p_\nu}{|m_k^2 - m_j^2|} \,. \tag{3.8}$$

The condition can be explored using a radioactive nucleus contained in an atomic lattice, as done in [42]. The position of such nucleus is certain to $\mathcal{O}(1\,\text{Å})$. In this very localized case, a coherent production of mass eigenstates takes place if

$$|m_k^2 - m_j^2| < 4 \times 10^9\,\text{eV}^2\, \frac{E_\nu}{\text{MeV}} \,.$$

If the lightest neutrino mass is negligible, the condition states that the heavier neutrino mass should be lighter than about $60\,\text{keV}\sqrt{E_\nu/\text{MeV}}$. Given that the limits on the neutrino mass are of $\mathcal{O}(1\,\text{eV})$ [33, 34], it is reasonable to expect that any decay emitting a neutrino will produce a coherent superposition of neutrino mass eigenstates.

[1] For a wave packet derivation of neutrino oscillations see [40].

Coherent detection of mass eigenstates

A coherent superposition of mass eigenstates interfere among themselves as they propagate. Oscillations are a result of this inteference, and in order to observe the phenomenon, the neutrinos have to be detected while interference effects are still taking place. In other words, the detection has to be performed while the system is still coherent. When the different mass eigenstates do not overlap, they cannot interfere to produce neutrino oscillations and only the mixing from $\mathbf{U}$ can be observed [45].

Since the masses of the eigenstates are different, they travel at different speeds, splitting the original packet into pieces. If the system is left to propagate undisturbed, the mass eigenstates will stop overlapping after some distance, and the interference will stop [45]. Following [41], consider a neutrino with momentum p_ν, composed by the superposition of two mass eigenstates ν_1 and ν_2 with speeds β_1 and β_2, respectively. These components will no longer overlap when $|t\beta_1 - t\beta_2| > \sigma_x$, where σ_x is the spread of the original wavepacket. According to [41], σ_x is given by the region within which the parent particle can be localized. This can depend either on the experimental setup ($\mathcal{O}(10^2\,\mathrm{m})$ for neutrino beams from π, K decays), or the lifetime of the particle in question. Using σ_x, the condition for overlapping mass eigenstates can be expressed as a condition on the distance traveled L, to be

$$L < \frac{\sigma_x}{|\beta_1 - \beta_2|} \simeq \sigma_x \frac{2p_\nu^2}{|m_2^2 - m_1^2|}\,. \tag{3.9}$$

For values of $p_\nu \sim 1\,\mathrm{MeV}$, $\sigma_x \sim 1\,\mathrm{m}$ and $m_{k,j} \sim 1\,\mathrm{eV}$, the mass eigenstates stop overlapping after traveling distances of $\mathcal{O}(10^9\,\mathrm{km})$. The coherence condition of overlapping mass eigenstates can then be assumed to be always fulfilled (at least for the current generation of oscillation experiments).

Note that detector limitations can mimic the practical outcome of non-overlapping eigenstates: only observing the neutrino mixing and not the oscillatory effect. They are briefly discussed after the derivation of oscillation probabilities for vacuum propagation.

3.1.3 Can the SM charged leptons oscillate?

Having just explained why neutrinos oscillate, and keeping in mind that the SM allows all fermions to mix, a natural question to ask is if the SM charged leptons could also oscillate. Although the topic is out of the scope of this work, briefly considering the idea can help in the understanding of the concepts presented before.

Oscillations occur for neutrinos because the interaction states are a mixture of the mass eigenstates, which interfere with each other as they propagate. The flavor eigenstates and mass eigenstates of charged leptons in the Standard Model are defined to have a one-to-one correspondence. A particle is identified as an *electron* during production because of its mass. This is the only property that distinguishes it from a muon or a tau. As the interaction eigenstates are not a mixture of mass eigenstates, oscillations like those described for neutrinos cannot occur for SM charged leptons [43, 44].

The conclusion reached relies on the assumption that the state produced is a SM charged lepton. However, consider for a moment the *Gedankenexperiment* presented in [43], in which an initial state e' is created, which is a coherent superposition of e, μ and τ. As these mass eigenstates travel, they interfere with each other, changing the projection of the system on the basis of the new state e'. In this situation, the conditions of mixed states and interference are met. Nevertheless, a set-up which relies on detecting massive particles would only measure

a constant mixture of SM leptons, given by the composition of e'. For oscillations like those of neutrinos to appear, a way of observing the newly defined state e' while it is still coherent would be also necessary.

Evaluating the conditions for charged leptons, as in [43]:

- Producing a coherent superposition of e, μ and τ. An uncertainty $\sigma_{m_\nu^2} \geqslant (106\,\mathrm{MeV})^2$, given by the muon mass, is required to produce the two lightest charged leptons coherently, which has to be compared with the one from a typical pion decay. From Eq. 3.6, the pion decay at rest has an uncertainty $\sigma_{m_\nu^2} \simeq 6.4\,\mathrm{eV}^2$. The decay of the W boson into a charged lepton and a neutrino, on the other hand, results in an uncertainty of $(5\,\mathrm{GeV})^2$, which is sufficient even to produce the τ lepton.

- Maintaining coherence over macroscopic distances. Applying Eq. 3.9 to the charged leptons resulting from the decay at rest of W yields a coherence length of $\mathcal{O}(10^{-11}\,\mathrm{m.})$ The W boson would need to be boosted for any effect to be observed.

The outcome is that a sort of neutrino-like oscillations involving charged leptons is not ruled out by current particle physics knowledge. Nevertheless, the conditions required for these oscillations to occur and be detected are not known to occur in Nature and would be very difficult to produce in the laboratory.

3.2 Neutrino oscillations in vacuum

The propagation of neutrinos in vacuum is used as the starting point for the derivation of oscillation probabilities. Unlike in the previous Section, the neutrinos are now described by plane waves. This calculation is much simpler, and its results have been found to be valid for all practical purposes [46, 47].

3.2.1 Derivation of oscillation probabilities

The calculation of oscillation probabilities is presented following the books of Giunti [28] and Bilenky [48]. Let us start by considering the evolution in time of an initial state $|\,i\,\rangle$, which is given by the Schrödinger equation

$$i\frac{d}{dt}\,|\,i\,\rangle = \mathcal{H}\,|\,i\,\rangle, \quad \text{with} \quad |\,i(0)\,\rangle = |\,i\,\rangle\,, \tag{3.10}$$

where $\mathcal{H}$ is the Hamiltonian of the system. For the case of particles propagating freely, the Hamiltonian $\mathcal{H}_0$ is independent of time, and the Schrödinger equation has solutions of the form

$$|\,i(t)\,\rangle = e^{-i\mathcal{H}_0 t}\,|\,i\,\rangle, \tag{3.11}$$

where

$$\mathcal{H}_0\,|\,i\,\rangle = E_i\,|\,i\,\rangle, \quad \text{with} \quad E_i = \sqrt{p_i^2 + m_i^2}. \tag{3.12}$$

Here the state $|\,i\,\rangle$ is an eigenstate of $\mathcal{H}_0$ with energy E_i, so the solutions can be written as

$$|\,i(t)\,\rangle = e^{-iE_i t}\,|\,i\,\rangle. \tag{3.13}$$

Take now an initial state $|\,\nu_\alpha\,\rangle$ to be a neutrino in a flavor eigenstate α produced in a decay. The amplitude for such neutrino to be detected with the flavor β after traveling for a

time t is given by

$$\mathcal{A}_{\nu_\alpha \to \nu_\beta}(t) = \langle\, \nu_\beta \,|\, \nu(t) \,\rangle = \langle\, \nu_\beta \,|\, e^{-i\mathcal{H}_0 t} \,|\, \nu_\alpha \,\rangle . \tag{3.14}$$

In order for the Hamiltonian to operate on the state $|\, \nu_\alpha \,\rangle$, the state has to be expressed in terms of the mass eigenstates that form it. This is done by changing $|\, \nu_\alpha \,\rangle$ to the mass basis. Substituting Eq. 3.1 in Eq. 3.14, and using Eq. 3.12,

$$\mathcal{A}_{\nu_\alpha \to \nu_\beta}(t) = \sum_k U^*_{\alpha k}\, e^{-iE_k t} \,\langle\, \nu_\beta \,|\, \nu_k \,\rangle \,, \tag{3.15}$$

where E_k is the energy of the k-th mass eigenstate. Since neutrinos interact as flavor eigenstates, Eq. 3.15 has to be returned to the flavor basis by means of the complex conjugate of Eq. 3.1,

$$|\, \nu_k \,\rangle = \sum_\eta U_{\eta k} \,|\, \nu_\eta \,\rangle \,. \tag{3.16}$$

Applying Eq. 3.16 and making use of the states being orthogonal and the fact that $\mathbf{U}$ is a unitary matrix,

$$\mathcal{A}_{\nu_\alpha \to \nu_\beta}(t) = \sum_k U^*_{\alpha k}\, U_{\beta k}\, e^{-iE_k t} \,. \tag{3.17}$$

Taking the square of the amplitude to determine the probability for the transition, we have that

$$P_{\nu_\alpha \to \nu_\beta}(t) = |\mathcal{A}_{\nu_\alpha \to \nu_\beta}(t)|^2 = \sum_{k,j} U^*_{\alpha k}\, U_{\beta k}\, U_{\alpha j} U^*_{\beta j}\, e^{-i(E_k - E_j)t} \,. \tag{3.18}$$

Neutrinos, which have masses of $\mathcal{O}(1\,\text{eV})$ or smaller [33,34], are extremely relativistic particles already at energies of $\mathcal{O}(1\,\text{keV})$. In this limit, it is possible to neglect the mass contribution to the total energy of the particle in Eq. 3.4, which results in $E_k \simeq E$. The first order correction to this formula depends on the square of the neutrino mass [44], and can be written as

$$E_k \simeq E + \frac{m_k^2}{2E} \,. \tag{3.19}$$

Substituting Eq. 3.19 in the phase of Eq. 3.18,

$$-\,i\,(E_k - E_j)\,t \simeq -i\,\frac{m_{kj}^2}{2E}\,t \,. \tag{3.20}$$

In the relativistic limit being considered, the time t at which a neutrino is detected can be approximated by the distance L that the particle has traveled between the points of production and interaction. Making use of $L \simeq t$ ($c = 1$), the phase in Eq. 3.20 becomes

$$-\,i\,\frac{m_{kj}^2}{2E}\,t = -i\,\frac{m_k^2}{2E}\,L \,. \tag{3.21}$$

Substituting this factor back into the transition probability of Eq. 3.18 yields

$$P_{\nu_\alpha \to \nu_\beta}(L) = \sum_{k,j} U^*_{\alpha k}\, U_{\beta k}\, U_{\alpha j} U^*_{\beta j}\, e^{-i\frac{\Delta m_{kj}^2}{2E}L} \,, \tag{3.22}$$

where $\Delta m_{kj}^2 = m_k^2 - m_j^2$ and E is the energy with which the neutrino was produced. The expression can be rewritten to separate the real and imaginary contributions of the mixing

matrix explicitly, as

$$P_{\nu_\alpha \to \nu_\beta}(L,E) = \delta_{\beta\alpha} - 4 \sum_{k>j} \Re[U^*_{\alpha k}\, U_{\beta k}\, U_{\alpha j}\, U^*_{\beta j}] \, \sin^2\left(\frac{\Delta m^2_{kj}}{4E}\, L\right) \pm 2 \sum_{k>j} \Im[U^*_{\alpha k}\, U_{\beta k}\, U_{\alpha j}\, U^*_{\beta j}] \, \sin\left(\frac{\Delta m^2_{kj}}{2E}\, L\right) . \tag{3.23}$$

The sign of the imaginary part depends on whether neutrinos (+) or antineutrinos (−) are being considered.

The probability for flavor transition depends on the mixing matrix, which determines the amplitude of the oscillation, and the mass differences which affect the phase. A term with these two characteristics is formed for each pair of neutrino mass eigenstates. The mass difference sits inside an even function in the real term, making the term insensitive to its sign. The imaginary part, on the other hand, adds a component which is sensitive to the sign of the mass difference. The phases ϕ_{kj} can be written in more convenient units after restoring the values of c and $\hbar$, as

$$\phi_{kj} = a\, \frac{\Delta m^2_{kj}}{4E}\, L \simeq a \times 1.267\, \frac{\Delta m^2_{kj}}{\mathrm{eV}^2}\, \frac{\mathrm{GeV}}{E}\, \frac{L}{\mathrm{km}} , \tag{3.24}$$

where $a = 1, 2$ for the real and imaginary phases, respectively.

The multiplication of mixing matrices in Eq. 3.23 assures that, if Majorana phases exist, they have no impact in oscillations [28, p. 250]. As a result the solution derived holds regardless of whether neutrinos are Dirac- or Majorana-type particles.

3.2.2 Hierarchy of neutrino masses

Thus far we know of the existence of three neutrino flavor and mass eigenstates, from which two independent mass squared differences, or *mass-splittings* can be derived. If one of the mass eigenstates is much heavier or lighter than the other two, then

$$|\Delta m^2_{\mathrm{large}}| \gg |\Delta m^2_{\mathrm{small}}| .$$

Neutrinos have been observed to follow such a hierarchy, with $|\Delta m^2_{\mathrm{large}}/\Delta m^2_{\mathrm{small}}| \simeq 30$ [30]. Under these circumstances it is possible for experiments to be mainly sensitive to one of these splittings [28, p. 273]. To explore this, take a neutrino emission where three mass eigenstates are produced, out of which m_3 is much lighter than the others. The two mass-splittings are then

$$|\Delta m^2_{\mathrm{large}}| \simeq |m_3 - m_{1,2}| , \quad \text{and} \tag{3.25}$$

$$|\Delta m^2_{\mathrm{small}}| = |m_2 - m_1| , \tag{3.26}$$

giving two scenarios that can be explored:

(i) Being the lightest state, m_3 is the fastest and gains spatial separation first [41]. While moving away from m_1 and m_2, m_3 interferes with them. Because of the existence of a pronounced hierarchy, if m_3 has just started pulling away, m_1 and m_2 have had no time to separate, and they interfere constructively. They behave effectively as one state. This conclusion can also be derived from the phases ϕ_{kj} in Eq. 3.23: when $\phi_{\mathrm{large}} \sim \pi$,

$\phi_{\text{small}} \ll \pi$. Under these conditions, the oscillation probabilities mainly depends on $|\Delta m^2_{\text{large}}|$.

(ii) On the other hand, if the same system is left to evolve for a longer time, at the point in space where $\phi_{\text{small}} \sim \pi$, $\phi_{\text{large}} \gg \pi$. While in principle both phases play a role on the oscillation probabilities under these conditions, in practice ϕ_{large} can be too fast for a detector to be able to resolve it. If the detector's resolution in L/E dilutes the effects of oscillations (which can happen already by its size), then the contribution of the large mass-splitting has to be averaged, resulting in a constant probability [28, p. 277]. Measurements of oscillation probabilities at this L/E combination can be described by a constant value and an oscillatory term that only depends on $|\Delta m^2_{\text{small}}|$.

The existence of a hierarchy gives rise to these two scenarios, where oscillation probabilities can be described by a scheme with only two neutrinos and two effective mixing angles[1] θ_{large}, θ_{small}. This conclusion holds regardless of the values of the three mixing angles that compose the mixing matrix $\mathbf{U}$. However, the situation can be further simplified if θ_{13} is small enough ($\sin\theta_{13} \leqslant 0.01$ [30]), which results in

$$\theta_{\text{small}} \simeq \theta_{12}\,, \tag{3.27}$$

$$\theta_{\text{large}} \simeq \theta_{23}\,, \tag{3.28}$$

and a constant value for case (ii) which is almost zero [30].

Both of the cases discussed are exemplified using the survival probability for ν_μ shown in Fig. 3.1. A travel distance L of 2 000 km and a source of neutrinos which covers a wide energy range are assumed. The precise values of the mass differences are not of importance, as it is enough to require that the masses have a pronounced hierarchy. For this example, a value close to the one realized in Nature was used.

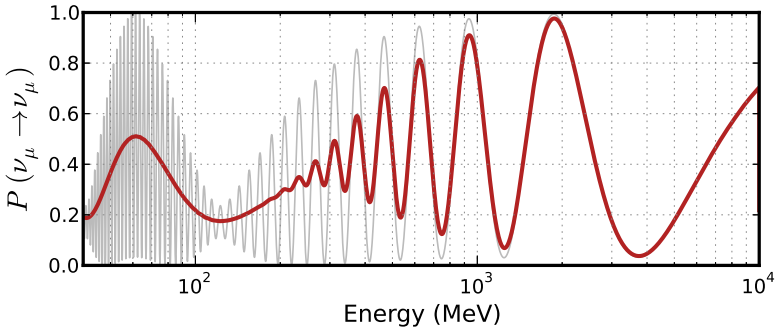

Figure 3.1: Survival probability for ν_μ for a wide energy range and a travel distance of $L = 2\,000$ km. The gray line is the exact value from Eq. 3.23, the red line includes a 4 % energy resolution at detection. Calculated using the values of Table 4.1.

Two probabilities are shown in the Figure. The one in gray was calculated using Eq. 3.23, while the one in red uses the same equation but it includes a finite energy resolution during detection, of about 4 %, while no uncertainty is assumed for the detection point. Above 1 GeV, the parameter $\Delta m^2_{\text{large}}$ determines the phase of the oscillation probability. The transitions in this region can be approximated by a scheme with only two neutrinos and one effective mixing angle.

[1] For consistency, the angles are labeled according to the mass-splitting that they couple (large, small). This corresponds to the labels "atmospheric" and "solar" which are used in the literature.

Below 200 MeV, both of the mass differences affect the result. The oscillations created by the parameter $\Delta m^2_{\text{large}} L/E$ happen at scales smaller than the detector's resolution, so the result has to be averaged over. The contribution of the large mass-splitting to the probability is then a constant value, which depends only on the matrix $\mathbf{U}$. Oscillations produced by $\Delta m^2_{\text{small}}$ have a much slower phase, which the detector can observe. The transition probability in this region can also be described by a scheme with two neutrinos, plus a constant value.

For this example, the uncertainty was assigned to the detector's energy resolution, assuming perfect localization of production and detection points. As oscillations are a function of L/E, a realistic calculation should average over $\sigma_{L/E}$.

3.2.3 The two-neutrino scheme

When the two-neutrino scheme is sufficient to explain oscillation probabilities, $\mathbf{U}$ turns into a 2×2 matrix which depends on a single mixing angle θ and does not include an imaginary phase,

$$\mathbf{U}_{2\nu} = \begin{pmatrix} \cos\theta & \sin\theta \\ -\sin\theta & \cos\theta \end{pmatrix}. \tag{3.29}$$

Substituting $\mathbf{U}_{2\nu}$ and Δm^2 in 3.23 results in a sum with only one term, which is

$$P^{2\nu}_{\nu_\alpha \to \nu_\beta}(L, E) = \sin^2(2\theta) \sin^2\left(\frac{\Delta m^2}{4E} L\right). \tag{3.30}$$

The simplicity of Eq. 3.30 is very convenient for analyzing data, and its results can be rather precise. Figure 3.2 uses the best known oscillation parameters, presented in the next Chapter, to compute the survival probability for an electron neutrino after a propagation distance of 1 000 km in the two- and three-neutrino schemes. The large mass-splitting gives the dominant effect. The main difference is a slight modification in the phase, which translates in probability differences smaller than 0.05 for most of the energy region shown.

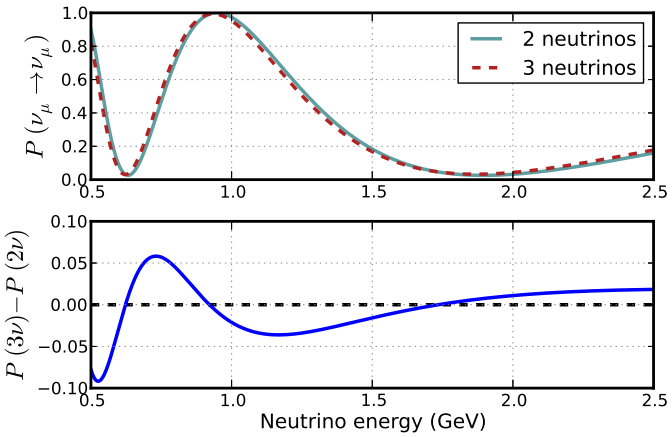

Figure 3.2: Survival probability for ν_μ after traveling 1 000 km in vacuum. Calculated in the two- and three-neutrino formalisms. Using the oscillation parameters from Table 4.1.

3.3 Neutrino oscillation in matter

3.3.1 Effective matter potentials

In the previous Section we considered neutrinos propagating in vacuum, but when traversing normal matter neutrinos can scatter with electrons, protons and neutrons. Although the probability of an interaction is rather small, Wolfenstein found that the sheer number of targets creates an effective potential, an effect known as coherent forward scattering [49]. The Feynman diagrams that correspond to these elastic exchanges are shown in Fig. 3.3.

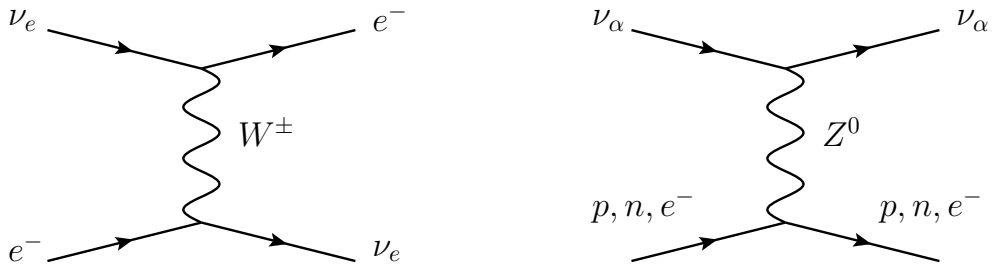

(a) CC **(b)** NC

Figure 3.3: Elastic scattering processes between neutrinos and matter.

The Lagrangian resulting from coherent scattering via the Z^0 boson has the same form independently of neutrino flavor, with a sign that changes with the electric charge of the target (see Eq. 2.4). When traversing normal matter, the number of electrons and protons that neutrinos meet is equal, which leads to a cancellation of both effects. The scattering with neutrons, on the other hand, affects all flavors equally, yielding an overall phase without any physical consequences, which can be neglected. As a result, there is no contribution from neutral current processes to the case under discussion[1].

The only elastic scattering that affects the neutrinos as they travel through matter is that of ν_e with electrons. From the neutrino point of view, the presence of electrons can be seen as an effective potential $V_{\rm CC}$ which affects only the electron neutrino flavor, and is given by[2]

$$V_{\rm CC}(n_e) = \pm\sqrt{2}\, G_F\, n_e(x)\,. \tag{3.31}$$

The plus sign applies for neutrinos and the minus for antineutrinos; n_e is the number of electrons per mole or electron number density along the path, and G_F is the Fermi constant, containing the strength of the interaction between an electron and a neutrino, as given in Eq. 2.15. After multiplying by a factor $(\hbar c)^3$ and substituting the value of G_F, Eq. 3.31 can be given in more convenient units, as

$$V_{\rm CC}(x) \simeq \pm 7.54 \times 10^{-14}\, Y_e(x)\, \frac{\rho(x)}{\mathrm{g/cm}^3}\ \mathrm{eV}\,. \tag{3.32}$$

Here the electron density n_e has been replaced by the matter density ρ multiplied by the number of electrons per nucleon Y_e, which for normal matter has a value close to 0.5.

[1] This statement is true up to small radiative corrections [50].
[2] The calculation of $V_{\rm CC}$ can be found in [48, p. 124] and [28, p. 324].

3.3.2 Neutrino propagation in matter

The evolution of a neutrino state in the Schrödinger picture is given by Eq. 3.10, introduced for describing the propagation of neutrinos in vacuum[1]. For the case of neutrinos passing through matter, the total Hamiltonian $\mathcal{H}$ can be expressed as

$$\mathcal{H} = \mathcal{H}_0 + \mathcal{H}_I \,. \tag{3.33}$$

Here $\mathcal{H}_0$ describes the free propagation in vacuum, whose eigenstates are the neutrino mass eigenstates, with eigenvalues as given in Eq. 3.12. $\mathcal{H}_I$ describes the interactions between neutrinos and matter, and their eigenstates are the neutrino flavor states. From the previous Section, the only interaction of relevance comes from CC scattering of electron neutrinos with electrons, which gives

$$\mathcal{H}_I \,|\, \nu_e \,\rangle = V_{\rm CC} \,|\, \nu_e \,\rangle \,, \tag{3.34}$$

where $V_{\rm CC}$ is the potential defined in Eq. 3.31. This potential makes the total Hamiltonian of the system dependent on the electron density along the neutrino trajectory, so solutions similar to those given in Eq. 3.11 do not apply in general, and the calculation of the probabilities has to be carried out again.

As for the vacuum case, we start by looking at the transition amplitude for a neutrino produced with a flavor eigenstate α to be detected in the flavor eigenstate β, which we denote as $\psi_{\alpha\beta}$. This amplitude is given by

$$\psi_{\alpha\beta}(t) = \langle\, \nu_\beta \,|\, \nu_\alpha(t) \,\rangle \,, \tag{3.35}$$

and its time evolution, as for the whole state, is governed by Eq. 3.10, where

$$i\frac{d}{dt}\,\psi_{\alpha\beta}(t) = \mathcal{H}_0\;\psi_{\alpha\beta}(t) + \mathcal{H}_I\;\psi_{\alpha\beta}(t)\,. \tag{3.36}$$

The first term on the right-hand side of the Eq. 3.36 corresponds to the starting point of the vacuum case (see Eq. 3.14). Using the result obtained in Eq. 3.21 the evolution of the free Hamiltonian can be expressed as

$$\mathcal{H}_0\;\psi_{\alpha\beta}(t) = \sum_k U^*_{\alpha k}\,\frac{\Delta m^2_{k1}}{2E}\,U_{\beta k}\;\psi_{\alpha\beta}(t)\,. \tag{3.37}$$

Using the eigenvalues of the matter potential, given in Eq. 3.34, and substituting Eq. 3.37 into Eq. 3.36 with the approximation $x \simeq t$ as for the vacuum case, yields

$$i\frac{d}{dx}\,\psi_{\alpha\beta}(x) = \left(\sum_k U^*_{\alpha k}\,\frac{\Delta m^2_{k1}}{2E}\,U_{\beta k}\;\; + \delta_{\alpha e}\,V_{\rm CC}\right)\,\psi_{\alpha\beta}(x)\,. \tag{3.38}$$

The equation has again the form of a Schrödinger equation with an effective Hamiltonian $\mathcal{H}_F$. This can be seen explicitly if the exercise is done for all possible flavors and the amplitudes are written in matrix form as a system of coupled differential equations, as

$$i\frac{d}{dx}\mathbf{\Psi}_\alpha = \mathcal{H}_F\mathbf{\Psi}_\alpha \quad \text{ with } \; \mathcal{H}_F = \frac{1}{2E}(\mathbf{U}\,\mathbf{M}^2\mathbf{U}^\dagger + \mathbf{A}). \tag{3.39}$$

[1] As for the vacuum case, the propagation of neutrinos in matter closely follows the books of Giunti [28] and Bilenky [48].

Taking the two-neutrino scheme to simplify the matrices,

$$\mathbf{\Psi}_\alpha = \begin{pmatrix} \psi_{ee} \\ \psi_{e\mu} \end{pmatrix} \quad \mathbf{M}^2 = \begin{pmatrix} 0 & 0 \\ 0 & \Delta m^2 \end{pmatrix} \quad \mathbf{A} = \begin{pmatrix} A_{\rm CC} & 0 \\ 0 & 0 \end{pmatrix}, \tag{3.40}$$

where $A_{\rm CC} = 2\,E\,V_{\rm CC}$ and $\mathbf{U}$ is the 2×2 real matrix introduced in Eq 3.29.

Before continuing, it is convenient to write the total effective Hamiltonian $\mathcal{H}_F$ as a sum of two matrices where one is proportional to the unit matrix and the other is traceless, as

$$\mathcal{H} = \frac{1}{2}\,\mathrm{Tr}(\mathcal{H})\,\mathbf{1} + \mathcal{H}_M\,. \tag{3.41}$$

Here $\mathbf{1}$ is the unit matrix, and $\mathrm{Tr}(\mathcal{H}_M) = 0$. Rewriting $\mathcal{H}_F$ in this way gives

$$\mathcal{H}_F = \frac{1}{4E}\left(A_{\rm CC} + \Delta m^2\right)\mathbf{1} + \frac{1}{4E}\begin{pmatrix} -\Delta m^2\cos 2\theta + A_{\rm CC} & \Delta m^2 \sin 2\theta \\ \Delta m^2 \sin 2\theta & \Delta m^2 \cos 2\theta - A_{\rm CC} \end{pmatrix} \tag{3.42}$$

A diagnoal matrix does not contribute to transitions between the states, so only the traceless matrix $\mathcal{H}_M$ is of relevance for oscillations. This matrix is Hermitian, and can be diagonalized by the transformation[1]

$$\mathbf{U}_M^\dagger \mathcal{H}_M \mathbf{U}_M = \frac{1}{4E}\begin{pmatrix} -M & 0 \\ 0 & M \end{pmatrix}, \quad \text{with} \quad \mathbf{U}_M = \begin{pmatrix} \cos\theta_M & \sin\theta_M \\ -\sin\theta_M & \cos\theta_M \end{pmatrix}. \tag{3.43}$$

Note that the matrix $\mathbf{U}_M$ has the same form as the mixing matrix for the two-neutrino mixing of Eq. 3.29. Moreover, if the transformation is applied to the Hamiltonian of vacuum propagation ($A_{\rm CC} = 0$), the place taken by the M variable corresponds to the mass-splitting Δm^2. It follows that the angle θ_M and M can be interpreted as the effective parameters that neutrinos experience when passing through matter. It is then possible to find that

$$M = \Delta m^2_M = \sqrt{(\Delta m^2\cos 2\theta - A_{\rm CC})^2 + (\Delta m^2 \sin 2\theta)^2}\,, \quad \text{and} \tag{3.44}$$

$$\tan 2\theta_M = \frac{\tan 2\theta}{1 - \dfrac{A_{\rm CC}}{\Delta m^2 \cos 2\theta}}. \tag{3.45}$$

Rewriting Eq. 3.40 in terms of the effective matter parameters, and keeping only $\mathcal{H}_M$,

$$i\frac{d}{dx}\begin{pmatrix} \psi_{ee} \\ \psi_{e\mu} \end{pmatrix} = \frac{1}{4E}\begin{pmatrix} -\Delta m^2_M \cos 2\theta_M & \Delta m^2_M \sin 2\theta_M \\ \Delta m^2_M \sin 2\theta_M & \Delta m^2_M \cos 2\theta_M \end{pmatrix}\begin{pmatrix} \psi_{ee} \\ \psi_{e\mu} \end{pmatrix}. \tag{3.46}$$

The matrix $\mathbf{U}_M$ can now be used to express the flavor eigenstates ψ in Eq. 3.46 into the effective eigenstates for matter propagation ϕ by the transformation

$$\mathbf{\Psi}_e = \mathbf{U}_M \mathbf{\Phi}_e\,, \quad \text{with} \quad \mathbf{\Psi}_e = \begin{pmatrix} \psi_{ee} \\ \psi_{e\mu} \end{pmatrix}, \quad \mathbf{\Phi}_e = \begin{pmatrix} \phi_{e1} \\ \phi_{e2} \end{pmatrix}. \tag{3.47}$$

Using this transformation and multiplying the entire equation by $\mathbf{U}_M^\dagger$ from the left side gives

$$i\,\mathbf{U}_M^\dagger\left(\frac{d}{dx}\mathbf{U}_M\right)\mathbf{\Psi_e} + i\,\mathbf{U}_M^\dagger \mathbf{U}_M \frac{d}{dx}\mathbf{\Psi_e} = \frac{1}{4E}\begin{pmatrix} -\Delta m^2_M & 0 \\ 0 & \Delta m^2_M \end{pmatrix}\mathbf{\Phi}_e\,. \tag{3.48}$$

[1] A proof of this can be found in [48, p. 237].

Simplifying the expression and passing the term with the derivative of $\mathbf{U}_M$ to the right-hand side of the equation results in

$$i\frac{d}{dx}\begin{pmatrix}\phi_{e1}\\ \phi_{e2}\end{pmatrix} = \frac{1}{4E}\begin{pmatrix}-\Delta m^2_M & -i\,4E\,d\theta_M/dx\\ i\,4E\,d\theta_M/dx & \Delta m^2_M\end{pmatrix}\begin{pmatrix}\phi_{e1}\\ \phi_{e2}\end{pmatrix}. \tag{3.49}$$

Solutions to Eq. 3.49 require to integrate over the changes in the mixing angle, hence electron density, for the trajectory that the neutrinos cross. As the electron density profile can take any form it is not possible to obtain a general analytic solution. Nevertheless, the formulation found allows to easily identify general properties and approximate solutions for some of the cases that can be found in Nature.

Before continuing, it is important to point out that the same steps taken for obtaining Eq. 3.49 can be followed for the case of three neutrinos, as done in [51]. When performing such a calculation, both mass-splittings have to modified according to Eq. 3.44. From the three mixing angles, however, only two need to be modified following Eq. 3.45. The potential matrix in the three-neutrino scheme is invariant under 2-3 rotations, so θ_{23} stays unchanged [52,53].

3.3.3 Oscillation probabilities with matter effects

The MSW effect

Neutrino flavor transitions due to oscillations in matter can become maximal, regardless of how small they might be in vacuum. This can be seen from the definition of the effective mixing angle given in Eq. 3.45, which has a pole at

$$A_{\mathrm{CC}} = \Delta m^2 \cos 2\theta\,. \tag{3.50}$$

In more convenient units, the position of the pole can be expressed as

$$\Delta m^2 \cos 2\theta \simeq 7.54\times 10^{-5}\frac{\rho}{\mathrm{g/cm^2}}\frac{E}{\mathrm{GeV}}\ \mathrm{eV}^2. \tag{3.51}$$

Approaching this equality results in an effective mixing angle that tends to $\pi/4$. From Eq. 3.46, the amplitude of a flavor transition is proportional to $\cos 2\theta_M$, which is maximum for $\theta_M = \pi/4$, meaning that the pole maximizes the mixing between two neutrino states.

This resonance was first discovered by Mikheev and Smirnov [54,55], and is known as the *MSW effect*. Note that to be able to fulfill the resonance condition, the product $\Delta m^2 \cos 2\theta$ needs to have the same sign as A_{CC}. The following cases are possible:

- the signs of Δm^2 and $\cos 2\theta$ are equal → neutrinos can resonate,
- the signs of Δm^2 and $\cos 2\theta$ are opposite → antineutrinos can resonate.

Testing which one of these cases takes place in Nature is a way of identifying the ordering of the neutrino masses.

The enhancement of a small mixing angle due to matter effects is shown in Fig. 3.4. After the resonance condition is met, when $|A_{\mathrm{CC}}| \gg |\Delta m^2 \cos 2\theta|$ the denominator of Eq. 3.45 becomes very large and the effective angle in matter tends to $\pi/2$.

The mass-splitting at the resonance point takes the value of $\Delta m^2 \sin 2\theta$. This value is the minimum of the Eq. 3.44 with respect to A_{CC}. Having the smallest mass difference possible, the interference among the states at the resonance point is slowed down when compared to the vacuum case.

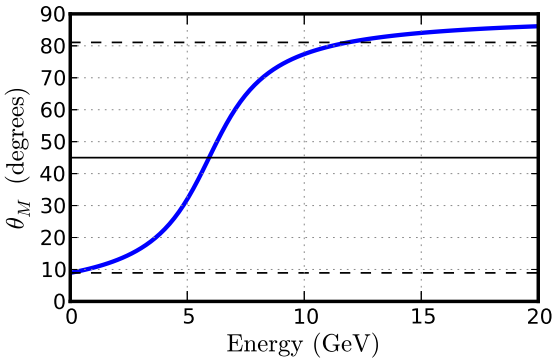

Figure 3.4: Effective θ_{13} as a function of neutrino energy for an electron number density of 2.5 (blue). Dashed black lines show the value of θ_{13} for vacuum, from 4.1, and its complement $(\pi/2 - \theta_{13})$. The solid black line indicates maximal mixing. Calculated using Eq. 3.45.

Constant electron density

The simplest case of neutrino oscillations in matter is that of a constant electron density along the path that they cross. Neutrinos crossing the Earth's mantle can be studied using this approximation. In this situation

$$\frac{d\theta_M}{dx} = 0\,. \tag{3.52}$$

Substituting the derivative in Eq. 3.49 yields

$$i\frac{d}{dx}\begin{pmatrix}\phi_{e1}\\ \phi_{e2}\end{pmatrix} = \frac{1}{4E}\begin{pmatrix}-\Delta m^2_M & 0\\ 0 & \Delta m^2_M\end{pmatrix}\begin{pmatrix}\phi_{e1}\\ \phi_{e2}\end{pmatrix}\,, \tag{3.53}$$

which is identical to the evolution equation for neutrinos in vacuum[1]. This leads to a transition probability that has the same structure,

$$P^{2\nu\ \text{matter}}_{\nu_e\to\nu_\mu}(x,E) = \sin^2(2\theta_M)\sin^2\left(\frac{\Delta m^2_M}{4E}L\right)\,, \tag{3.54}$$

where the effective oscillation parameters for matter Δm^2_M and θ_M have been used.

Parametric resonance

Another way in which the flavor transitions of neutrinos can be enhanced compared to the ones in vacuum is by the so-called *parametric resonance*. The possibility exists for neutrinos traveling along a path with regions of constant electron density that change periodically. The *castle wall* profile, shown in Fig. 3.5, is an example of such a case.

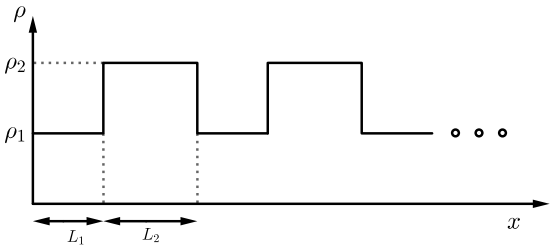

Figure 3.5: Periodic matter potential known as *castle wall*. Taken from [28, p. 343].

[1] This can be proven by setting $A_{\text{CC}} = 0$ and following the same steps as for the matter case.

The castle wall profile with one and a half periods (from Fig. 3.5, $L = L_1 + L_2 + L_1$) is a good approximation to the potential experienced by neutrinos that pass through the Earth crossing its core [56]. Their evolution can be described by a product of Hamiltonians of constant electron density,

$$\mathcal{H}_F = \left[\mathbf{U}^\dagger \mathcal{H}(x = L1)\mathbf{U}\right]_{M1} \left[\mathbf{U}^\dagger \mathcal{H}(x = L2)\mathbf{U}\right]_{M2} \left[\mathbf{U}^\dagger \mathcal{H}(x = L1)\mathbf{U}\right]_{M1} , \tag{3.55}$$

where the terms inside each parentheses are to be evaluated in the layer given by the subscripts $M1$ and $M2$. The resulting $\mathcal{H}$ has analytic solutions for the two-neutrino case, resulting in

$$P^{2\nu_{CW}}_{\nu_e \to \nu_\mu} = \left(2 s_1 \sin 2\theta_{M1} \left(c_1 c_2 - s_1 s_2 \cos 2\left(\theta_{M1} - \theta_{M2}\right)\right) + s_2 \sin 2\theta_{M2}\right)^2 , \tag{3.56}$$

as derived in [28, p. 343]. The variables s_k and c_k are the sine and cosine functions of ϕ_k, the phase acquired by the neutrinos in the k-th layer. This phase is given by layer thickness L_k and the effective mass difference in it Δ^2_{Mk}, as $\phi_k = \Delta^2_{Mk} L_k / 4E$.

The probabilty in Eq. 3.56 shows that the transitions depend on the difference between the effective mixing angles, and in turn on the electron densities. A large transition probability can be obtained even if the A_{CC} value of both of the layers is far from the MSW condition in Eq. 3.50. A more detailed explanation of the effect, as well as resonance conditions for neutrinos crossing the Earth, can be found in [57, 58].

Figure 3.6 compares the oscillation patterns expected for the cases of propagation in vacuum, a constant electron density, and along a periodic electron density profile. One and a half periods are assumed. At low energies, the change in the oscillation phase can be observed, as the peaks of the vacuum case do not coincide with those of the propagation in matter. At higher energies the probabilities differ, with the constant matter suppressing oscillations, and the periodic potential making them maximal.

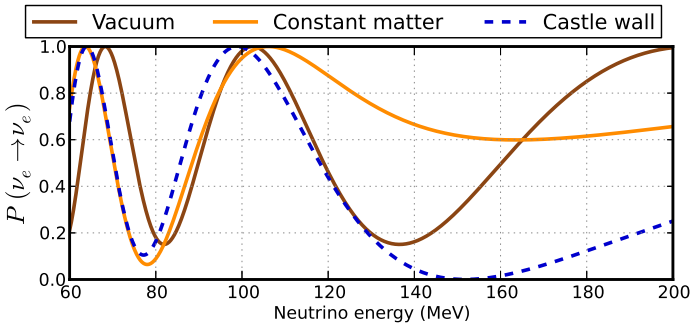

Figure 3.6: Comparison of oscillations probabilities in vacuum, constant matter ($n_e = 4$) and a castle wall potential ($n_e = 2, 4, 2$). Using the oscillation parameters from Table 4.1 and $L = 6\,700$ km.

Adiabatic evolution

Going back to Eq. 3.49, we focus now on the off-diagonal terms of the Hamiltonian. These terms generate transitions between the effective neutrino mass eigenstates in matter, and depend on how rapidly the electron density changes along the neutrino path. The importance of these transitions with respect to the diagonal terms can be quantified by the *adiabaticity parameter*

$$\gamma = \frac{\Delta m^2_M}{4E|d\theta_M/dx|} = \frac{\Delta\left(m^2_M\right)^2}{2E \sin 2\theta_M |dA_{\mathrm{CC}}/dx|} . \tag{3.57}$$

If $\gamma \gg 1$ for all the points in the trajectory, the evolution is said to be adiabatic, and the off-diagnoal terms of the Hamiltonian can be neglected. If that is the case, each state evolves independently, gaining only a phase factor of the form

$$\phi_{ej}(x) = \exp\left(\pm i \int_0^x \frac{\Delta m^2_M(x')}{4E} dx'\right) \phi_{ej}(0)\,, \tag{3.58}$$

where the plus sign applies for $j = 1$ and minus for $j = 2$. Using this phase, the oscillation probability is given by

$$P^{\text{adiabatic}}_{\nu_e \to \nu_e}(x) = \frac{1}{2} + \frac{1}{2}\cos 2\theta^{(\text{i})}_M \cos 2\theta^{(\text{f})}_M \tag{3.59}$$

$$+ \frac{1}{2}\sin 2\theta^{(\text{i})}_M \sin 2\theta^{(\text{f})}_M \cos\left(\int_0^x \frac{\Delta m^2_M(x')}{2E} dx'\right)\,. \tag{3.60}$$

The superscripts (i) and (f) on the mixing angle stand for interaction and detection points, respectively. The first two terms account for the effective mixing, while the last one includes the interference effects.

This type of evolution can occur for neutrinos emitted by stars, which have an electron density that varies smoothly. Moreover, neutrinos from stars are detected after traveling astronomical distances, so the phase of Eq. 3.58 is very large, and varies too fast to be detected. The average of the cosine has to be taken, which is zero. Now taking into account that the detection takes place after traveling through vacuum,

$$\bar{P}^{\text{adiabatic}}_{\nu_e \to \nu_e} = \frac{1}{2} + \frac{1}{2}\cos 2\theta^{(\text{i})}_M \cos 2\theta\,, \tag{3.61}$$

where the bar over the P indicates that the probability has been averaged.

Matter effects with 3 neutrino flavors

Analyzing matter effects in a two-neutrino scheme allows obtaining analytical solutions for special cases at the cost of not rendering the full phenomenology that appears from having three states involved. Besides the expected effects of modifying the oscillatory pattern in a more complicated way, effects related to the factor $e^{i\delta}$ in the mixing matrix also appear. The possibility for fundamental CP and T violation arises, which cannot exist without this complex phase [59]. Another possibility is that of matter-induced T violation, which can happen for asymmetric electron density profiles with more than 3 neutrino states. Detecting them requires experiments highly sensitive to small perturbations in the oscillation patterns and/or capable of gathering very large statistics. None of the current experiments has been sensitive enough to measure matter effects in oscillations with three neutrino states.

As mentioned in the Introduction, neutrino oscillations have been observed by several experiments. Most of the parameters that describe the phenomenon are known to some extent. How this is done is presented in the next Chapter, which starts by delimiting what is known and what is yet to be discovered on the subject.

4 Selected experimental results

Many experiments have contributed to establish that neutrinos oscillate. They have been performed in a wide variety of circumstances, using different neutrino sources and detection techniques while covering an extensive range of energies and travel distances. A small selection of them is presented here with the aim of portraying, however briefly, the variety mentioned.

With only a few exceptions, which are discussed at the end of the Chapter, most of the experimental results can be well accommodated in the three-flavor neutrino scheme described before. From these experiments the parameters that govern the phenomenon of oscillations can be deduced.

The best fit values, together with the experimental channel used to obtain them, are given in Table 4.1. Two of the mixing angles in $\mathbf{U}$, θ_{12} and θ_{23} are close to giving the maximal mixing possible, while the third one θ_{13} is small but non-zero. The masses follow a pronounced hierarchy, and we make use of it to group the experiments in the presentation that follows. The precise ordering of the masses is still unknown; Fig. 4.1 shows the two possibilities accepted by the data. This, together with the phase that would allow the violation of *CP* invariance, are the two only still unknown fundamental parameters of the neutrino that affect oscillations.

Table 4.1: Best fit values of oscillation parameters from a global analysis of the world's data [60]. The types of transitions and experiments that give information for each parameter are shown. For solar neutrinos, the L/E factor is large enough so that the neutrino loses coherence and the phase has to be averaged over. The fit assumes the normal mass hierarchy.

Parameter	Best fit	Experimental channel
$\sin^2\theta_{12}$	$0.307^{+0.018}_{-0.016}$	$\nu_e \to \nu_\alpha$ (solar), $\bar{\nu}_e \to \bar{\nu}_e$ (reactor)
Δm^2_{21}	$7.54^{+0.26}_{-0.22} \cdot 10^{-5}$ eV^2	$L/E \sim 16\,\mathrm{km/MeV}$
$\sin^2\theta_{23}$	$0.386^{+0.034}_{-0.021}$	$\overset{(-)}{\nu}_\mu \to \overset{(-)}{\nu}_\mu$ (atmospheric, beam)
$\lvert\Delta m^2_{31}\rvert \simeq \lvert\Delta m^2_{32}\rvert$	$2.43^{+0.06}_{-0.10} \cdot 10^{-3}$ eV^2	$L/E \sim 500\,\mathrm{km/GeV}$
$\sin^2\theta_{13}$	0.0241 ± 0.0025	$\bar{\nu}_e \to \bar{\nu}_e$ (reactor), $\nu_\mu \to \nu_e$ (beam) $L/E \sim 1\,\mathrm{km/MeV}$
δ_{CP}	-	-

4.1 Experiments driven by the large mass-splitting

Experiments taking neutrino data at values of $L/E \sim 500\,\mathrm{km/GeV}$ are sensitive to oscillations driven by the large mass-splitting. The largest effect can be observed in transitions of the

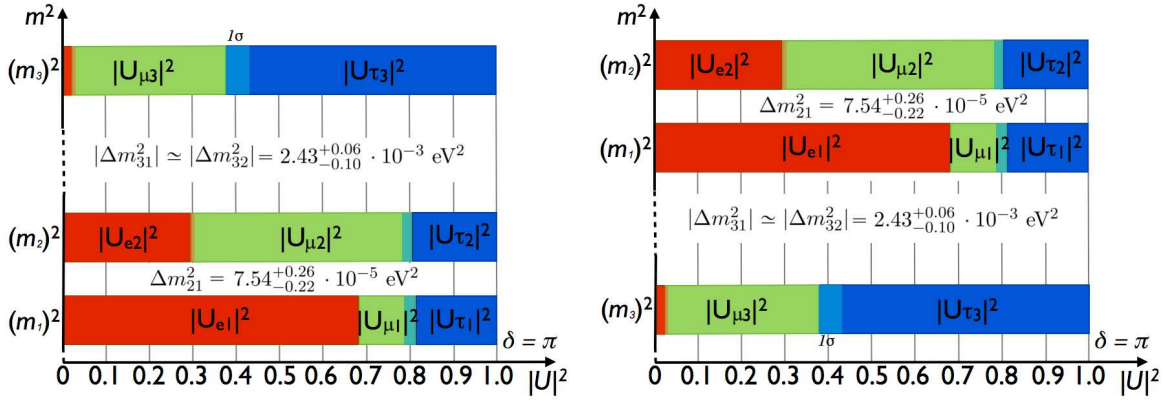

(a) Normal hierarchy **(b)** Inverted hierarchy

Figure 4.1: Diagram of the configuration of neutrino massive states accepted by neutrino oscillations data. The mass-splittings change order depending on the hierarchy. The flavor content α of the a mass eigenstate j is shown as color bars, labeled with the square of the corresponding mixing matrix element $|U_{\alpha j}|^2$. From E. Resconi.

type $\nu_\mu \to \nu_\tau$. The effect is usually expressed as the survival probability of muon neutrinos, which can be approximated rather accurately by

$$P_{\nu_\mu \to \nu_\mu} \simeq 1 - \sin^2 2\theta_{23} \, \sin^2 \left(\frac{\Delta m^2_{32} \, L}{4 \, E_\nu} \right) . \tag{4.1}$$

The fraction that oscillates into ν_τ is then given approximately by $1 - P_{\nu_\mu \to \nu_\mu}$. Even though the mixing angle involved allows the flavor conversion to be close to maximal, the appearance of ν_τ is experimentally challenging. This comes about because the tau lepton, required to identify a neutrino interaction as CC ν_τ, has a mass of 1.7 GeV [30]. Such a large mass suppresses the ν_τ CC cross-section with respect to the other neutrino flavors up until energies of several hundreds GeV [61], much higher than the energy at which most neutrino oscillation experiments operate. When the transition $\nu_\mu \to \nu_\tau$ takes place at energies lower than that, neutrinos will seem to be missing, even for an experiment capable of detecting ν_τ interactions.

4.1.1 Super-Kamiokande

The Super-Kamioka Neutrino Detector Experiment [62] is iconic in the field of neutrino oscillations. Located under Mount Kamioka in Japan, it has been operating since 1996 and is still taking data. The experiment is usually credited for providing conclusive evidence for the existence of neutrino oscillations [21].

Super-Kamiokande detects neutrinos by observing the Cherenkov light emitted by the charged lepton produced after a CC interaction with nuclei. The detector consists of a large underground water-filled cylindrical tank with photo-multipliers (PMTs) mounted on the surface of its walls. It has an energy threshold of about 4.7 MeV and an effective target volume of 50 kton.

Muons and electrons traveling faster than the speed of light of the medium produce Cherenkov light along their path, a phenomenon addressed in detail in Chapter 6. The projection of the Cherenkov cone of light on the wall has the shape of a ring. Electrons start a cascading process where $e^\pm$ pairs are emitted, which projects as fussy light ring in

the walls of the detector. Muons, on the other hand, travel almost undisturbed until they decay. If they start and stop inside the detector, they produce a ring with sharp edges. These characteristics are used to identify the type secondary particle, and hence the neutrino flavor that produced the interaction. A sketch of the detection principle with both kinds of events is shown in Fig. 4.2.

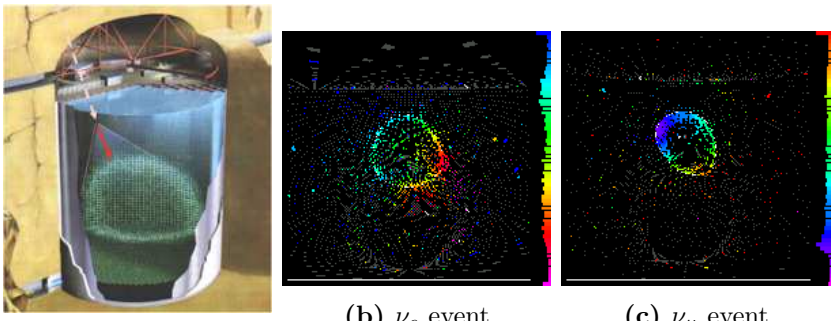

(a) Detection principle **(b)** ν_e event **(c)** ν_μ event

Figure 4.2: Detection principle and neutrino signatures in the Super-Kamiokande detector.

Super-Kamiokande measures oscillations driven by the large mass-splitting using atmospheric neutrinos, described in detail in Sec. 5.1. The analysis identifies neutrinos with energies between MeV and GeV and compares how their flux changes as they cross the Earth. Figure 4.3 shows Super-Kamiokande's most recent measurements of multi-GeV fully contained ν_μ and ν_e events. The sample has a mean neutrino energy of 4.8 GeV. Taking this value inside Eq. 4.1 and assuming $\sin^2 2\theta_{23} = 1$ allows to reproduce their results. For the neutrinos that cross the entire Earth ($\cos\theta_z = -1$), Eq. 4.1 returns a survival probability of

$$P_{\nu_\mu \to \nu_\mu}(L = 12\,700\,\text{km}, E = 4.8\,\text{GeV}) = 0.44\,,$$

where L is the Earth's diameter.

The Super-Kamiokande Collaboration has also published a study of their data with the inclusion of the appearance of a ν_τ component. The results are limited by the expected number of events coming from CC ν_τ, of about 180 for the livetime included. Still, they are able to rule out zero tau lepton events by 3.8 standard deviations [63].

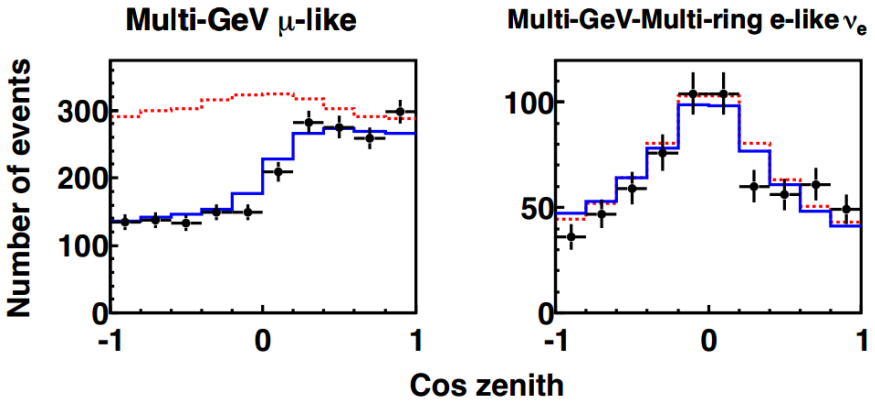

Figure 4.3: Zenith angle distribution for atmospheric ν_e and ν_μ events measured in Super-Kamiokande. Expectation with (solid) and without (dashed) oscillations shown. Taken from [64].

4.1.2 MINOS

Experiments making use of atmospheric neutrinos suffer from the uncertainties associated with the knowledge of the flux. A way of avoiding this is to utilize man-made neutrinos, produced in a controlled accelerator facility, even if this means committing to a fixed baseline. For producing a neutrino beam first it is necessary to accelerate protons and make them collide with a dense target. The results of the collisions are mainly pions, which are left to decay in flight. Electron and muon neutrinos are part of the pion decay products. This was the strategy taken for the design of many experiments, MINOS among them [65]. The specific set-up of the NuMI 3 GeV neutrino beam used for MINOS is depicted in Fig. 4.4.

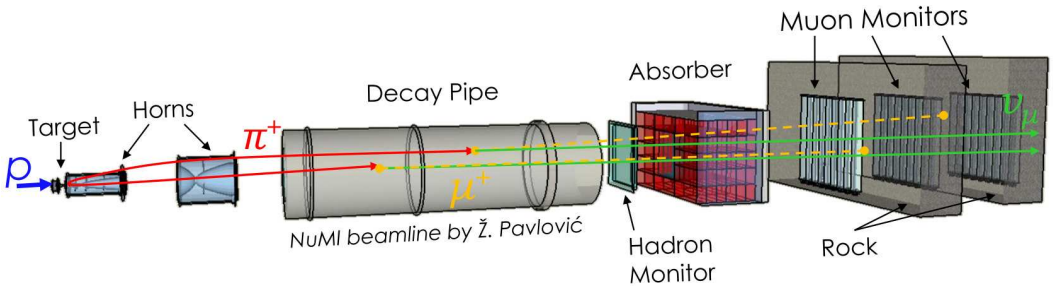

Figure 4.4: Diagram of the NuMI beam set-up used for the MINOS experiment at Fermilab.

The MINOS experiment has a far and a near detector. The detectors, designed to be as similar as possible, are magnetized steel-scintillator tracking calorimeters. The near detector is situated at the beam site, and is used to monitor the beam activity and gain a better understanding of the flux. The far detector is located at a distance of 735 km from the accelerator site and it records neutrino events that have been affected by oscillations. *Magnetic horns* [66] are used to focus the beam and switch between the neutrino and antineutrino modes of operation.

The latest results of MINOS, as published in [67], are shown in Fig. 4.5. The full data sample is shown, as well as the neutrino and antineutrino subsets. From these separate studies, MINOS found consistent mixing parameters between ν and $\bar{\nu}$ oscillations.

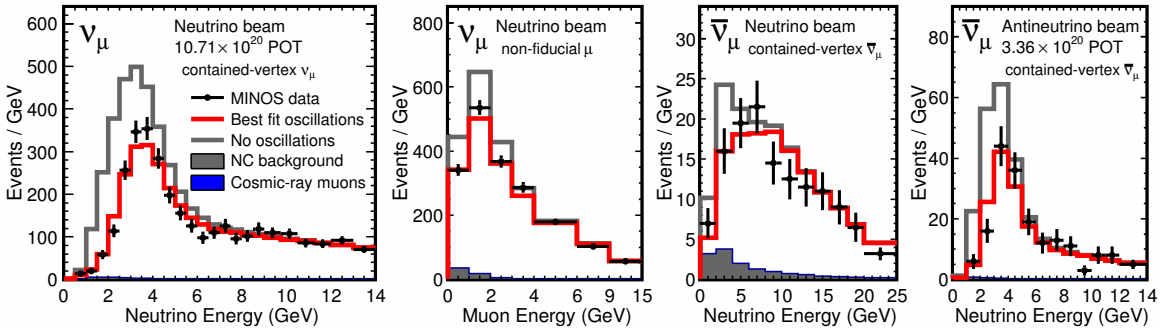

Figure 4.5: Oscillation results from MINOS. Full data sample ($\nu_\mu + \bar{\nu}_\mu$) on left panel. The panels to the right show the ν_μ sample, as well as the $\bar{\nu}_\mu$ sample, which is divided into two subsets. The best fit explains the neutrino and antineutrino data simultaneously. Taken from [67].

4.1.3 T2K

The T2K (Tokai-to-Kamioka) Collaboration [68] built on the success of Super-Kamiokande, directing a neutrino beam at the detector. The T2K experiment intentionally focuses its beam away from the detector by a few degrees, having it *off-axis*. Because of the kinematics of pion decay, doing this provides an energy spectrum that is much narrower compared to the one obtained if the beam would be on-axis (see Fig. 4.6a), with the negative effect of a decrease in the flux. The T2K experiment, like MINOS, also has secondary detectors installed close to the beam target, but the detection principle of each one is rather different. The purpose of the near detector, ND280, is not only to monitor the beam but also to study neutrino interactions at the transition region discussed in Sec. 2.3.3.

The main goal of T2K is to measure θ_{13}, whose value was only known to be smaller than about $\pi/10$ radians by the time the experiment was planned [69]. The neutrino beam has an energy centered around of $\mathcal{O}(1)$ GeV and the distance to the far detector is of 295 km. As for MINOS, the main effect is the disappearance of muon neutrinos from the original flux.

The detector of T2K, Super-Kamiokande, has the ability to identify electron neutrino events with high precision. This allows measuring the component of ν_μ which oscillates into ν_e. The leading order term for this transition is given by

$$P_{\nu_\mu \to \nu_e} \approx \sin^2\theta_{23}\, \sin^2 2\theta_{13}\, \sin^2\left(\frac{\Delta m^2_{32}\, L}{4\, E_\nu}\right), \tag{4.2}$$

where the full three-neutrino mixing scheme has been used. The probability for this transition depends on the angle of interest, θ_{13}, so any ν_e observation implies a non-zero value of θ_{13}.

In 2013 the T2K Collaboration reported, for the first time, on conclusive evidence of the appearance of ν_e in a ν_μ beam [70]. They observed 28 candidate events, with an expected background of 4.6 (see Fig. 4.6). This result is the first conclusive evidence for neutrino oscillations in appearance mode.

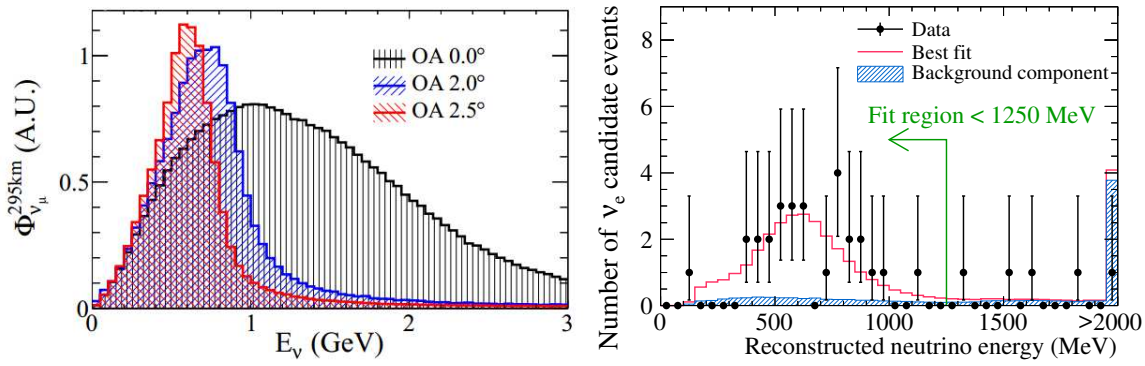

(a) Neutrino energy spectrum **(b)** Oscillation results

Figure 4.6: Beam configuration and results on $\nu_\mu \to \nu_e$ transformations at the T2K experiment, as presented in [70].

4.1.4 OPERA

The OPERA experiment is an ongoing effort to detect the appearance of tau neutrinos from a ν_μ beam [71]. The beam is produced at CERN and has an average energy of 17 GeV, well

above the production threshold of the tau lepton. The detector is located at the Grand Sasso laboratory in Italy, at a distance of 730 km from the beam.

The experiment was designed to make use of existing facilities, which explains why the probability for the oscillation searched for with this set-up is of the order of 1 %. Even though not optimal, the experiment is still unique for being the only full size experiment in the field able to detect the appearance of ν_τ on an event-by-event basis[1]. Also, the detection technique is rather different from other ongoing experiments.

The OPERA detector consists of "bricks" of nuclear emulsion plates, very much like photographic films, in which the path of charged particles is recorded. With close to eight plates per centimeter, the vertices of the events can be resolved, leading to the identification of the taus. In between the plates, slabs of lead increase the density of the detector. The bricks are positioned between layers of plastic scintillator counters, followed by a magnetic spectrometer. When an interesting event is recorded by the scintillators, the bricks are removed and analyzed to search for the decay signatures of the tau lepton.

As of summer 2013, the OPERA Collaboration has reported on three ν_τ candidates [73,74]. Figure 4.7 shows one of them, with the distinctive kink produced by the tau decay. The three events found thus far correspond to a deviation of $3.5\,\sigma$ from no observation.

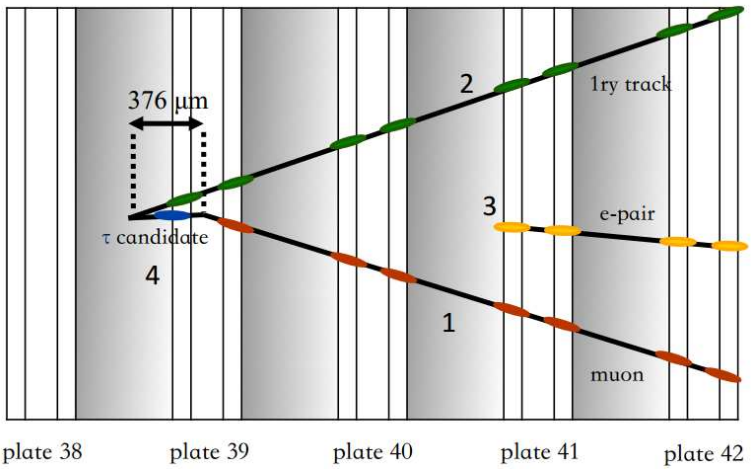

Figure 4.7: Event display of the third ν_τ candidate from OPERA. A tau lepton and a hadron come out of the primary vertex. The tau decays between the emulsion bricks, resulting in a neutrino, which is not seen, and a muon. From [74].

4.2 Experiments driven by the small mass-splitting

There are two ways in which the small mass-splitting can dominate the oscillation probabilities. One of them, already discussed, takes place when the large mass-splitting contribution is too fast to be observed. The other is when the initial system produces a neutrino which happens to have very little content of the lightest or heaviest mass eigenstate. Going back to Fig. 4.1 it can be seen that m_3 has a very small $|U_{e3}|^2$ component; its size is within the error bands of the figure. This means that the electron neutrino is almost exclusively formed by m_1 and m_2. The survival probability for ν_e in vacuum is then, to a very good approximation,

[1] The ICARUS experiment [72] can also detect ν_τ's event-wise. However, the size of the detector limits its capabilities to make oscillation measurements, and is therefore not discussed here.

described by an analogue formula to Eq.4.1,

$$P_{\nu_e \to \nu_e} \simeq 1 - \sin^2 2\theta_{12} \, \sin^2 \left(\frac{\Delta m^2_{21} \, L}{4 \, E_\nu} \right) . \tag{4.3}$$

However, unlike for the case of the large mass-splitting, both transitions $\nu_e \to \nu_\mu$ and $\nu_e \to \nu_\tau$ take place.

Nuclear fusion and fission exclusively produce electron neutrinos and antineutrinos, respectively. These reactions take place in the Sun and in nuclear reactors, turning them into source candidates for neutrino oscillations studies. The case of the Sun is of particular interest because of the high electron density in it, which makes it necessary to include matter effects. For this case, Eq.4.3 is no longer valid.

4.2.1 Sudbury Neutrino Observatory (SNO)

The Homestake experiment was the first one to observe a deficit of neutrinos when comparing their measurements of the Sun's neutrino flux with the Standard Solar Model (SSM) expectation [18]. However, the interpretation of the results depended to a large degree on the level of understanding of the Sun's neutrino emission. To avoid this problem, the Sudbury Neutrino Observatory (SNO) [75] was designed to perform both a measurement of the solar neutrino flux and a model-independent test of the oscillation hypothesis. In order to do so, SNO devised a way of separately measuring CC and NC reactions. If oscillations were to be taking place the observed CC event rate, entirely due to ν_e, should show a deficit with respect to the NC measurement, where all flavors contribute.

SNO was a water Cherenkov detector, which consisted of a spherical vessel situated in a cylindrical cavity 2 km underground in a mine. The vessel was filled with *heavy* water D_2O and surrounded by PMTs mounted on the sphere structure. To identify background muons, the cavity was filled with pure water. The possible reactions inside such a detection vessel are

$$\text{CC}: \quad \nu_e + d \to e^- + p + p \, , \tag{4.4}$$

$$\text{NC}: \quad \nu_l + d \to \nu_l + p + n \, , \tag{4.5}$$

$$\text{ES}: \quad \nu_l + e^- \to \nu_l + e^- \, . \tag{4.6}$$

The main challenge of the experiment was the separation of the different contributions. The CC and ES processes in (4.4) and (4.6) were detected via the Cherenkov light produced by the outcoming electron. The neutrino energy thresholds for detection achieved are close to 5 MeV for both reactions. The NC contribution of (4.5) was selected by detecting the gamma emission after the capture of the free neutron emitted in NC interactions, which comes with a delay of $\mathcal{O}(10\,\text{ms})$. The energy threshold for this channel is of about 2 MeV, lower than for the other channels. The experiment achieved a very precise measurement of the ratio from CC to NC neutrino interactions [76],

$$\frac{\Phi_{CC}}{\Phi_{NC}} = 0.340 \pm 0.023^{+0.029}_{-0.031}. \tag{4.7}$$

The Sun has an electron number density that varies smoothly as a function on the distance from its center, where $N_e \sim 100$ [77]. For neutrino energies above the threshold of SNO ($E_\nu > 5\,\text{MeV}$) the MSW condition is fulfilled for lower values of N_e. This means that they pass through the resonance as they exit the Sun. Their survival probability can be

approximated by the averaged adiabatic solution from Eq. 3.61. Assuming that at the Sun's core A_{CC} is at least several times larger than $\Delta m^2_{21} \cos\theta_{12}$ allows to approximate the mixing angle at production by $\pi/2$, yielding a survival probability of

$$P_{\nu_e \to \nu_e}(E \gg 1\,\mathrm{MeV}) \simeq \sin^2\theta_{12} \simeq 0.38\,, \tag{4.8}$$

which is a good first order approximation to the result given in Eq. 4.7.

The result from SNO provided more evidence that something happens to neutrinos as they travel between the Sun and the Earth. Since the result was obtained from the ratio between interaction types, it does not depend on the absolute solar neutrino flux. At the same time, the measurement demonstrates that the effect is only manifest in CC interactions, just as expected from oscillations.

4.2.2 Borexino

Interpreting the solar measurements as neutrino oscillations can lead to different conclusions, which depend on the path that the neutrinos follow. The problem arises because the matter density of the Sun is not negligible, and the potential that it induces has to be included: neutrinos from the Sun experience matter effects. How strong the matter effects are depends on the electron density and the neutrino energy (see Eqs. 3.32, 3.45, and 3.44). Since solar neutrinos have a wide energy spectrum both the matter and vacuum regime can be observed. The Borexino experiment is mentioned here because it is able to connect both regions.

Borexino [78] detects neutrinos using a spherical vessel filled with liquid scintillator, very much like SNO. The vessel is also shielded by using water, with both regions monitored by PMTs. The experiment has performed very thorough background studies, which has allowed them to make observations with a rather low energy threshold of about 0.2 MeV.

Figure 4.8 shows the solar neutrino measurements of Borexino, compared with the expectation from oscillations. For neutrino energies below 1 MeV, matter effects are very weak. For these energies, the value of A_{CC} is always smaller than $\Delta m^2_{21} \cos\theta_{12}$, so the MSW resonance cannot be fulfilled. The survival probability of electron neutrinos is well approximated by the mean value of the vacuum formula of Eq. 4.3, with

$$P_{\nu_e \to \nu_e}(E \leqslant 1\,\mathrm{MeV}) \simeq 1 - \frac{\sin^2 2\theta_{12}}{2} \simeq 0.53\,. \tag{4.9}$$

The values from Eqs. 4.8 and 4.9 are a good first order approximation to the results in Fig. 4.8.

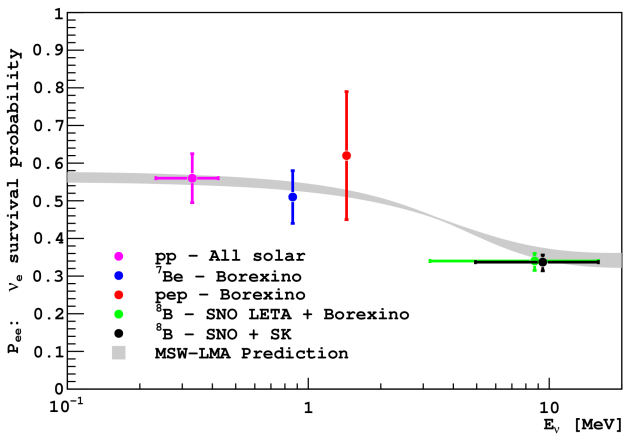

Figure 4.8: Measurements of solar neutrino survival probability compared with the prediction of oscillations including matter effects. Taken from [79].

Since solar experiments are sensitive to matter effects, they can determine the absolute value of the mass-splitting that affects them, that is Δm^2_{21}. Defining the mass eigenstate m_1 as the one with "largest ν_e content", from oscillation of solar neutrinos it follows that m_2 is heavier, thus the splitting has a positive sign.

4.2.3 KamLAND

The small mass-splitting has also been tested using neutrinos from nuclear reactors, as in the KamLAND experiment [80]. The KamLAND detector consisted of a spherical vessel filled with liquid scintillator and shielded by mineral oil. PMTs monitored the vessel, looking for signatures of neutrino interactions. The detector was located in a region of Japan with a high density of nuclear reactors, at distances from 80 km to 800 km. Around 80 % of the neutrinos come from a distance of between 140 km and 215 km.

Nuclear reactors produce electron antineutrinos with an energy of a few MeV. To measure them KamLAND was designed to have a very low energy threshold of 2.6 MeV. With such a low value, it was the first experiment to measure neutrinos being produced by radioactive material in the Earth's crust [81]. On the topic of oscillations, it confirmed the results obtained from solar measurements but using electron antineutrinos from a man-made source instead. Figure 4.9 shows their measurements as a function of L/E, where the oscillatory behavior can be easily observed. The first peak on the survival probability is located at about 34 km/MeV. Taking the approximate formula in Eq. 4.8 and the parameters in Table 4.1, the first maximum can be calculated to be around

$$\frac{\pi}{1\,267\,\Delta m^2_{21}} \simeq 33\,\text{km/MeV}\,,$$

which is again a good approximation to the observation and the full calculation shown in Fig. 4.9.

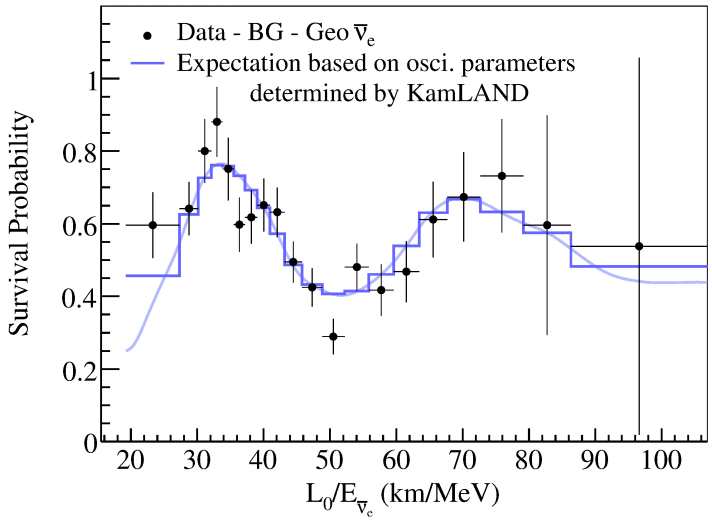

Figure 4.9: Results from KamLAND for $\bar{\nu}_e$ disappearance as a function of L/E, as reported in [82].

4.3 Experiments sensitive to three-neutrino effects

Experiments which are sensitive to only one of the two mass-splittings measure an amplitude that is approximately given by the θ_{12} or θ_{23} mixing angles. Due to its small value, the contribution of θ_{13} to the observables in these experiments is generally negligible. The results of T2K are obtained by measuring these small effects, looking for $\nu_\mu \rightarrow \nu_e$ oscillations. Another way of being sensitive to θ_{13} is by probing a region where both mass differences play a role.

Oscillations driven by both mass-splittings can be observed by using neutrinos from nuclear reactors, detecting them at distances of $\mathcal{O}(1\,\mathrm{km})$. For such distances and E_ν of $\mathcal{O}(1\ \mathrm{MeV})$, the survival probability can be approximated as

$$P_{\bar{\nu}_e \rightarrow \bar{\nu}_e} \simeq 1 - \sin^2 2\theta_{13} \sin^2 \frac{\Delta m^2_{31} L}{4E} - \cos^4 \theta_{13} \sin^2 2\theta_{12} \sin^2 \frac{\Delta m^2_{21}}{4E}\,. \tag{4.10}$$

Four experiments have measured reactor antineutrinos under these conditions, namely CHOOZ [83] and its successor Double CHOOZ [84], DayaBay [85] and RENO [86]. They all use the same detection method with which Reines discovered the particle, i.e. detection of gamma-rays after neutrino interactions with protons (full process in Eq. 1.1). It is no surprise, then, that the detectors are rather similar. Their set-ups, which have a modular approach with multiple detection units, are compared in Table 4.2.

Table 4.2: Comparison of the set-ups used by reactor experiments measuring θ_{13} from $\bar{\nu}_e$ disappearance. Compiled from [84–86].

Experiment	Reactors	Detectors and distance
Double Chooz	$1\times4.5\,\mathrm{GW_{th}}$	Single, $d \simeq 1050\,\mathrm{m}$
RENO	$2\times2.66\,\mathrm{GW_{th}}$, $4\times2.8\,\mathrm{GW_{th}}$ linear array	2 detectors $d \simeq 294\,\mathrm{m}$, $1383\,\mathrm{m}$
DayaBay	$6\times2.9\,\mathrm{GW_{th}}$ distributed	6 detectors, 3 sites $d \simeq [364 - 1912]\,\mathrm{m}$

Each detection unit is composed by concentric cylindrical tanks. The transparent inner container is filled with liquid scintillator doped with Gadolinium for capturing neutrons. This constitutes the target volume. The tank surrounding it, also transparent, contains only liquid scintillator and acts as a gamma catcher. The outermost tank has PMTs mounted on its walls and is filled with mineral oil. Known as the buffer, it shields the detector from radioactive signals. To identify and remove atmospheric muons the detection units are submerged in pure water and monitored with PMTs. Double Chooz and RENO use yet another tank for this purpose, while Daya Bay places its units in instrumented halls filled with water that can accommodate up to three of them.

The effort undergone by the three Collaborations has turned θ_{13} from the last unknown into the best-known mixing angle. Results from Daya Bay and RENO are shown in Fig. 4.10. The discovery that the value was different from zero and large, where "large" means at the edge of the limits set by CHOOZ in [69], opens the door to interesting studies. One consequence is that, with all angles having non-zero values, the imaginary phase can appear in the probability calculations and lead to *CP* violation. Other implications can be found in [87].

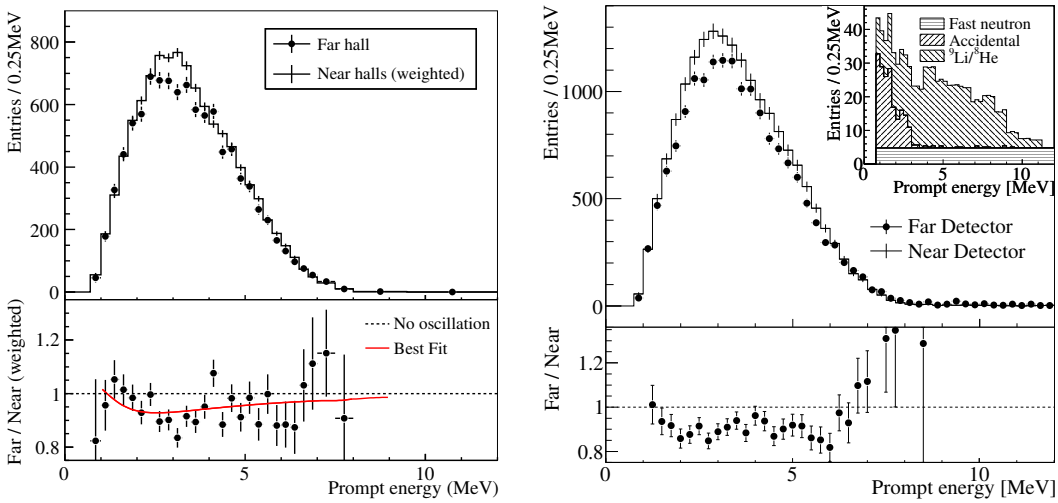

(a) DayaBay **(b)** RENO

Figure 4.10: Results on the disappearance of $\bar{\nu}_e$ from reactor experiments. Taken from [88] and [89].

4.4 Anomalous results

All of the neutrino oscillations results discussed so far can be well accommodated in the standard theory described in Chapter 3. However, a handful of experiments have reported measurements which are in conflict with it. These results come from both accelerator neutrinos and neutrinos from radioactive sources.

A preferred explanation for the tensions is the existence of oscillations between the three known neutrinos and additional *light* neutrino massive states. Since it has been proven that there are only three active neutrino families [31], the possible extra states are considered sterile, an idea that dates back to Pontecorvo [90]. The study of sterile neutrinos is outside the scope of this work, so only a general overview is given. The way in which they are presented is largely based on [91], where a more detailed discussion can be found.

Radioactive sources

The GALLEX and SAGE gallium solar neutrino detectors were tested using intense radioactive sources placed inside the detection volume. During these tests the experiments measured event rates a factor 0.02 lower than the expectation. The deficit, which amounts to 2.7 standard deviations, could be attributed to oscillations with $\sin^2 2\theta \geqslant 0.07$ and $\Delta m^2 \geqslant 0.35\,\mathrm{eV}^2$ [92].

Similarly, measurements of the neutrino output of nuclear reactors (ILL-Grenoble [93], Goesgen [94], Rovno [95], Krasnoyarsk [96], Savannah River [97] and Bugey [98]) have reported results smaller than the expectation. The issue was aggravated recently, after more accurate particle physics data were included in the calculation of the reference spectra [99]. The current average ratio between the measured and expected flux is of 0.927 ± 0.023. Although the deficit could be due to unknown processes in the physics of the reactor, if interpreted as a consequence of oscillations it results in $|\Delta m^2| = 2.4\,\mathrm{eV}^2$ and $\sin^2 2\theta \sim 0.14$. Combining the gallium data in the analysis of the reactor data does not change the best fit values [100].

Accelerator neutrinos

The LSND experiment also reported anomalous results while searching for the transformation $\bar{\nu}_\mu \rightarrow \bar{\nu}_e$ of MeV neutrinos at a distance of 30 m from its production point [101]. The experiment found an excess of more than 3 standard deviations from the background, favoring oscillations with a mass-splitting between $0.2 - 2.0$ eV^2, much larger than any other experiment.

The KARMEN experiment operated under similar conditions as LSND, but with a baseline of 17.7 m. They found no deviation from their background expectation, excluding much of the region preferred by the LSND results [102]. However, a joint analysis of the data of both experiments found that part of the parameter space was still not excluded [103].

The MiniBooNE experiment also searched for the excess found by LSND, but for both ν_e and $\bar{\nu}_e$. Operating in the $\bar{\nu}_e$ mode it obtained results compatible with those of LSND. In ν_e mode, on the other hand, the experiment found an unexpected excess of electrons which could not be explained by the same model.

Theories invoking sterile neutrinos that are successful in explaining one tension introduce disagreements among the rest of the experimental data. Demanding more than one sterile state can lead to better agreement, but only because the number of degrees of freedom increases significantly [104,105]. Even though sterile neutrinos do not seem to be the solution for the anomalies that brought the idea to light, they are an interesting possibility and experiments continue searching for them [106,107].

The current knowledge of neutrino oscillations has started probing the details of the theory that explains the phenomenon. While most experiments seem to agree, the few outliers represent a demand for verification of the validity of the predictions of oscillations. On top of that, there are still two parameters that are yet to be determined: the correct ordering of the masses and the value of the complex phase in the mixing matrix. How a neutrino telescope can contribute to the development of the field by measuring atmospheric neutrinos is discussed in the next Chapter.

5 Measuring neutrino oscillations with IceCube DeepCore

In this Chapter we explore the possible oscillation studies that can be performed with IceCube DeepCore, and neutrino telescopes in general. A neutrino telescope is a very large charge-blind Cherenkov detector. If instrumented densely enough, it can measure atmospheric neutrinos at combinations of $L/E \sim 500\,\mathrm{km/GeV}$, where the effects of oscillations due to the large mass-splitting Δm^2_{32} are close to maximal.

We start the discussion by having a closer look at cosmic rays and atmospheric neutrinos. The IceCube DeepCore detector is introduced afterwards. Then we combine the two and cover the possible oscillation measurements and their limitations. At the end we briefly discuss the simulation tools required. Note that even though IceCube DeepCore is used as the reference detector, the information gathered and conclusions reached in this Chapter are general enough to apply to similar projects.

5.1 A neutrino beam from cosmic rays

Very high energy particles, known as cosmic rays, bombard the Earth continuously from space. They are mainly protons and nuclei, arriving isotropically from all directions. These cosmic rays have been measured from MeV to EeV energies following a steeply falling spectrum, which can be approximated by several power law functions [108]. Their origin is still unknown, although there are indications that supernova remnants could be responsible for the flux up to PeV energies [109].

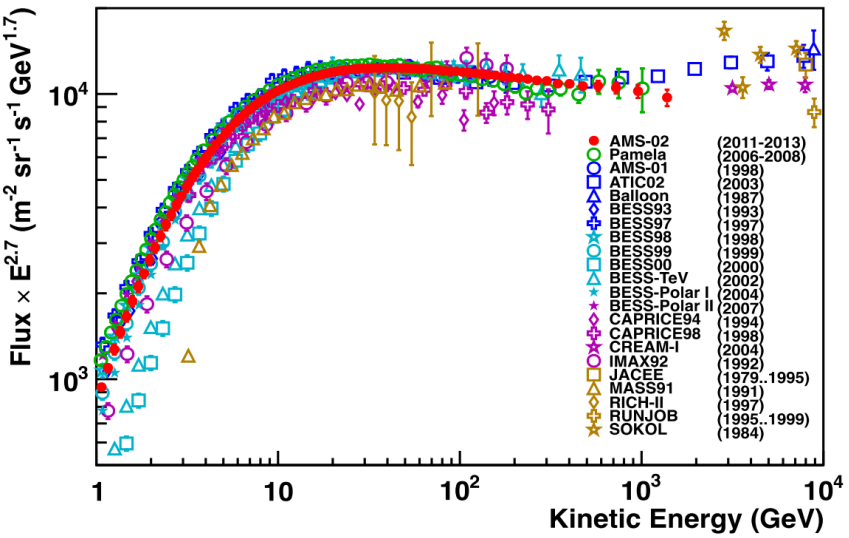

Figure 5.1: Direct measurements of the energy spectrum of cosmic ray protons. Taken from [110].

The low energy component has such a high flux that it can be measured directly by relatively small experiments, with detection areas of $\mathcal{O}(1\,\mathrm{m}^2)$. Satellites and balloons can observe the primary particles before they interact with the molecules in the atmosphere. Spectroscopic analysis allows one to determine the energy and type of particle detected with high precision. A compilation of direct measurements of the proton component of cosmic rays is shown in Fig. 5.1, where the flux has been multiplied by $E^{-2.7}$. The flux at the highest energies shown is so small that direct detection becomes technically too challenging, and the particles have to be measured by terrestrial arrays. These arrays detect cosmic rays indirectly by looking at the secondary particles produced after they interact in the atmosphere. The interaction typically happens at a height of about 25 km above sea level, where a shower of particles is initiated. Figure 5.2 shows a diagram of a typical air shower including the different types of secondary particles produced. Terrestrial arrays determine the energy and type of primary particle from studying the shower profile, a method which is much less precise than direct observation.

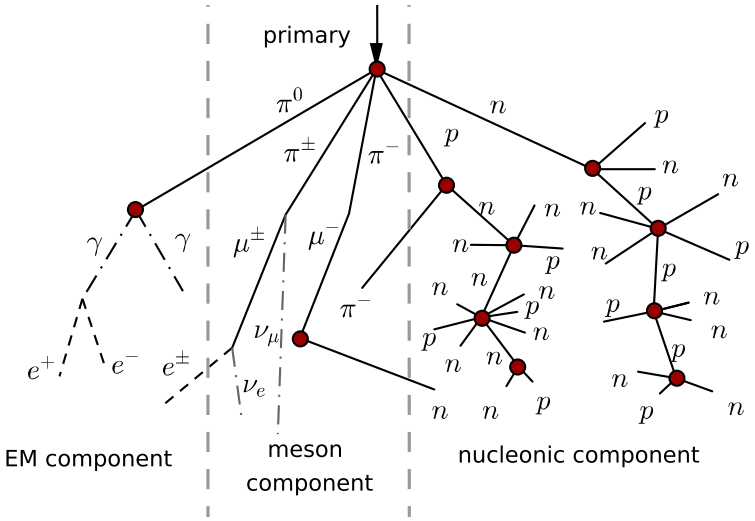

Figure 5.2: Diagram of the development of a cosmic ray interaction in the atmosphere.

During the development of the air shower muons and neutrinos are produced. They originate in weak decays of hadrons as shown Fig. 5.2. A typical interaction is

$$\begin{aligned} p + N \rightarrow X + \pi^{\pm},\, K^{\pm} \\ \hookrightarrow\ \mu^{\pm} + \overset{(-)}{\nu}_{\mu} \\ \hookrightarrow e^{\pm} + \overset{(-)}{\nu}_{e} + \overset{(-)}{\nu}_{\mu}\,. \end{aligned} \tag{5.1}$$

The decay of pions and kaons results in a comparable flux of electrons, muons and neutrinos.

5.1.1 Atmospheric muons

The atmospheric muons produced in air showers with energies above a few hundred GeV can travel long distances before they decay. They are able to penetrate deep into the Earth, depending on their energy and the material that they are crossing [30]. Figure 5.3 shows the measured vertical muon intensity integrated over energy as a function of depth, taking water

as the reference material. Only at a depth of about 15 km the flux starts to be dominated by muons from CC ν_μ interactions which, oscillations set aside, is constant.

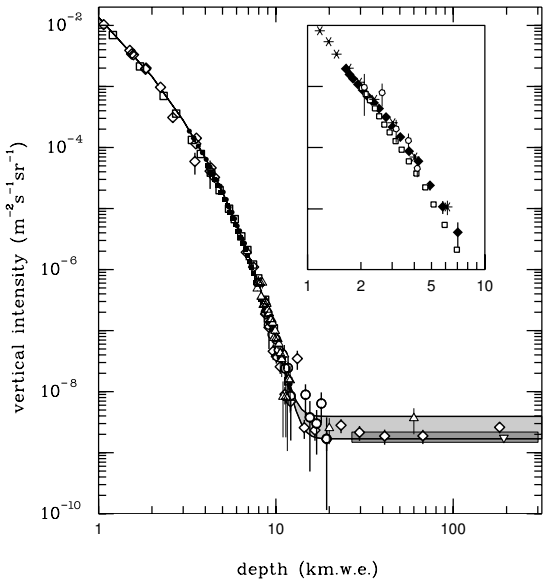

Figure 5.3: Measurements of vertical intensity of the flux of atmospheric muons as a function of depth. Includes the muons produced in the shower, as well as the ones from subsequent ν_μ interactions of neutrinos from the shower. This last component is independent of depth, which makes the curve constant when it dominates. Taken from [30].

The flux of atmospheric muons is so strong that experiments searching to detect charged particles from neutrino interactions have to be shielded against it. Taking the cross-sections from Fig. 2.6, the interaction length for neutrinos with $E_\nu = 10\,\text{GeV}$ in water is of $\mathcal{O}(10^9\,\text{km})$. This has to be compared with muons of the same energy, which deposit about 200 MeV of energy per meter when crossing water [111]. A first step to reduce the muon signals, as it can be deduced from Fig. 5.3, is to build the detector underground. To complement this, active rejection of events that seem to enter the volume of interest is typically used.

5.1.2 Atmospheric neutrinos

From the cosmic rays interactions in the atmosphere a stable flux of neutrinos is produced. Notable attempts to model it have been made by Honda *et al.* [112], Barr *et al.* [113] (commonly referred to as the "Bartol" model) and Battistoni *et al.* [114] (which uses the FLUKA Monte Carlo). The spectra that result from the different models are compared in Fig. 5.4.

While there are differences in the predictions, the models are in agreement on the global characteristics of the spectrum. For the region of interest, of E_ν between 10 GeV and 100 GeV, muon neutrinos follow a spectral index close to 3, which becomes slightly steeper for energies higher than about 200 GeV (close to 3.15). The ratio of $\nu_\mu : \bar{\nu}_\mu$ starts at about 1.25 at 10 GeV, increasing to close to 1.3 at 500 GeV.

Electron neutrinos behave differently. This can be understood using the process in Eq. 5.1 as an example, where it is possible to see that the ν_μ component comes from the muon production and the muon decay, which contribute roughly equally. The ν_e component, on the other hand, comes only from the muon decay, thus the decay in-flight of the muon affects the electron neutrino flux more strongly. Models agree that the ratio $\nu_e : \bar{\nu}_e$ is of 1.2 at 10 GeV, but have rather different predictions for higher energies (see (b) in Fig. 5.4). The same holds for the spectral index, which according to Honda is of about 3.5 and constant up to E_ν of 1 TeV, but has different predictions in the other models shown.

Measurements of the atmospheric neutrino spectrum have been reported by Frejus, Super-Kamiokande, AMANDA and IceCube. A compilation of them can be seen in Fig. 5.5. The

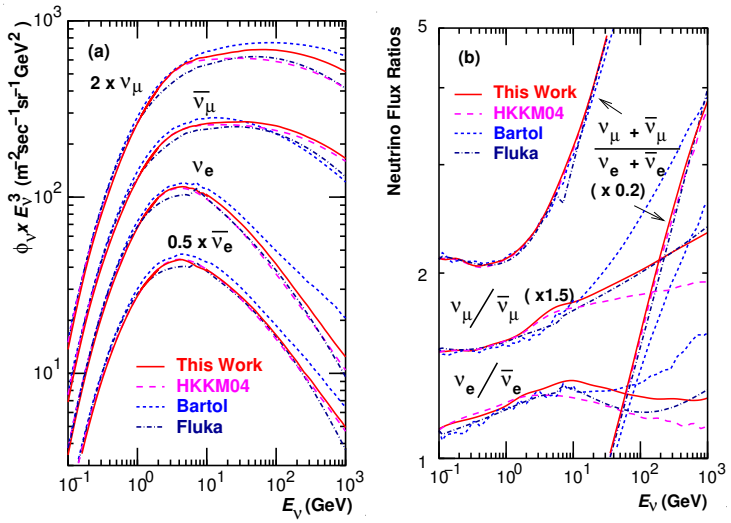

(a) Energy spectrum **(b)** Flavor ratios

Figure 5.4: Comparison of models of the flux of atmospheric neutrinos. The label "This Work" is an updated version of the HKKM04 model. Taken from [112]

region of interest for standard oscillations is that covered by Super-Kamiokande (ν_μ) and Frejus (ν_e and ν_μ). The measurements are not sensitive enough to discriminate between the models mentioned before. Different models are represented by a band labeled "conventional"[1]. The measurements do, however, constrain the normalization and spectral index of the flux.

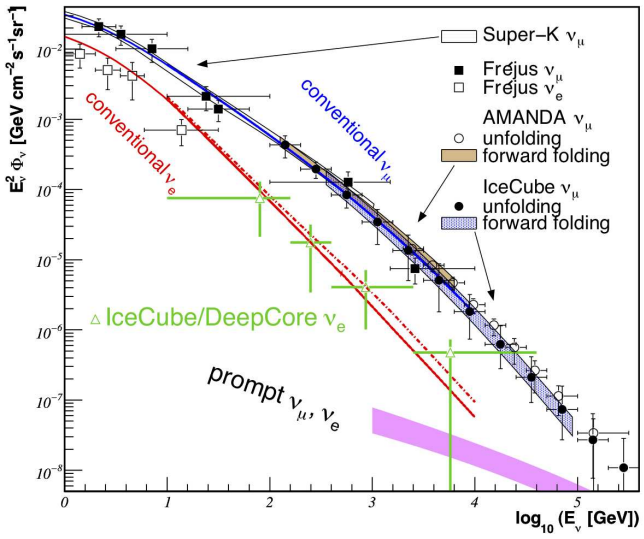

Figure 5.5: Measurements of the atmospheric neutrino flux. The conventional lines are extrapolations from the models in Fig. 5.4. Taken from [116].

5.2 The detector: IceCube DeepCore

The IceCube Neutrino Observatory [117] is an ice Cherenkov neutrino telescope, buried 1.5 km deep in the Antarctic ice at the geographic South Pole (see Fig. 5.6). The detector consists of 5 160 light sensors distributed over a volume of a cubic kilometer, which monitor the ice

[1] The flux of atmospheric neutrinos is sometimes divided in conventional and prompt. The conventional flux comes from processes lilke that in Eq. 5.1, while the prompt flux comes from the decay of charmed mesons. This flux is expected to be less steep but only relevant for measurements at E_ν of 1 PeV or higher (a recent flux estimate can be found in [115]). Because of this, it is not discussed in this work.

permanently. At the surface it has an array of ice filled tanks that detect cosmic rays via air showers, named IceTop.

The main goal of IceCube is the detection of neutrinos emitted outside the solar system. Atmospheric neutrinos are a source of background for this kind of search, as well as a potential signal for others. In order to use atmospheric neutrinos the detector was more densely instrumented towards its bottom using more efficient sensors. This allows the instrument to detect neutrino interactions of lower energies in this particular volume. The subarray is called DeepCore [118].

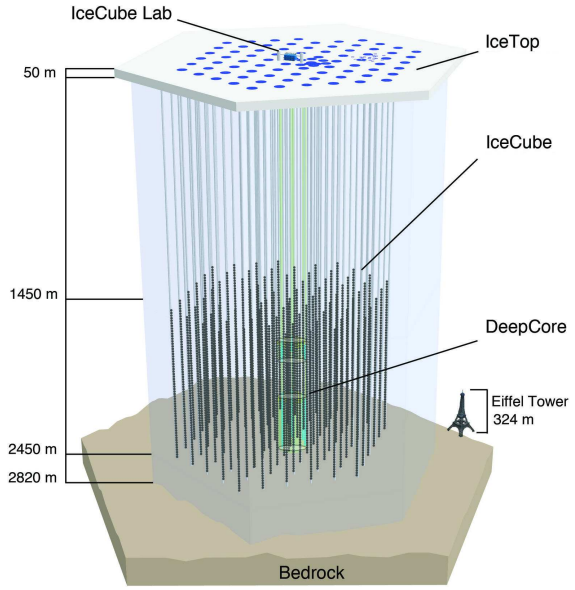

(a) Schematic view

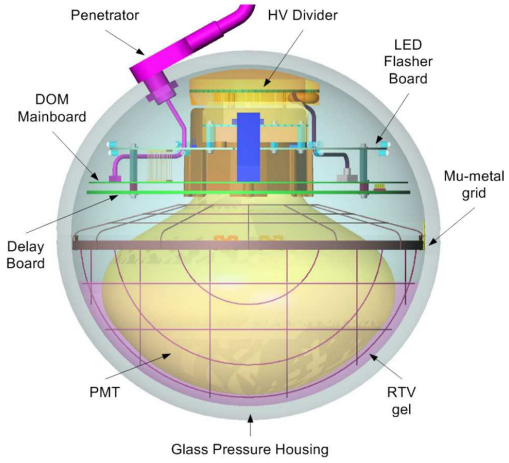

(b) Digital Optical Module

Figure 5.6: The IceCube Neutrino Observatory and its detection unit.

5.2.1 Principle of operation

Charged particles traversing a medium faster than the local speed of light emit electromagnetic radiation, a phenomenon known as the Cherenkov effect (discussed in Sec. 6.1.1). The operation of IceCube relies entirely on the detection of these photons, together with their arrival time and the position of the sensor that records them.

The photons are recorded by individual detection units, known as Digital Optical Modules (DOMs). The main components of a DOM are a 10" Hamamatsu photomultiplier (PMT), a mainboard with the necessary electronics to supply power and digitize the signal, an array of light emitting diodes and a 13" glass sphere, which encloses all of the above [119].

The detection of a photon starts when it arrives at the DOM and crosses the 0.5" thick glass sphere. Leaving the sphere it enters a gel which is used to optically couple the sphere and the PMT. Once in the PMT, the photon can be absorbed by a photocathode, emitting an electron which is then amplified. The resulting signal is readout as a change in the voltage of the PMTs anode, and given to the mainboard electronics.

The voltage at the PMTs anode is fed to three pieces of circuitry, one for triggering and two more for reading out the signal in high and low resolution modes. The high resolution readout path consists of two custom 10-bit analog-to-digital converters, known as ATWDs, operated at 300 mega samples per second (MSPS). An ATWD has 3 input channels at

different amplification levels, and capture results in the recording of 128 analog samples at each one of them. A signal is readout with a maximum duration of 426 ns and a bin size of about 3.3 ns [120]. For signals that might take a longer time to develop, a low resolution converter (fADC) is available. The fADC is operated at 40 MSPS, and capture consists of 256 samples, which cover an interval of a little over 6 μs with a bin size of 25 ns [121].

When a DOM records a signal with an integrated charge above the 0.25 PE threshold it communicates with its nearest and next-to-nearest neighbors to determine if any of these DOMs have also crossed the threshold. The allowed time interval is ± 1 μs. This search is repeated for each DOM that is found above threshold. When two or more DOMs fulfill the criteria, they are given the "Hard Local Coincidence" (HLC) tag, and are readout both in high and low resolution modes. Modules above the threshold but without an HLC tag are readout in low resolution mode only. A summarized comparison between the two readout modes with their respective conditions can be found in Table 5.1.

Table 5.1: Readout modes of the IceCube Digital Optical Modules. From [121].

Readout path	Condition	Sampling rate	Capture	Resolution
ATWD	HLC	300 MSPS	128 samples	3 ns
fADC	Above threshold	40 MSPS	256 samples	25 ns

The output of reading out a DOM is a digitized waveform. An unfolding procedure is conducted to determine the time at which the signal appeared, its duration, and the number of photons that created it. Given the finite time and voltage resolutions, individual photons cannot always be discerned. Instead, the concept of *pulses* is introduced. A pulse describes the charge Q deposited in the DOM by a bundle of photons during a time interval $t + \Delta t$. The time interval can vary according to the results from the unfolding, but is typically of the order of the resolution of the capture method used. This means that multiple pulses can appear in one DOM during one event, which lasts for several microseconds. The charge is normalized to the single photon case, and expressed in units of photoelectrons (PEs). These two quantities, charge Q and time t, are the detector's observables which are available for analysis.

5.2.2 Detector layout

The DOMs are arranged in strings. Each string supports 60 DOMs and there are 86 of them. The 80 "standard" IceCube strings are instrumented from a depth of 1 450 m to 2 450 m, with a spacing of 17 m between sensors. The layout of the strings follows a concentric hexagonal pattern, with a typical distance of 125 m to the nearest neighbor, as it can be seen in Fig. 5.7a [117].

In addition there are 8 dedicated DeepCore strings, which use PMTs with 35 % higher quantum efficiency with respect to the standard ones. Six of these surround the central IceCube string. They follow the same hexagonal pattern with a smaller separation, of 70 m. The two remaining strings are deployed inside the DeepCore region. DOMs on DeepCore strings are 7 m apart and only start at a depth of 1.75 km, with a large gap between the positions of the 10th and 11th DOM (see Fig. 5.7b) [118].

The DeepCore fiducial volume, as is used later on in the data analysis, is defined in the $x - y$ plane by the DeepCore strings, the central string, and the first hexagon of standard IceCube strings (see Fig. 5.7a). In the z direction, the volume starts at a depth of 2 100 m.

Standard IceCube strings have 18 DOMs below this depth; DeepCore strings have 50. Figure 5.7b is a sketch of the side projection of the detector and the fiducial volume.

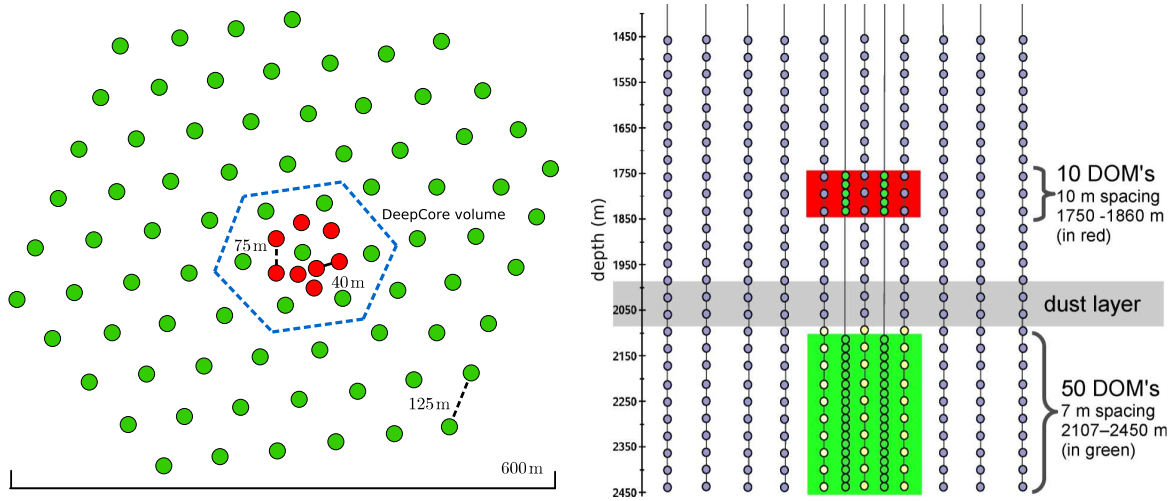

(a) Footprint view **(b)** Side view

Figure 5.7: Top and lateral projections of the IceCube detector. The DeepCore fiducial volume is marked in blue (a) and green (b). Panel (b) taken from [122].

5.2.3 Detection medium

The ice of the Antarctic glacier was formed from snow after it was compacted under its own weight in a very slow process. The result of this process is a layered structure, with an air bubble content that decreases with depth. The clearest ice starts at depths of around 1.4 km. There the medium has a transparency that is not possible to match in laboratory conditions [123].

The optical properties of the ice, i.e. scattering and absorption, affect the trajectory of the light produced by charged particles. These properties are studied by using data taken by a "dust logger" device, and also with data acquired by the experiment itself while operating in LED flashing mode. The data are fit by assuming that optical properties change with depth, but are constant in the $x - y$ plane. Figure 5.8 shows the result from two such fits, for light of 400 nm of wavelength. The absorption coefficient, shown in the left panel, is defined as the average distance traveled by a photon before it is absorbed. The geometrical scattering b, which determines the average distance between successive scatters as $1/b$, is used to define an effective scattering coefficient $b_e = b \cdot (1 - \langle \cos\theta \rangle)$, where θ is the deflection angle at each scatter point [124].

The most striking feature is the existence of a region at a depth of about 2.1 km with abnormal values. The reason for this is an unusually high accumulation of dust; the existence of this layer was also observed by the dust logger. Aside from the dust layer it can also be seen that the ice has a complicated small scale structure, with absorption and scattering coefficients that vary as much as 30 % from their mean values.

Apart from the compacted ice, the photons travel through a second kind of ice structure before reaching the DOMs. The construction of IceCube required drilling holes and melting columns of ice to deploy the instrumentation. The refreezing of the water in the holes left ice columns with optical properties rather different from those of the bulk of the ice. This

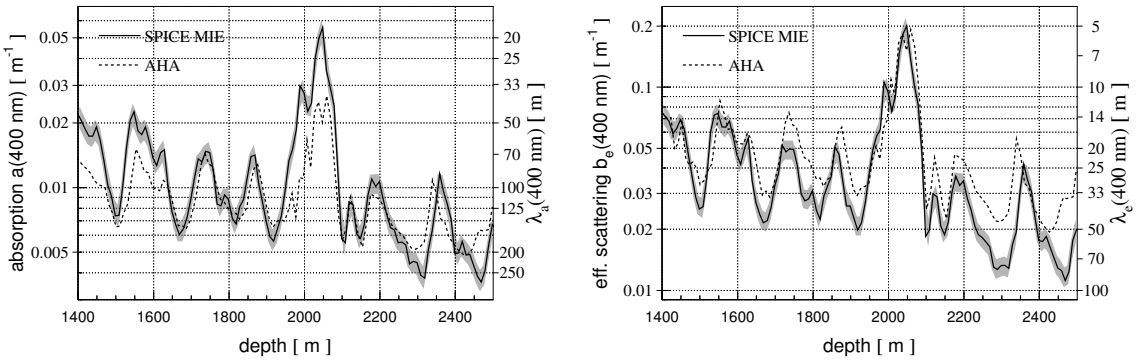

(a) Absorption **(b)** Scattering

Figure 5.8: Optical properties of the South Pole ice inferred from two different studies. From [124].

borehole ice is modeled by assuming a dense concentration of bubbles, with the best fit given by a scattering length of 50 cm. This can be compared with the effective scattering length from Fig. 5.8b, which in the dust layer is of about 5 m.

5.3 Measurable effects of neutrino oscillations

In order to measure the phenomenon of oscillations, the first requirement for the detection method is to be able to differentiate between neutrino flavors. Recall from the weak Lagrangians (Eqs. 2.3 and 2.4) that flavor sensitivity is only achieved in CC interactions. The flavor discrimination can be done by using differences in the recorded signals like the rings in Super-Kamiokande, detection processes unique to a certain flavor like the inverse beta decay in reactor experiments, and detector threshold effects, among others. Neutrino telescopes rely on muon tagging, cross-section effects and flux differences to statistically separate neutrino flavors.

5.3.1 Classification of neutrino events

The detection principle together with the separation of the light sensors limits the ability of IceCube DeepCore to differentiate the individual particles coming from a neutrino interaction. Muons are the only ones that can be identified with some confidence, since they can travel distances comparable to the spacing of the detector. Hadrons, electrons and tau leptons, on the other hand, decay and/or interact and initiate cascades of particles that develop over distances of a few meters[1].

Table 5.2 sketches the signatures that can be expected for different deep inelastic scattering (DIS) neutrino interactions in the detector. Muons come from the interaction vertex of CC ν_μ and from the tau decay of a small fraction of CC ν_τ interactions. Whether the event looks elongated or not depends on the energy that is taken by the muon. All other processes end up in hadronic or electromagnetic cascades, which appear too similar to the detector to be discriminated. The description of the light deposition of individual events requires that we include the optical properties of the medium.

[1] The details of propagation of charged particles in ice are given in Chapter 6.

Table 5.2: Possible experimental signatures of neutrino interactions in IceCube DeepCore. Dashed lines represent neutrinos, orange lines are muons, red lines are particles originated in a hadronic cascade and blue lines are electrons and photons.

Interaction		Secondary particles	Detector signature
CC ν_μ	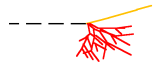	μ track and hadronic cascade	Track with cascade
CC ν_τ	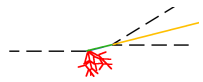	τ decays into μ ($\sim 17\,\%$ b.r.)	
	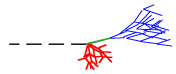	τ decays into e / hadrons	
CC ν_e	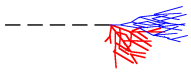	Hadronic and EM cascades	Cascade
NC ν_α		Hadronic cascade	

5.3.2 Neutrino observables

Once the flavor of the interaction is known, two more variables can be included to study oscillations: the energy and the propagation distance of the neutrino (see Eq. 3.23). The energy of a neutrino can be estimated from the light in the event by assuming one of the situations in Table 5.2. Tracks and cascades have distinct but known ways of losing energy and it is possible to connect the pattern of photons deposited with the original energy of the particles involved.

The propagation distance of a neutrino produced in the atmosphere can be approximated, within an error of a few kilometers, from its arrival direction. A direction can only be assigned with confidence to sufficiently elongated events, which explains why we need a muon in the final state[1]. The propagation distance L is given by

$$L^2 = r_i^2 + r_p^2 - 2\, r_i\, r_p \cos\left[\theta_z - \arcsin\left(\frac{r_i}{r_p}\sin\theta_z\right)\right] . \tag{5.2}$$

Here r_i and r_p are the radii of the neutrino interaction and production points, respectively, measured from the Earth's center, and θ_z is the zenith angle. The definition of the quantities involved can be seen in Fig. 5.9.

If the approximation $r_i \simeq r_p \simeq r_E$ is taken, where r_e is the radius of the Earth, Eq. 5.2 simplifies to $L \simeq 2\, r_E \cos\theta_z$. To first order, the propagation distance depends linearly on $\cos\theta_z$. This variable is the one used for showing the effects of oscillations of neutrinos that cross the Earth.

[1] Studies within the IceCube Collaboration have shown indications that events without a clear muon can also be assigned a direction, but only at energies of $\mathcal{O}(100\,\text{TeV})$ and higher.

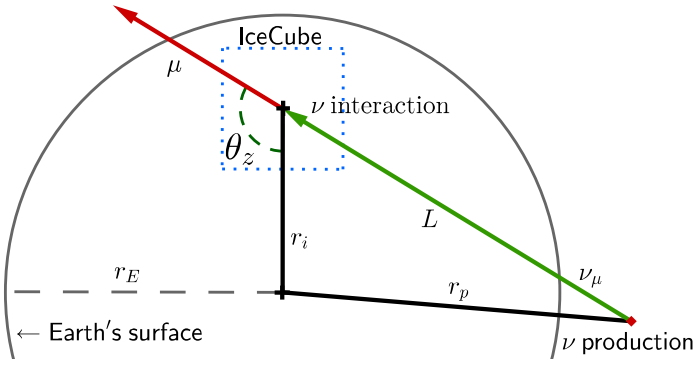

Figure 5.9: Diagram of the definition of zenith angle θ_z and propagation distance L for atmospheric neutrinos detected in IceCube DeepCore.

5.3.3 Possible studies on neutrino oscillations

Given the source, detector characteristics and the variables involved, the following studies can be performed:

Measurement of Δm^2_{32} and $\sin^2\theta_{23}$ from $\nu_\mu + \bar{\nu}_\mu$ disappearance

The strongest flux modification that oscillations produce is experienced by muon neutrinos and antineutrinos, which transform mainly into $\overline{\nu}_\tau$. The phenomenon is driven by the large mass-splitting, Δm^2_{32}, so θ_{12} can be ignored. Matter effects can modify the expectation from vacuum oscillations depending on the energy of the neutrino. In the Earth's mantle ($N_e \simeq 2.5$) the resonance condition is fulfilled for $E_\nu \simeq 6\,\text{GeV}$, with θ^m_{13} going to $\pi/2$. For higher electron densities, the resonance happens at lower neutrino energies. At $E_\nu \sim 10\,\text{GeV}$, $A_{\text{CC}} \gg \Delta m^2_{31}\cos 2\theta_{13}$ and the effective mixing angle θ^m_{13} tends to $\pi/2$ (see Fig. 3.4). For $E_\nu \geqslant 10\,\text{GeV}$ the disappearance of muon neutrinos can be approximated by the two-neutrino formalism in Eq. 4.1.

The expected survival probability for $\overline{\nu}_\mu$ in the two-neutrino scheme in vacuum, as a function of energy and arrival angle, is shown in Fig. 5.10 (left). The calculation, performed using the best known oscillation parameters quoted in Table 4.1, shows the existence of a region in the parameter space where most muon neutrinos oscillate into a different flavor, ν_τ in this case.

Going from high to low energies, the minimum survival probability appears first for neutrinos with energies of about 25 GeV that cross the entire Earth ($\cos\theta_z = -1$). For lower energies the minimum shifts towards a more horizontal direction. The survival probabilities for two neutrino energies, 25 GeV and 12 GeV, are shown on the right-hand side of Fig. 5.10, where the shift of the oscillation minimum can be observed. Note that, in both cases, the survival probability around the horizon, where the travel distance L is of $\mathcal{O}(10\,\text{km})$, stays close to one, with oscillations not modifying the flux in that region. In order to observe the shifts in the oscillation minimum, both the propagation distance and the neutrino energy of each event have to be recovered. This is possible for CC ν_μ events.

For a study looking to measure θ_{23} and Δm_{32} with atmospheric neutrinos of energies of 10 GeV and higher, a sample can be selected by focusing primarily on removing atmospheric muons. As $\overline{\nu}_\mu$ is the main component of the atmospheric neutrino flux, the background that could be introduced by other neutrino flavors is not of concern. A long-range muon in the final state is desired since it allows performing a reliable angular reconstruction and provides a straight-forward tagging strategy.

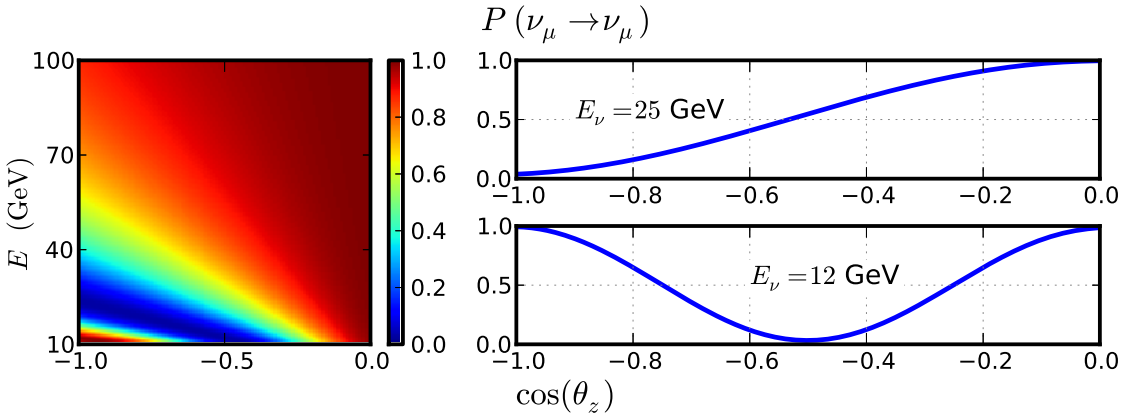

Figure 5.10: Survival probability $P(\nu_\mu \to \nu_\mu)$ for neutrinos that cross the Earth. Calculated using using the two-neutrino scheme in vacuum. The left panel shows P as a function of neutrino energy and arrival zenith angle. The panels to the right show P for two energy bands. Obtained using the values of Table 4.1.

Possible *CPT* violation from $\nu_\mu/\bar{\nu}_\mu$ disappearance

The disappearance probabiliy of atmospheric muon neutrinos with $E_\nu \geqslant 10\,\text{GeV}$ can be well approximated by the two-neutrino formalism in vacuum (see previous study). As the imaginary phase δ_{CP} does not enter in the description, neutrinos and antineutrinos should have the same oscillation patterns. If the sample of the study mentioned before can be divided in ν_μ and $\bar{\nu}_\mu$, *CPT* invariance could be tested by fitting oscillation parameters from each sample subset (similarly to MINOS, see Section 4.1.2).

This study requires correct identification of muons, and a final sample with a large antineutrino component. In the case that the detector is capable of correctly separating single muons from the rest of the particles in ν_μ CC interactions, the distribution of events as a function of the kinematic variable y can be recovered. From Chapter 2, the cross-section for antineutrinos depends on y while the one for neutrinos does not. Using different regions of the reconstructed y distribution could yield a changing $\nu/\bar{\nu}$ ratio. Obtaining oscillation parameters for samples with different $\nu : \bar{\nu}$ contributions can allow determining if *CPT* invariance is violated.

Matter effects and mass hierarchy with ν_μ

The resonance conditions for θ_{13}^m are fulfilled in the mantle by neutrinos with an energy of about 6 GeV. For higher electron densities, the neutrino energy required to meet the resonance decreases. Parametric effects, such as those described in Section 3.3.3, also play a role for neutrino trajectories that go through the Earth's core ($\cos(\theta_z) \geqslant 0.8$), where $N_e \simeq 5.5$. However, both of these effects are strong only for neutrinos, if the hierarchy is normal, and for antineutrinos if it is inverted[1].

An example of how the oscillation pattern differs for the two hierarchies is shown in Fig. 5.11. For neutrinos with an energy of 25 GeV the oscillation probability deviates by less than 1 % from the vacuum case. The situation, however, changes for lower energies. At 12 GeV the matter potential distorts the simplified picture of the previous studies by 10 % for

[1] The phenomenon is explained in Section 3.3.3. The specific case for the Earth has been recently covered in [125, 126].

neutrinos crossing the entire Earth. The modification can be as large as 30 % for neutrinos with an energy of 7 GeV.

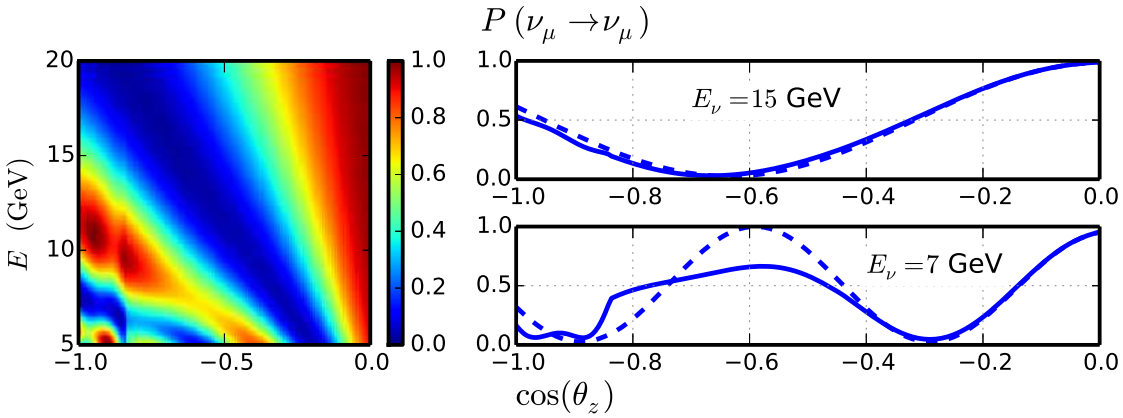

Figure 5.11: Survival probability for muon neutrinos for Earth crossing trajectories. Matter effects are included. The solid line corresponds to the case of normal hierarchy, dashed for inverted. Values from Table 4.1.

Atmospheric neutrinos contain both ν_μ and $\bar{\nu}_\mu$. For a detector that cannot separate interactinos of neutrinos from antineutrinos the matter effects in Fig 5.11 have to be averaged. Below 10 GeV, the atmospheric neutrino flux of ν_μ and $\bar{\nu}_\mu$ is almost equal, but the cross-section is still a factor 2 higher for neutrinos. Unless the acceptance of the data selection turns out very different for the two particles, the same ratio will hold and the samples analyzed will be dominated by muon neutrinos. In this case measuring a deviation from the vacuum expectation would mean that Nature follows a normal hierarchy. Conversely, no deviation would point to the inverted hierarchy being the correct one.

It is important to point out, once again, that the modeling of neutrino interactions at $E_\nu \sim 6$ GeV is not as well understood as for higher energies. It was mentioned in Section 2.3.3 that the transition between DIS single-quark interactions and interactions with a coherent nucleus is not well understood. Any attempt to perform a measurement in this region should be accompanied by thorough studies demonstrating how this lack of knowledge affects the confidence in the result.

Detection of ν_τ appearance

The events that disappear from the $\overline{\nu}_\mu$ component can appear as ν_τ in the detector. Most of the ν_τ interactions would end up in some sort of cascading process, as shown in Table 5.2, while a small fraction ends up producing muons. Only the energy, and not the direction, could be fit from the majority of these events.

A search for ν_τ appearance would need to take into account two other issues related both to the atmospheric neutrino flux and the interaction kinematics. The first one is the irreducible background that neutral currents from all flavors generate for a search of cascade-type events. The second is the fact that the cross-section for ν_τ interactions is suppressed due to the mass of the tau lepton, a problem that also limits the ability of Super-Kamiokande to study the topic. Nevertheless, the situation for IceCube DeepCore is better, since its size allows it to measure atmospheric neutrinos with higher energies. At about 25 GeV the cross-section ratio for neutrino-nucleon interactions $\sigma_{\nu_\tau}/\sigma_{\nu_\mu}$ is already 0.5 [61].

Compared with the analyses previously discussed, studying the appearance of ν_τ requires a different kind of event selection and data anlysis. The analysis would have to center around the observed energy of an event. Improvements could come from having some angular resolution for cascades, as this would allow for attempting a measurement of the up/down flux asymmetry, as discussed in [127].

Given the different possibilities, the measurement of muon neutrino disappearance is a logical choice for a first oscillation analysis using IceCube DeepCore. The study searches for a strong effect that, while not being new, has only been recently observed at such high energies. Moreover, it defines a good starting point for the other potential measurements. Assuming that the standard oscillation interpretation holds, the expected result is partially known. The study allows one to test the capabilities of the detector and reconstruction techniques, and assess their uncertainties. For all these reasons, developing a muon neutrino disappearance analysis was chosen as a goal for this work. From this point on, the discussion focuses mainly on the needs of this particular study.

5.4 Simulation tools

The IceCube detector has to rely heavily on simulation tools to interpret its data. These tools can be divided into those involved in the simulation of the primary cosmic ray flux, the propagation of particles, and the detector's response. Standard particle physics software is used for simulating the interactions of neutrinos, while the propagation and detection are IceCube specific. Both are described next.

Note that even though cosmic rays are the source of both neutrinos and atmospheric muons, the components are simulated separately. The emphasis is put on the correctness of the neutrino simulation. A large set of variations of the neutrino flux are generated in order to reproduce the effects from different uncertainties. The details on the atmospheric muon simulation, on the other hand, are not as relevant. The event selection will try to remove this contribution entirely, and knowing the overall characteristics of their spectrum is enough for the task.

Neutrino interactions

Neutrinos are injected at the surface of a cylinder that rotates around the center of the detector. They are forced to interact in a volume that surrounds and includes IceCube, which is large enough to include events where the interaction takes place outside the instrumented volume but a particle could still leave pulses in the DOMs. Individual events are weighted according to their interaction probability and incoming flux.

The flux of neutrinos is taken from the parameterization of Honda *et al.* [112], which does not include the effects of oscillations. The zenith angle distribution for the site-specific prediction of Honda for the South Pole is shown in Fig 5.12. The flux is expected to be up-down symmetric for $E_\nu \geqslant 4\,\mathrm{GeV}$. The spectral index of the model is modified by $E^{+0.05}$ to match recent observations [128]. There is no dependence on the azimuthal angle assumed, neglecting possible but small geomagnetic effects.

The neutrino-nucleon interactions in the ice are simulated using the GENIE event generator [130]. The validity of GENIE extends to all nuclear targets and neutrino flavors, with energies from MeV to a few hundred GeV. The generator implements an interaction model which includes ad hoc parameters that can be tuned to match the data. The main emphasis of

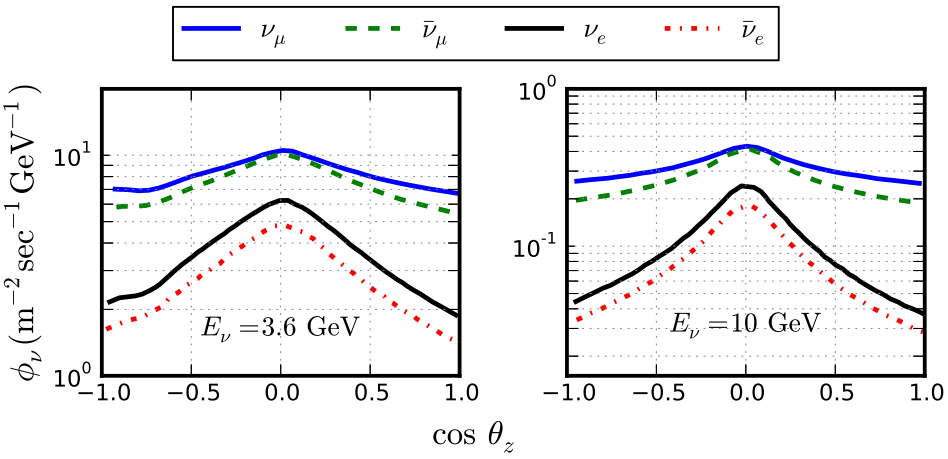

Figure 5.12: Zenith angle distribution of the predicted flux of atmospheric neutrinos at the South Pole for each neutrino flavor. Two neutrino energies are shown. Reproduced from [129].

the generator is on the transition region, where theoretical models are not well defined (see Section 2.3.2). Accelerator experiments like MINERvA, MINOS, and T2K, among others, have used GENIE to cross-check and validate their baseline simulation codes, and have found it to give consistent results (see Refs. [67,131,132]).

Atmospheric muon background

The atmospheric muons that reach the detector are obtained from the full simulation of cosmic ray interactions in the atmosphere and the subsequent particle shower. This is done using a modified version of the Cosmic Ray Simulations For Kascade package (CORSIKA) [133]. This software allows simulating air showers initiated by different cosmic ray primaries following the rules of distinct hadronic interaction models. The baseline simulation used in this analysis follows the composition and flux proposed by Hoerandel *et al.*, and the SIBYLL interaction model [134].

The CORSIKA tool tracks all of the particles during the shower evolution in the atmosphere. The implementation in IceCube, known as dCORSIKA[1], has been modified to use parameterizations of muon energy losses and discard particles that do not have enough energy to reach the depth of the detector. Once the muons are in the vicinity of IceCube they are propagated using a different set of tools.

Propagation of charged particles and photons

The passage of charged particles through matter is studied in detail in the next Chapter, and only the relevant details for simulation purposes are given here. The treatment of charged particles in the IceCube simulation is divided in two branches. Muons and tau leptons are dealt with individually by means of the Muon Monte Carlo (MMC) code presented in [135]. The MMC software implements a parameterization of the energy losses with the aim of speeding up the simulation. Since the muon tracks that interest the typical IceCube searches can be kilometers long, the approach is very well justified. In MMC the travel direction is

[1] http://dima.lbl.gov/~dima/work/CORSIKA/

kept fixed but the effects of multiple Coulomb scattering are included in the calculation of energy losses and the Cherenkov emission profile.

The rest of the charged particles, electrons and hadrons, are simulated using variations of a "cascade" object. The cascade templates come from parameterizations obtained using the Geant4 package [136], obtained by [137], based on previous work of [111] and [138]. While Geant4 implements a full simulation of the physical processes that take place during the transport of a particle, the spacing of the IceCube detector and the medium properties make most of the fine details not discernible. The result is that, to a good approximation, the energy losses of these particles can be modeled by a generic cascade object. The validity of the approximation breaks down for low energies (below 5 GeV) where the development of the cascade have larger fluctuations than those from the calculated templates [137].

Once the Cherenkov emission of muons and cascades has been calculated the photons are propagated through the ice. In order to determine which of them arrive at the DOM, and when they do so, each photon is propagated individually. The propagation takes into account the optical properties of the bulk ice to determine the photon's path. All photons emitted are tracked, keeping only those that arrive in the vicinity of a DOM. A more detailed description of the direct photon propagation simulation can be found in Appendix A of [124].

DOM simulation

The next step in the simulation chain is to reproduce the behavior of the DOM. The influence of the borehole ice is introduced here as a modification of the angular acceptance. The wavelength dependent response of the PMT is also included, which was obtained in laboratory measurements using single photons and very faint light sources [120]. Next, the behavior of the DOM electronics is recreated, yielding a digitized signal.

Noise due to electronics and other processes is included in this step. The injected rate of background photons, typically 500 Hz for IceCube DOMs and 650 Hz for DeepCore DOMs, is obtained individually for each sensor after it has been deployed and left to stabilize [120]. From this point on, the analysis of data and simulation is done using the same tools. The ones in charge of characterizing the signal are described in the following Chapter.

6 Reconstructing muon neutrinos in ice

This Chapter focuses on the reconstruction of the two observables upon which an oscillations measurement can be performed, namely the neutrino energy and the distance it traveled before detection. The first Section describes the physics of the passage of particles through matter, following closely the work of Kowalski, Wiebusch and Raedel [111, 137, 138]. It is followed by a study of the signature that these particles leave in the detector, and how this is used to reconstruct the kinematic variables of an event. The scope is limited to neutrinos with energies from a few to a few hundred GeV, with special emphasis on CC ν_μ interactions.

6.1 Charged particles in ice

When a charged particle traverses matter it interacts with the medium. As a result, a fraction of the particle's energy and its original direction are lost. If the particle happens to be traveling faster than the speed of light in the medium it emits Cherenkov radiation. This radiation accounts for only a small fraction of $\mathcal{O}(10^{-4})$ of the total energy losses, but is the one upon which IceCube DeepCore relies in order to detect neutrinos.

6.1.1 The Cherenkov effect in ice at the South Pole

For a material with refraction index n there is a velocity threshold above which a charged particle starts emitting coherent electromagnetic radiation, given by

$$\beta \geqslant \frac{1}{n}\,, \tag{6.1}$$

where β is the velocity in units of the speed of light in vacuum. The angle at which the light is emitted is given by

$$\cos\Theta_C = \cos\left(\frac{1}{\beta n}\right)^{-1}\,. \tag{6.2}$$

The light emission forms a cone due to constructive interference, as depicted in Fig. 6.1. For very relativistic particles ($\beta \simeq 1$), the angle of emission is independent of the particle's energy, and depends only on the refraction index of the medium.

The number of Cherenkov photons emitted per wavelength λ and unit track length x can be estimated using the Frank-Tamm formula [139] to be

$$\frac{d^2N}{dxd\lambda} = 2\pi\alpha\frac{1}{\lambda^2}\left(1-\frac{1}{(\beta n)^2}\right)\,. \tag{6.3}$$

Here α is the fine structure constant. In the range between [300-500] nm, where the IceCube DOMs are sensitive and the South Pole ice is transparent, and using $n = 1.35$, the integral of the formula yields an emission of about 270 photons per centimeter of track length.

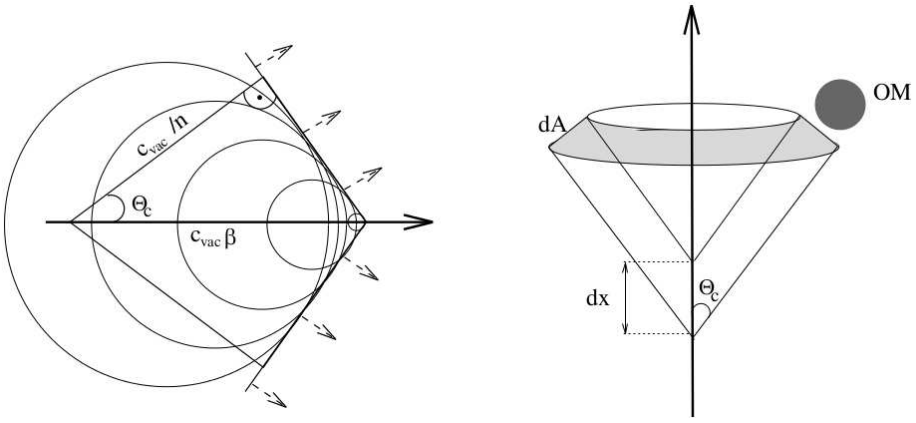

Figure 6.1: Geometry of the emission of Cherenkov light. The Huygens construction (left) is shown together with a sketch of light detection by a DOM (right). Taken from [111].

6.1.2 Muon propagation in the Antarctic ice

A muon traveling through a medium loses energy mainly via ionization, bremsstrahlung, photo-nuclear interactions and pair production. For a particular material the total energy loss can be expressed as a weighted sum of all individual contributions, resulting in an average energy loss

$$-\frac{dE}{dx} = a(E) + b(E)E\,. \tag{6.4}$$

Here the first term includes the energy losses due to ionization, while the second one sums up the radiative processes mentioned. The parameters $a(E)$ and $b(E)$ have only a weak dependence on energy, so approximating them as constant,

$$-\frac{dE}{dx} = a + b\,E\,. \tag{6.5}$$

From the previous equation it can be seen that there is a critical energy that separates the domains where ionization and radiative losses dominate, which can be estimated as $E_{\text{crit}} \equiv a/b$. Using typical values for ice, $a \simeq 0.259\,\text{GeV}\,\text{m}^{-1}$ and $b \simeq 0.363 \cdot 10^{-3}\,\text{m}^{-1}$ [138], results in a critical energy of about 700 GeV. The relevant muons for atmospheric neutrino oscillations are well below this threshold, so a further approximation can be made by setting $b = 0$. The energy loss is then constant, and by integrating Eq. 6.5 it is possible to relate the range of the muon R_μ and the initial energy E_0 by the simple expression

$$R_\mu = \frac{E_0}{a}\,. \tag{6.6}$$

This allows one to estimate the energy of the muon by reconstructing its range, something that in principle can be done for contained events in IceCube DeepCore.

A muon propagating through matter scatters with the charged particles of the medium. The cumulative effect of these scatterings can modify the averaged direction that the muon track follows. Simulation studies have quantified this effect using water as the propagation medium [140]. They looked at angular difference between the direction in which the muon was emitted and the position where the muon decayed after it scattered. They found that

for muons with energies 10 GeV the difference in angle can be as large as 4 degrees. This difference decreases for higher energies, to about 1 degree at $E_\mu = 20\,\text{GeV}$.

The continuous scattering also modifies the light emission profile of muons. The result is a subdominant contribution in directions surrounding the Cherenkov angle. The total light profile for muon neutrinos in ice is shown in Fig. 6.2, compared with that of cascades, which are presented next.

6.1.3 Electromagnetic and hadronic cascades

Electrons and photons

High energy electrons, or positrons, traveling through matter radiate photons through bremsstrahlung. Photons, in turn, produce electron-positron pairs when they interact with matter. These processes get repeated iteratively, producing an *electromagnetic cascade*. The cascading process stops when ionization becomes the dominant energy loss, which happens when all electrons reach a critical energy E_c.

The average distance over which an electron is reduced to $1/e$ of its energy is called the radiation length, X_0. In the simplest model it is assumed for every radiation length, an electron emits a photon, which generates an electron-positron pair. The next generation electrons share the energy lost by the parent equally. When E_c is reached all the particles deposit their energy at once. Under this assumption, a cascade has an elongation or depth X given by

$$X = X_0 \ln \frac{E}{E_c}\,, \tag{6.7}$$

where E is the energy of the electron that starts the process. Characteristic values in ice are $X_0 \sim 40\,\text{cm}$ and $E_c \sim 80\,\text{MeV}$.

The simple model has two properties that hold in full simulations,

(i) the longitudinal development of a cascade has a logarithmic dependence on energy, and

(ii) the number of electrons produced, and hence the total track length, is proportional to the energy of the initiating particle.

The result is that cascades will have elongations of a few meters at most, appearing almost point-like to a detector such as IceCube, and their brightness has a linear dependence on the energy of the particle that initiates the process, also referred to as the *cascade energy*.

The light profile of the cascade emission is shown in Fig. 6.2 together with the one of the muon. The photons are on average emitted in the forward direction, which gives rise to a peak at the Cherenkov angle in the light profile of cascades. About 30 % of the Cherenkov photons emitted stay within 3 degrees from the Cherenkov cone given by the cascade axis. For the muon track, close to 90 % of the photons are emitted within the same angle.

Hadrons

The final state of the neutrino-nucleon DIS always includes hadrons. High energy hadrons interact with the nuclei in matter leading to secondary hadrons and leptons in an iterative process which results in what is known as a *hadronic cascade*. As electrons and photons are created in the process, a substantial part of hadronic cascades is indeed electromagnetic.

The basic development of hadronic cascades in space is very similar to that of electromagnetic ones, but with important differences in energy losses, particle content, lateral spread

and fluctuations. Hadronic cascades contain particles heavier than electrons, that have a higher Cherenkov threshold. A fraction of them are slow neutrons, which do not produce any light. Neutral pions also produce no light, but they decay into photon pairs, which start their own electromagnetic cascades. Charged pions, on the other hand, can decay into muons and muon neutrinos; long-ranged particles that do not contribute to the cascading process. Finally, a non-negligible fraction of the energy is lost in the hadronic binding processes.

The result is a light yield smaller than the one obtained from an electromagnetic cascade of equal initial energy and with much larger event-by-event variation. The fraction F by which the number of photons emitted is smaller can be approximated by [141]

$$F = 1 - \left(\frac{E}{E_0}\right)^{-m}, \tag{6.8}$$

where E_0 and m are parameters of the model which depend on the material and the type of hadron involved. For ice, $m \simeq 0.16$ and $E_0 = 0.19\,\text{GeV}$ [138], resulting in an F between 0.6 and 0.8 for hadronic cascades between 10 GeV and 100 GeV. Using Eq. 6.8 it is possible to relate hadronic cascades to equivalent electromagnetic ones and have a unified scheme for estimating their energy.

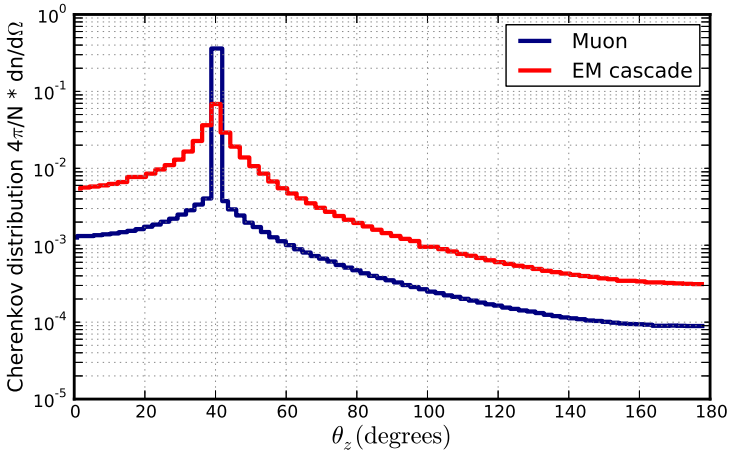

Figure 6.2: Normalized Cherenkov emission profile for 300 GeV muons (blue) and 100 GeV electromagnetic cascades (red). Reproduced from [111].

6.2 Signature of CC ν_μ events in IceCube

From the details gathered until this point it is possible to summarize the relevant physical characteristics of CC ν_μ interactions at the energies of interest:

- A muon track and a hadronic cascade are produced, as depicted in Fig. 6.3.
- The muon is minimally ionizing and with a range from a few to a few hundred meters ($E_\mu = [10, 100]\,\text{GeV}$), it can decay inside the detector's volume.
- The distribution of the energy taken by the muon and the hadrons, E_μ/E_had, depends on whether a neutrino or an antineutrino interacts.

- The cascade elongation is only logarithmically dependent on the energy, while the muon range has a linear dependence on it.
- Both objects emit light in following a profile that peaks at the Cherenkov angle. The emission outside this direction is much stronger for cascades.
- Both cascade and muon light emissions are proportional to the particle's energy.

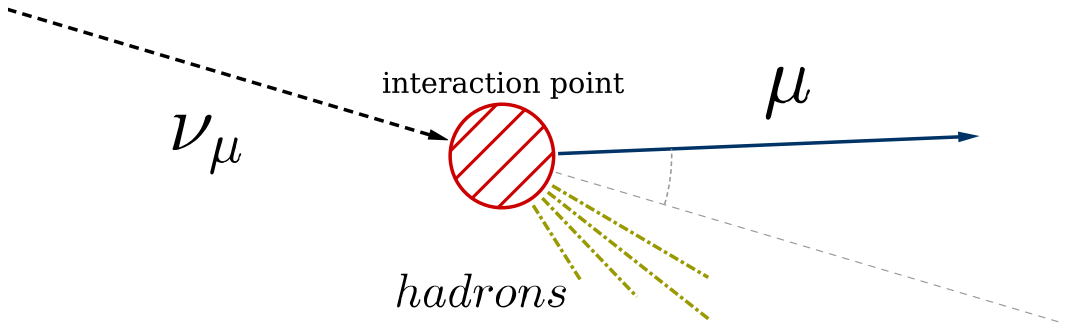

Figure 6.3: Sketch of a ν_μ CC interaction as seen by IceCube DeepCore.

Taking these points into account, we consider once again the specific case of IceCube DeepCore and the medium where it is located. Typical signal events will consist of muon tracks and cascades of energies around 15 GeV. For the tracks, this translates into a 60 m range, according to Eq. 6.6. While the details depend on the exact orientation, a muon of such energies can pass close to 6 DOMs and deposit its light in around twice that number. The number of DOMs that hold information from a cascade, on the other hand, depends heavily on its position in the detector. However, since most of the sensors with photons coming from a cascade will be on the closest string, it is usually not more than about 7 DOMs.

With so few positions in space holding information, any analysis strategy has to be robust against event-by-event variations. The typical events that IceCube searches for, of TeV energies and higher, leave photons in many more DOMs in the detector. The high energy and low energy data cannot be analyzed following the same steps. An event selection and reconstruction tools that expect a very faint signal are necessary. A way of using low energy faint signals, developed specifically for this analysis, is the focus of the rest of the Chapter.

6.2.1 Direct Cherenkov light in the DOMs

The average distance between strings DOMs inside the DeepCore fiducial volume is of 70 m, which is close to the typical effective scattering length of photons in the medium, of about 50 m [124]. It is likely that any photon they record has followed a path different from a straight line before its arrival. Despite this, there will be a fraction of photons which happen to travel (almost) undisturbed until they are detected. From here on we call these photons *direct*.

The scattering and absorption of the medium, which have been shown to have large variations (see Fig. 5.8), change the fraction of direct photons that can be expected from a given source. These medium properties, however, do not affect the time information that the direct photons carry. Therefore, an observable built as a function of the time of arrival of direct photons will only be dependent on the optical properties of the propagation medium by

threshold effects (e.g. modifying the absorption coefficient can reduce the number of direct photons expected so that events are missed). The analysis presented in this work is built around the idea of selecting these direct photons, and using an event only when enough of them are found[1].

Consider a Cherenkov emitter with infinite range crossing the DeepCore volume. The light wavefront expands in the shape of a cone, which eventually meets a string of DOMs. When the cone passes by a string it projects a conic section in space and time: a hyperbola. A sketch of this is shown in Fig. 6.4.

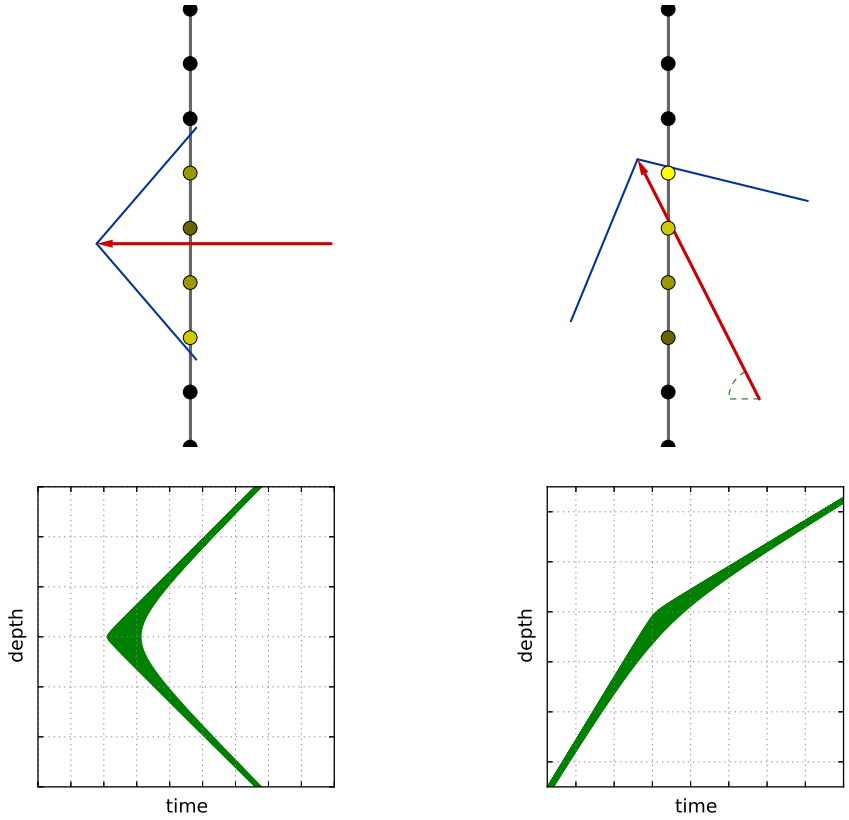

Figure 6.4: Formation of hyperbolic patterns. Top: diagrams depicting the differences in arrival time of photons to the DOMs as a function of the orientation of the Cherenkov emitter (red). Dark yellow means early signals, bright yellow means late. Bottom: hyperbolas formed by the intersection of Cherenkov light with the detector's strings for the two geometric configurations on top and a distance between $[0, 50]$ m between emitter and string.

Assuming that the string is perfectly vertical the configuration has rotational symmetry. It is then possible to remove one dimension from the problem and describe the situation in the plane perpendicular to the vector connecting the cone's axis and the string at the point where they are the closest. This point is referred to as the *point of closest approach* in short. Doing so allows uniquely defining the hyperbola by means of four quantities. A sketch that illustrates the definition of the quantities is shown in Fig. 6.5. The top view in panel (a) shows the point of closest approach, while the projection in the plane just described is contained in panel (b).

[1] In [142] the ANTARES Collaboration published the idea of using hyperbolic patterns.

The variables that define the hyperbola are listed below, together with an explanation of how they modify the projection:

- Distance between string and point of closest approach, d_c. It affects how sharp the change of direction is for the two arms of the hyperbola, where closer means sharper.
- Depth of the point of closest approach (z-axis), z_c. Transports the hyperbola up or down in the plot.
- Time of closest approach, t_c. Transports the hyperbola left or right in the plot.
- Angle between the cone's axis and the string, which is part of the direction vector $\vec{p}$. Changes the orientation of the arms of the hyperbola, as shown in Fig. 6.4.

Since the strings are aligned vertically, the angle between a string and the cone's axis corresponds to the zenith angle. In this work we use the physical strings as our axis, as the zenith angle is the quantity of interest. It is, however, possible to define an arbitrary plane as long as there are detectors aligned that fulfill the rotational symmetry and follow the same exercise.

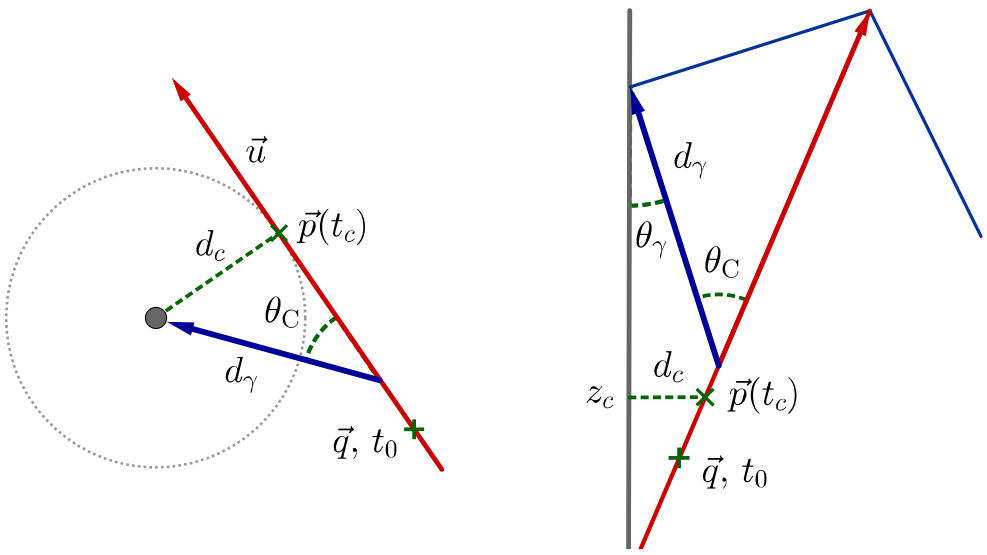

(a) Top projection **(b)** Side projection

Figure 6.5: Top and side projections of a Cherenkov emitter (red) passing by a string (gray). The variables that fully describe the emitter are shown. The vector d_γ is the distance traveled by the photons, and only its projection can be given in this sketches.

For the case of a particle with finite range the only changes are that the cone has a beginning and an end. After the particle either interacts or decays, the wavefront is not a complete cone any longer. The projected hyperbola may be missing a region, but the idea still holds.

From the light profile emission of cascades in Fig. 6.2 it can be expected that the arrival of photons at a string will also describe a hyperbolic shape, but not as well defined as for a track. Depending on the light emission of the cascade, it can almost appear to the detector as an isotropic source of light. The pattern resulting from such a point source is similar to the one given by a horizontal muon passing rather far away (see Fig. 6.4). Identifying these patterns is a way of differentiating events with a clear muon from events dominated by a cascade.

The outcome is that the signatures of both muons and cascades describe a hyperbola. Considering the case of IceCube DeepCore requires that we take into account the finite time resolution, jitter and noise from the detector side, and the absorption and scattering from the medium side. The items related to the detector are random, and add a variation that can be averaged out with enough photons. However, absorption will reduce the information available, while scattering will modify the time of arrival of photons and create fake direct patterns.

6.2.2 Identifying the direct photons of a neutrino event

The pattern that direct photons create is known, thus it is possible to search for them based only on their time of arrival (TOA). This has to be done independently at each string, and is implemented on all the pulses detected by an algorithm that goes through the following steps:

1. Look for a string that has at least 3 DOMs with pulses, the minimum requirement to identify a hyperbola.

2. Characterize the signal of each DOM with the arrival time of the earliest pulse recorded, and integrate the charge of all the pulses recorded by the DOM.

3. Restrict the search to DOMs inside a time window of $[-1, +2]\,\mu$s around the median TOA for the string under consideration. The time window is approximately the one required for a particle to travel the elongation of a string.

4. Search for the DOM which has the largest integrated charge. This is an estimator of the point of closest approach and it is also the first DOM temporarily accepted; we call it DOM_0. Use this point as a reference to scan the string up and down searching for more DOMs.

5. From the starting point t_0, given by the earliest pulse at DOM_0, calculate a time window for testing the TOA of the pulse in the DOM above, DOM_{+1}. The time window is symmetric, and given by the time that a photon takes to travel between the two DOMs. It can be expressed as

$$\left[t_0 - \frac{d_{0,+1}}{c_{\mathrm{ice}}} - t_{\mathrm{delay}}, t_0 + \frac{d_{0,+1}}{c_{\mathrm{ice}}} + t_{\mathrm{delay}} \right] . \tag{6.9}$$

   Here $d_{0,+1}$ stands for the absolute distance between the two DOMs considered, 0 and +1, c_{ice} is the speed of light in ice, and the parameter t_{delay} determines how strict the selection is with regard to scattering effects. A value of 20 ns for t_{delay} is used as a baseline. This step is repeated until one DOM is accepted. If none are, steps 6-8 are skipped.

6. Include the new DOM selected by the previous step in the search by defining a new time window for testing DOM_{+2}. While the lower limit is defined by the same conditions, the upper limit changes to reflect the newly acquired information. The time window is now given by

$$\left[t_1 - \frac{d_{1,+2}}{c_{\mathrm{ice}}} - t_{\mathrm{delay}}, t_1 + \frac{d_{1,+2}}{v_{\mathrm{eff}}} + t_{\mathrm{delay}} \right] , \tag{6.10}$$

   where v_{eff} defines an effective velocity for a photon that travels in between the two DOMs in question. This velocity is calculated using the last three DOMs that have

been selected; the resulting possibilities are shown in Fig. 6.6. The algorithm calculates all three effective velocities and takes the slowest one, allowing the largest time window possible.

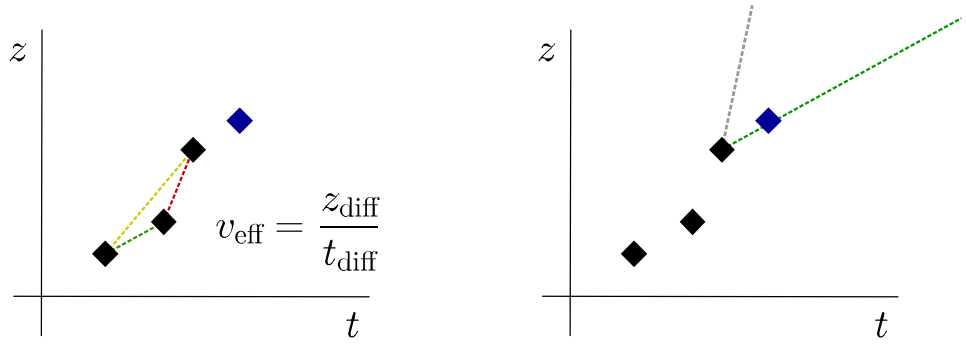

(a) Possible v_{eff} **(b)** Slowest v_{eff}

Figure 6.6: Criteria for selecting direct pulses. Markers represent pulses. Black pulses have been selected. The blue pulse is the one being tested. In (a) the three possible effective velocities given the pulses that have been selected are shown. In (b) the smallest effective velocity is applied (green line). The gray line is the earliest time of arrival allowed, as given by Eq. 6.10. In this example, the blue pulse would be taken.

7. Every time that a new DOM_n is taken, check again if all previous DOMs still match the hyperbolic shape. Using DOM_n and DOM_0 calculate an expected time of arrival for the signal of every intermediate DOM and allow a delay of $t_{\text{delay}}/2$. If a DOM falls outside the window, remove it from the selection. Figure 6.7 sketches a situation in which, depending on the t_{delay} used, the marked hit could be removed. This step allows for early photons to be used to remove scattered photons that might have been selected.

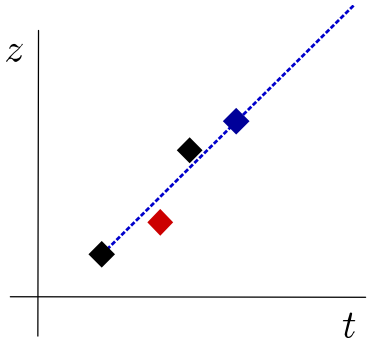

Figure 6.7: The latest pulse accepted (blue) is used to test if all previously ones selected still match the hypothesis. The pulse marked in red is discarded.

8. The search continues until either the string ends, or 8 consecutive DOMs are found that either have no signal or are rejected.

9. Steps 5 through 8 are repeated but now for DOMs below DOM_0.

10. If three or more DOMs are found to match the conditions in one string, they are identified as containing direct pulses. In any other case, all of the pulses from the string are discarded.

11. Steps 1 through 10 are repeated until all strings have been scanned.

Figure 6.8 shows, for a simulated event, the steps that the algorithm takes in order to identify the direct photons. The dashed line corresponds to the expectation from pure Cherenkov light. Note that many pulses are removed, but the remaining ones follow the hyperbolic pattern.

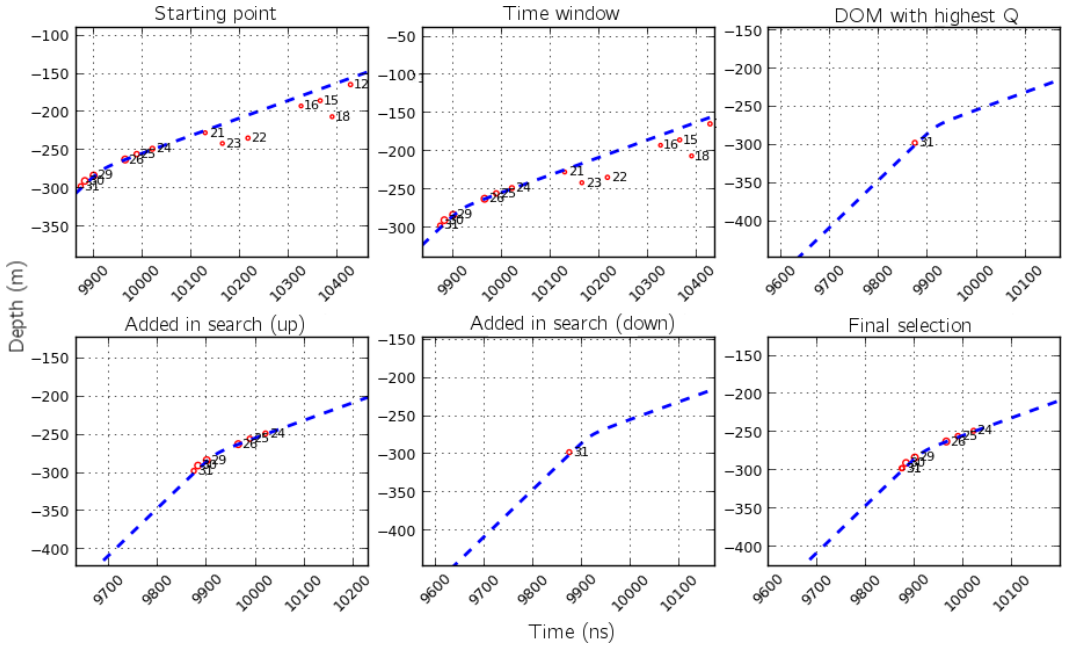

Figure 6.8: Step-wise demonstration of the selection of direct pulses for one string of a simulated event. The expected alignment of the pulses is given by the blue dashed line. The number corresponds to the DOM position on the string, where 60 is the bottom-most one.

The signals in the DOMs selected are assumed to be direct photons, and are labeled as such for the rest of this work. The direct photons are used to judge the quality of the event, as it will be seen in the next Chapter. Since the scattering is minimal, they are also used to reconstruct the direction and position of muon tracks.

6.3 Directional reconstruction

The fitting procedures described correspond to the ones introduced first by J. Brunner *et al.* in [142] (ANTARES). We use the same terminology and notation as in the original paper, with minor modifications. The diagram of Fig. 6.5 shows the variables described below.

6.3.1 Track-like sources

Starting from the assumption that a particle travels at a known constant speed and it does so in a straight path, there are six variables that completely define its kinematical behavior: a point in space time along the particle's trajectory, and two angles which determine its direction. While the two angles are unique, the point along the trajectory of the particle contains a redundant variable, as any point can be chosen. All these points that form part of the track's trajectory can be parameterized as

$$\vec{p}(t) = \vec{q} + c\,(t - t_0)\,\vec{u}\,, \tag{6.11}$$

where $\vec{q}$ is the point crossed at t_0 and $\vec{u}$ is the direction vector, given by

$$\vec{u} = \{\cos\vartheta\cos\phi,\ \cos\vartheta\sin\phi,\ \sin\vartheta\}\,. \tag{6.12}$$

Note that in Eq. 6.12 the zenith angle appears in $\vartheta = \theta_z - \pi/2$.

Approximating the strings as vertical lines parallel the z-axis at positions $(L_x,\ L_y)$, the coordinates of the point of closest approach are given by this set of formulas,

$$z_c = \frac{q_z - u_z\,(\vec{q}\cdot\vec{u}) + u_z\,(L_x u_x + L_y u_y)}{1-u_z^2}\,, \tag{6.13}$$

$$t_c = t_0 + \frac{1}{c}\,(L_x u_x + L_y u_y + q_z u_z - \vec{q}\cdot\vec{u})\ , \tag{6.14}$$

$$d_c = \sqrt{(p_x(t_c) - L_x)^2 + (p_y(t_c) - L_y)^2}\,. \tag{6.15}$$

Here the track has been conveniently parameterized in terms of the quantities which define the hyperbola of Fig. 6.5: z_c, t_c, d_c and u_z.

In the case of dealing with a single string there is no preferred direction in the $x-y$ plane, and the symmetry makes the quantities defined useful, as they fully define the particle track. Dealing with one string only allows for the freedom to redefine the x and y coordinates of its position. Setting the $x-y$ position of the string to $(0,0)$ $(L_x = 0, L_y = 0)$ simplifies the equations, giving

$$z_c = \frac{q_z - u_z\,(\vec{q}\cdot\vec{u})}{1-u_z^2}\,, \tag{6.16}$$

$$t_c = t_0 + \frac{1}{c}\,(q_z u_z - \vec{q}\cdot\vec{u})\ , \tag{6.17}$$

$$d_c = \sqrt{p_x^2 + p_y^2}\,. \tag{6.18}$$

Using these variables, the time of arrival of a photon t_γ at a point z along the string, which experiences a refraction index n, can be calculated by

$$t_\gamma(z) = (t_c - t_0) + \frac{1}{c}\left((z-z_c)\,u_z + \frac{n^2-1}{n} d_\gamma(z)\right)\ , \tag{6.19}$$

$$d_\gamma(z) = \frac{n}{\sqrt{n^2-1}}\sqrt{d_c^2 + (z-z_c)^2\,(1-u_z^2)}\,, \tag{6.20}$$

$$\cos\theta_\gamma(z) = \left(1-u_z^2\right)^2 \frac{z-z_c}{d_\gamma(z)} + \frac{u_z}{n}\,. \tag{6.21}$$

The variables d_γ and θ_γ are the distance traveled by the photon and the angle of arrival with respect to the string's axis, as shown in Fig. 6.5. The equations are valid if there are pulses in multiple strings as well. This requires (i) that the differences in string positions are taken into account, and (ii) an extra variable to fully define the problem, as there is no rotational symmetry any longer.

6.3.2 Point-like sources

The emission of an isotropic point-like source, which produces a single light flash at a given moment, is also described by a hyperbola. This approximation can be used to model cas-

cades because their elongation is much shorter than the spacing between DOMs, even in the DeepCore volume.

Unlike for the track case, a point-like isotropic emitter does not have a travel direction, thus the problem has one degree of freedom less. It is convenient to modify the point of closest approach to represent the interaction vertex of a cascade, then $z_c = q_z$, $t_c = t_0$, and

$$d_c = \sqrt{(q_x - L_x)^2 + (q_y - L_y)^2}\,. \tag{6.22}$$

Considering a single string again, and assuming that it is located at $(0, 0)$, then $d_c = \sqrt{q_x^2 + q_y^2}$. The photon arrival time t_γ is now given by a different set of equations:

$$t_\gamma(z) = t_0 + \frac{n}{c} d_\gamma\,, \tag{6.23}$$

$$d_\gamma(z) = \sqrt{d_c^2 + (z - q_z)^2}\,, \tag{6.24}$$

$$\cos\varphi_\gamma(z) = \frac{z - q_z}{d_\gamma}\,. \tag{6.25}$$

Again, multiple strings can be used, as long as the simplification of putting them at (0,0) is removed.

6.3.3 Fitting procedure

In order to fit the observed time of arrival with the expectation we use a χ^2 with an additional term. The error involved in the observation is estimated by the readout binsize of 3 ns. The errors are expected to follow a normal distribution, which justifies the method selected.

The timing information is complemented by using the total charge observed at each DOM. For a medium with uniform optical properties the largest signal is expected from the photons that travel the shortest distances to the detection unit. This is implemented by including a term that penalizes trajectories in which this does not hold. For this purpose the angular acceptance of the DOM needs to be included, which is modeled as $(\cos\theta_\gamma + 1)/2$, where θ_γ is the polar angle defined by the axis of the DOM. The measured charge q_i in the i-th DOM is corrected as

$$q_i' = \frac{2q_i}{\cos\varphi_\gamma + 1}\,. \tag{6.26}$$

There is a minimum distance which any photon travels $d_{\min}$, given by the DOM size itself. Enforcing it avoids the tendency to systematically put the track fit close to a detector string. This is done by using a modified photon travel distance D, which is defined as

$$D(d_\gamma) \equiv \sqrt{d_{\min}^2 + d_\gamma^2}\,. \tag{6.27}$$

The modified χ^2 is then

$$\chi^2_{\text{mod}} = \sum_{i=1} \left[\frac{(t_{\gamma,\text{exp}}(z_i) - t_{\gamma,\text{obs}}(z_i))^2}{\sigma_\gamma^2} + \frac{q'(z_i)\, D(d_\gamma)}{\bar{q}\, d_0} \right]. \tag{6.28}$$

Here the expected and observed time of arrivals t_γ are compared, in units of the time resolution σ_γ^2. The integrated and corrected charge q_i' multiplied by the travel distance D is weighted by the mean charge $\bar{q}$ multiplied by d_0. This quantity, d_0, enters to balance the weight between the two terms, and can be interpreted as the typical distance at which the

detector expects to see a signal of one photoelectron. The values used for this work are $\sigma_\gamma = 3\,\text{ns}$, taken from PMT calibration studies [120], and $d_0 = 10\,\text{m}$, taken from simulation.

6.3.4 Performance of the zenith angle fit

The resolution of the zenith angle fit was tested using simulated muon neutrino events starting inside the DeepCore volume. The results can be seen in Fig. 6.9. The sample follows an $E^{-2.5}$ spectrum between 4 GeV and 80 GeV, with a mean energy of of $E_\nu = 15\,\text{GeV}$, and it was divided according to the neutrino arrival direction. The results are shown separately for events reconstructed using a single string and those that used multiple strings.

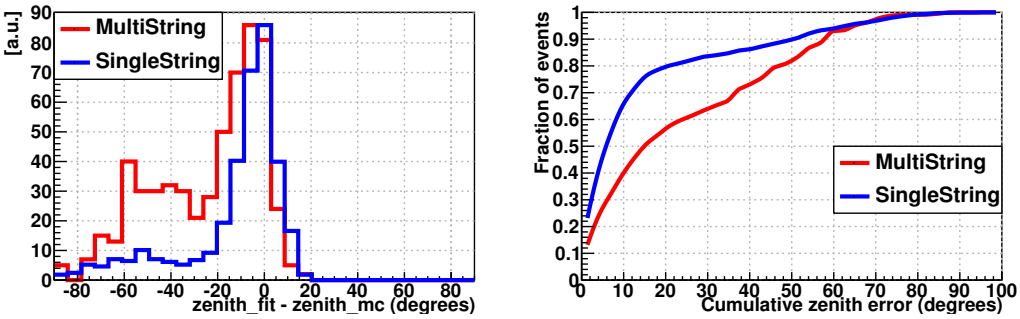

(a) Up-going events

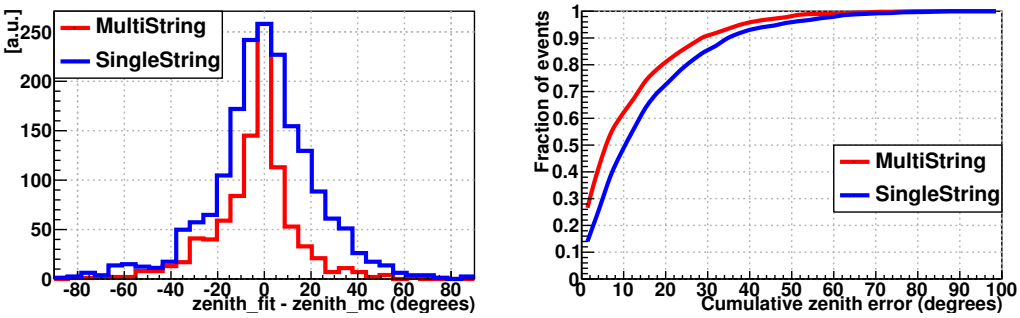

(b) Events coming from the horizon

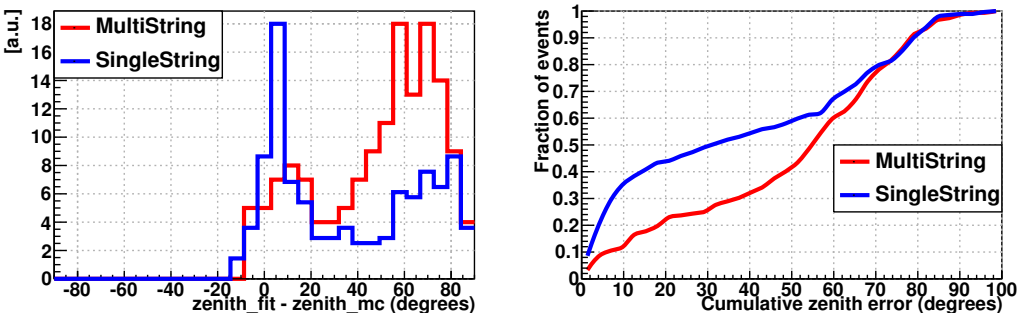

(c) Down-going events

Figure 6.9: Zenith angle resolution (left) and cumulative distribution of the sample as a function of the zenith angle resolution (right). Results for single- and multi-string reconstructions are shown. The sample is divided according to the neutrino direction.

Figure 6.9a corresponds to up-going events, with $\cos\theta_z < -0.9$. The error on the zenith angle is centered on zero, with long tails created by bad misreconstructions. The distribution has an RMS of 20 degrees, dominated by misreconstruced events. Depending on the reconstructing method (single- or multi-string), half of the sample has an error smaller than 6 or 15 degrees. For very vertical events of Fig. 6.9a fitting with only one string gives the best results; multiple strings introduce a bias on the fit.

The events coming from the horizon, $\cos\theta_z$ between $[-0.9, 0.9]$ show slightly different results, as it can be seen in Fig. 6.9b. The method with multiple strings performs better, although the difference is not very large. Both have an RMS close to 25 degrees, again dominated by misreconstructions. The half-sample error is close to 6 and 10 degrees for multi- and single-string fits, respectively.

Muons traveling downwards in the detector are not well reconstructed by the direct pulses method, as can be seen in the results from Fig. 6.9c. The Figure contains muons with a $\cos\theta_z > 0.9$. The reconstruction is not accurate because it assumes that the photons given to it are direct, while down-going muons emit light that can only arrive at a DOM after it has scattered. The patterns from these events are distorted enough so that they can fake the hyperbola hypothesis for another direction. The error on the direction of these events is too large for them to be included in the final sample. They are naturally removed by the identification of direct photons, but the ones which can fake the pattern searched for have to be removed during the selection by means of other tools.

This sample aims to show the benefits and the failures of the reconstruction, thus no selection was applied to the events evaluated. The zenith angle resolution of the final sample is much better, and is shown in the next Chapter, Fig. 7.12. At the final step, the reconstruction returns an error smaller than 10 degrees.

6.4 Neutrino energy estimation

The reconstruction of the neutrino energy follows the strategy presented in [143]. It assumes that at the interaction point of every event a muon track and a hadronic cascade are created. A sketch of this is shown in Fig 6.3. The two components are reconstructed individually, with an intermediate step to avoid double counting of pulses. In order to do so, the track has to be considered first.

6.4.1 Muon track energy

The energy of a muon track can be estimated from its length and/or the stochastic losses that it suffers along its path. At the energies on which we focus in this study the stochastic losses are almost negligible, leaving the range of the particle as the main observable.

The determination of the range of a muon track is done by searching for the most likely position where such track could have started and ended in order to explain the light pattern that the detector observes. The track position and direction are taken as given, and the reconstruction focuses on moving the two points mentioned along this unique axis. The vertex and decay point of the muon are fitted independently using different hypotheses.

Interaction vertex

All neutrino interactions have a cascade at their vertex. Any cascade above the Cherenkov threshold will produce an equal or larger amount of light than a muon per unit length along

the travel direction. A way to find the vertex of an event is to look for the first point along the track trajectory where a cascade can be placed.

This idea is implemented in an algorithm that attempts to put cascades all along the track, with a separation of 15 m between them. The charge expected at the DOMs in the neighborhood is obtained from tabulated simulation which includes the ice description. The procedure searches for the most likely sequence of cascades, and keeps the first one found as the best estimate of the event vertex.

Point of muon decay

The cascade develops fully in a distance of a few meters. After that, all light that can be detected comes from the muon track. The emission follows the sharp profile shown previously in Fig 6.2. If the muon decays inside the detector, its range can be used to determine the initial energy that it carried (Eq. 6.6). If the muon leaves the detector, the same Equation can be used too place a lower limit on the muon energy.

The first guess for the position where the muon decays is obtained by projecting the DOMs onto the track direction using the Cherenkov angle. The last point where a projection is found is used. This point is given as a seed to a more sophisticated method that includes the expected pulses from a muon track, as described in [144].

The probabilities for observing and not observing a signal given that there was a track present are calculated and combined in the likelihood ratio

$$\mathrm{LLHR} = \ln \frac{P(\mathrm{noHit}|\mathrm{Track})}{P(\mathrm{noHit}|\mathrm{noTrack})} \,. \tag{6.29}$$

Here $P(\mathrm{noHit}|\mathrm{Track})$ is the probability for not observing the light from the track, and $P(\mathrm{noHit}|\mathrm{noTrack})$ is the probability of not detecting photons given that the track decayed at an earlier point. Both situations are exemplified in Fig. 6.10. The ratio in Eq. 6.29 is minimized to identify the most likely decay point of the muon track being considered.

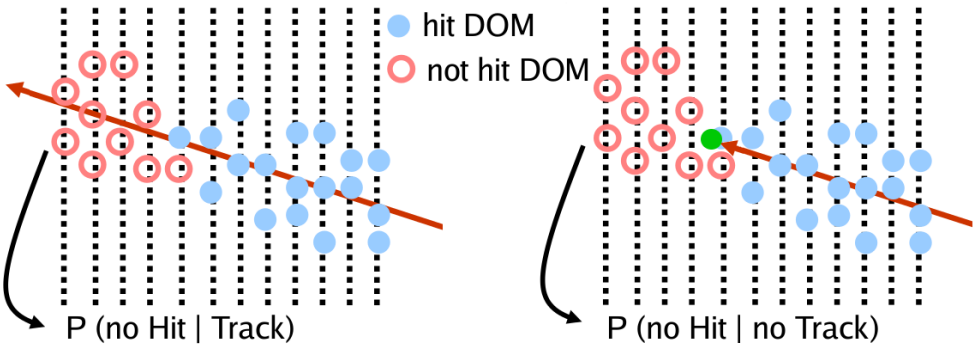

Figure 6.10: Sketch of how the probabilities to determine the position where the muon decays are calculated. The point of muon decay is marked in green (right-hand figure).

The range of the muon is calculated from the separation between the interaction vertex and the most likely decay point. By means of Eq. 6.6 the range can be converted into the initial muon energy, solving part of the problem. The next step is to estimate the cascade energy, but before doing so, the light contribution from the track has to be disentangled from the contribution of the cascade.

Separating the light contribution of tracks and cascades

Both the cascade and the muon track contribute to the light detected in the first few meters after a CC ν_μ interaction. Even in the situation where the cascade is much brighter, it is possible that the presence of a track introduces a bias in the cascade energy reconstruction, which expects a single cascade. In order to avoid this, the light contribution of the muon track is subtracted before such a reconstruction is performed. The procedure, described below, is sketched in Fig. 6.11.

Since the muon trajectory has been fully determined, it is possible to estimate the number of photons that are expected from it in a given DOM. According to [145], a good approximation can be obtained by using a simplified formula that includes the averaged effects of the geometric scattering length λ_s and absorption length λ_a. The formula is written in terms of the effective scattering length $\lambda_e = \lambda_s/(1 - \langle\cos\theta_s\rangle)$, which depends on the mean scattering angle θ_s. The expected number of photons is then given by [145, p. 6]

$$\mu(d) = l_0 A \frac{1}{2\pi \sin\theta_c} e^{-d/\lambda_p} \frac{1}{\sqrt{\lambda_\mu d}\tanh\sqrt{d/\lambda_\mu}}\,, \quad \text{where} \tag{6.30}$$

$$\sqrt{\lambda_\mu} = \frac{\lambda_e}{\sin\theta_c}\sqrt{\frac{2}{\pi\lambda_p}}. \tag{6.31}$$

Here l_0 is the average number of photons that a muon emits per unit length of its track, A is the DOM cross-section, θ_c is the Cherenkov angle in ice, and $\lambda_p = \sqrt{\lambda_a\lambda_e/3}$.

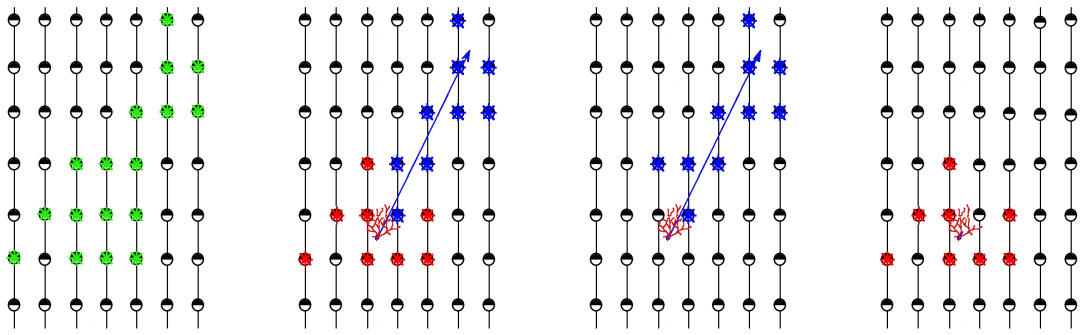

(a) Observation **(b)** Reconstruction **(c)** Muon light **(d)** Cascade light

Figure 6.11: Steps taken in order to separate the Cherenkov light emitted from the hadronic cascade at the vertex point from that of the muon. Taken from [143].

The resulting estimate is used to separate the light contribution of the muon from the one of the hadronic cascade in a DOM-by-DOM basis. In general, the photons from the track should arrive first, as they travel less or equal distance as those coming from the cascade. The number of photons given by Eq. 6.30 is subtracted from the sequence of pulses which could have been emitted from the track, starting from the earliest one. The light pattern that remains is the one used to estimate the energy of the cascade at the vertex.

6.4.2 Hadronic cascade energy

The hadronic cascade energy is estimated by varying its brightness, while the position and direction are kept fixed. For the position, the same vertex estimate found for the track is

used. The direction for the cascade is taken to be the same as that of the reconstructed track. Even though in reality the angles cannot be the same, the approximation is accurate.

The charge recorded by a DOM has a linear dependence on the number of photons that arrive to it, given that it does not reach saturation. The response of the DOMs can be characterized by an overconstrained system of linear equations,

$$Q_i = B_i \, E_{\mathrm{EM}}, \tag{6.32}$$

where Q_i is the observed charge (PEs) in the i-th DOM and B_i is the predicted photon distribution from an electromagnetic cascade of energy E_{EM}. The most likely value for E_{EM} is obtained by maximizing a Poisson likelihood which also includes noise terms[1]. The cascade parameterized is an electromagnetic one, which means that the result needs to be corrected (see Sec. 6.1.3). An empirical function relating the true and reconstructed energy is used, which on average is equal to the fit energy multiplied by a factor 1.4.

6.4.3 Performance of the full energy estimator

The performance of the full energy estimator was tested in the same sample used for the zenith angle reconstruction. The results are divided according to arrival direction, energy range and event type. The direction and position, required to start the algorithm, are taken from a reconstruction different to the one finally used in the analysis, with poorer resolution. The findings are nevertheless relevant, and correctly portray the reach of the method; the results obtained for this analysis are given in Section 7.2.

The results show that the energy reconstruction underestimates the total neutrino energy, with the exception of horizontal muon tracks of very low energies. There are ongoing investigations inside the IceCube Collaboration trying to determine the cause of this, which seems to be related to the sparseness of the detector. The reconstructions tend to systematically pull the event vertex close to the string with most photons. This allows the fits to explain the light detected with a dimmer cascade, lower energy cascade, and shortens the muon range. Events with cascades are affected the most, as it can be seen from Fig. 6.12. At the time that this analysis was developed, there was still no solution to this issue. The reconstruction is applied to data and simulation, so even though it underestimates the neutrino energy, the resolution that it gives is sufficient to separate a neutrino sample according to its energy.

The results for the sample containing muons that come from the horizon are shown in Figures 6.12a and 6.12b. At low energies, below 20 GeV, the reconstructed total energy is accurate within 50 % of the true neutrino energy. This is the worst possible sample, given that the events can start or end in regions where the instrumentation is too sparse. For energies higher than 30 GeV the situation improves. Muons can now reach ranges comparable to inter-string distances, resulting in an energy resolution of 30 %.

Muons traveling in a direction close to vertical can reach more DOMs than if they were to travel horizontally, and this translates into a better energy resolution. Figures 6.12c and 6.12d show the results for a nearly vertical sample, again divided in low and high energy events. Because of the orientation, the energy resolution improves by a factor 0.2, to a value of 40 % for events below 20 GeV. For higher energies, on the other hand, the orientation of the muon track does not play a role any longer. The results obtained for vertical and horizontal events are rather similar, as it can be seen from comparing figures 6.12b and 6.12d.

[1] A more detailed explanation of the idea can be found in [145]. Internal notes refer to this reconstruction under the name of "Monopod".

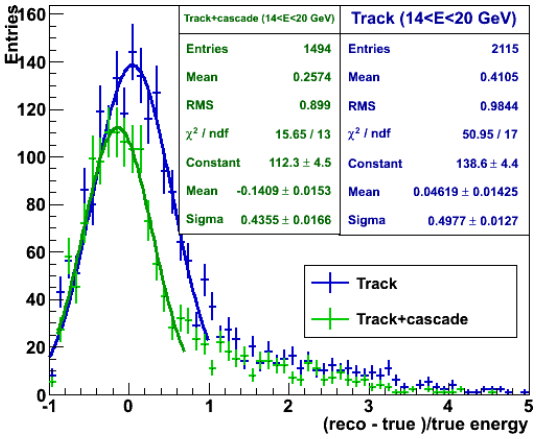

(a) $14 < E_\nu < 20$ GeV

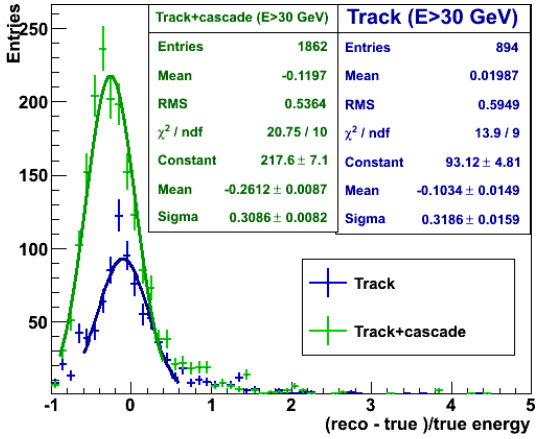

(b) $30 < E_\nu < 80$ GeV.

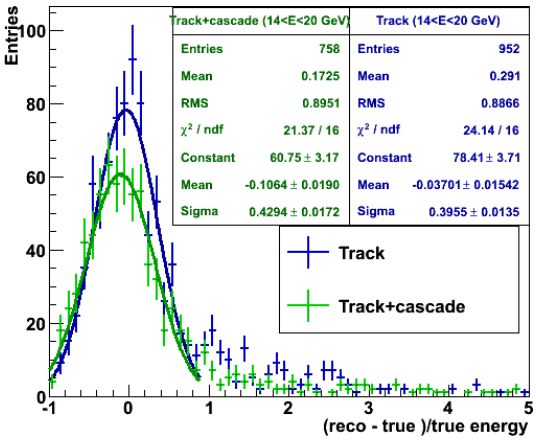

(c) $14 < E_\nu < 20$ GeV

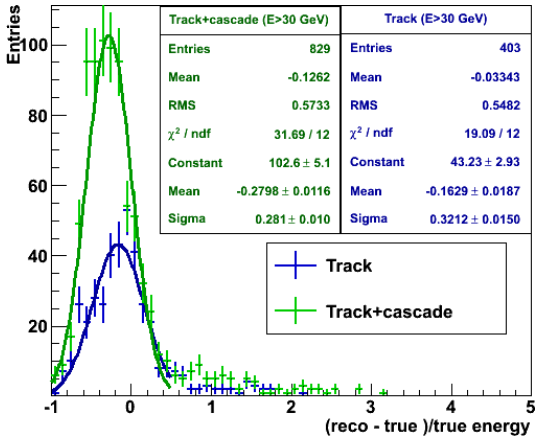

(d) $30 < E_\nu < 80$ GeV.

Figure 6.12: Energy resolution for test samples of up-going events (bottom) and events coming from the horizon (top). The resolutions are shown for a sample composed only by tracks, and for one which includes a cascade at the vertex. The figures are divided in two energy bands. Taken from [143].

Energy distribution between track and cascade

The full energy estimation method described gives a reasonable result, which can be accurate to around 30 % for a sample of atmospheric neutrinos. The individual estimation of the cascade and muon energies, on the other hand, have errors which are slightly larger than this factor, but partially cancel each other. The underlying problem is that the combination of the method described and the detector's characteristics do not allow to correctly separate the light contribution from the cascade and the track.

The light patterns that a track and a cascade produce close to the vertex point are typically degenerated, and reconstructing the energy in steps is not the best way to approach it. This degeneracy limits the possibilities for correctly reconstructing how the energy is distributed between muons and hadrons, and thus the y variable of the interaction. One of the oscillation

studies discussed in Sec. 5.3.3 required to have a handle on the y variable in order to separate neutrinos from antineutrinos, which does not seem plausible using this reconstruction method.

The methods presented for selecting neutrino events and reconstructing their kinematical variables are exploited in the following chapters with the goal of measuring muon neutrino disappearance. The results that they yield are the best ones among the available reconstructions in the Collaboration, and are accurate enough for the study at hand. But, even if from here on we discuss them almost exclusively in the context of the analysis of $\overline{\nu}_\mu$ disappearance, the ideas around which they are built are relevant for the rest of the oscillation analyses presented in Chapter 5, and any other study that aims to use GeV neutrinos and does not require an azimuthal angle.

7 Data analysis for $\nu_\mu + \bar{\nu}_\mu$ disappearance

This Chapter contains a detailed explanation of the steps taken in order to measure the effects of muon neutrino disappearance using IceCube DeepCore data. The description starts with the selection of the neutrino sample, which should contain events that leave a strong signature in the detector and a low level of atmospheric muon background. The fitting procedure as a function of the oscillation parameters comes next. The overall strategy and the steps introduced to deal with systematic uncertainties are also explained.

7.1 Data selection

The event selection seeks to maximize the sensitivity of the detector to the effects of muon neutrino disappearance. Optimizing the event selection, however, is technically challenging, and an approximate quantity is used instead of a full analysis, defined as

$$S = \frac{N_{\mu,\text{disappeared}}}{\sqrt{B}}. \tag{7.1}$$

Here S is the approximate sensitivity which we would like to maximize, $N_{\mu,\text{disappeared}}$ is the number of muon neutrino events that seem to disappear due to oscillations as given by the best known oscillation parameters, the signal of the analysis, and B is the sum of all the events recorded by the detector. This quantity does not take into account the fact that the signal is located at a particular values of energy and zenith angle, but since the event selection does not depend explicitly on these values, it is still useful.

The selection of events is presented as a three-step process, which describes

(i) the data taking and basic processing,

(ii) the strategies implemented to reject background, and

(iii) the variables related to event and reconstruction quality.

The steps are performed by discarding or cutting away regions of one-dimensional variables defined to deal with specific characteristics of the problem at hand. Possible correlations between them are not considered.

The selection of the cut values is done keeping in mind that the events that contribute to $N_{\mu,\text{disappeared}}$ in Eq. 7.1 are ν_μ with the following characteristics:

- $E_\nu \leqslant 100\,\text{GeV}$, as oscillation effects are stronger for them.
- The neutrino interacts via charged current (CC) inside the instrumented volume of DeepCore.
- A muon is found in the final state, with a range $R_\mu \gtrsim 25\,\text{m}$ ($E_\mu \gtrsim 5\,\text{GeV}$).

There are two sources of background for the analysis: atmospheric muons and neutrino interactions different from CC ν_μ. A large part of the selection consists in removing the

atmospheric muon component. The contribution from neutral current interactions and other neutrino flavors is expected to be suppressed by the cross-sections [30] and the flux itself [112], and is only explicitly removed in the final selection steps.

In the presentation of the selection procedure the different contributions to the data, as obtained from simulation, are shown. The atmospheric neutrino component includes the effects of oscillations, taking the parameters shown in Table 4.1. Since the contribution of atmospheric neutrinos at trigger level is orders of magnitude smaller than that of atmospheric muons, the atmospheric neutrino histograms are scaled up in all of the figures. The muon neutrinos that disappear, $N_{\mu,\text{disappeared}}$, are also quantified throughout the steps, and are labeled as "signal" in the figures.

Every figure shown is accompanied by a ratio of the data to the simulation, where the appropriate weights for the simulation have been used. In the best situation, the ratio should be flat and very close to one. However, as we will see throughout this Section, only the first condition generally holds. The reason for this is that all the figures are shown at a step where atmospheric muons dominate the sample, and the description of the atmospheric muon spectrum at the detector is rather uncertain. This will be considered when the data are fit to oscillations, while for now a variable is considered understood if the ratio of data to simulation is nearly flat.

The procedure was tested and the cut values were fixed using a partial data sample, which corresponds to about 30 days of detector livetime. This is about 10 % of the sample used to obtain the final result. This is standard IceCube policy to avoid introducing a bias in the selection. Each of the figures displayed in the following sections includes a comparison between the expectation and the data from this period. The whole sample was analyzed only after the study was carefully reviewed by the IceCube Collaboration.

7.1.1 Data taking and basic processing

The data taking starts with the trigger and in-situ filter, whose settings are fixed by the IceCube Collaboration. The data are further reduced by removing events which are likely to be noise or do not have enough information to be reconstructed. As the signal is expected at neutrino energies below 100 GeV, the dedicated DeepCore data stream is the only one used for this analysis. Other streams are not discussed.

Trigger conditions

In normal operation mode, the IceCube detector records data only when one or more of a list of conditions is met, known as triggers. Different triggers operate simultaneously serving multiple research purposes. For this analysis only the "Simple Majority Trigger" with 3 DOMs in the DeepCore fiducial volume (SMT3) is used[1]. The trigger, whose details can be found in [118, 146], requires a minimum of three DOMs in "hard local coincidence" (HLC) mode within a 2.5 μs time window[2]. If the detector triggers, a time window of $\pm 10\,\mu$s around the trigger time is created, and all the DOMs above threshold within this time are readout. The information from this slice of time is known as an *event*.

The trigger conditions, with 3 DOMs in HLC mode, are very loose, which result in a rate of close to 200 Hz [118]. The experiment has a limited bandwidth for transferring its data to the IceCube central repository in the United States, so the data have to be further reduced before transmission.

[1] The fiducial volume is defined in Section 5.2.2.

[2] The details about local coincidence and the readout modes can be found in Section 5.2.1.

In-situ filter

The first filter is applied at the South Pole. The filter's purpose is to reduce the data volume to be transferred. The filter targets atmospheric muons, which can leave signals that they have entered the DeepCore volume. The filter, presented in detail in [118], starts by constructing a simple guess for a neutrino interaction vertex, given by the average positions and times of all the HLC pulses inside the DeepCore volume. The standard deviation of the time of these pulses, σ_t, is also calculated. HLC signals outside a $3\,\sigma_t$ time window from the mean, which match the hypothesis of a muon entering the DeepCore volume, are searched for. If two or more pulses are found the event is rejected. This reduces the data rate to about 24 Hz, keeping 99 % of ν_μ while rejecting 96 % of atmospheric muons. Data that does not pass the criterion is not transferred to the central repository, but is stored on tape at the site and brought to the repository once per year.

Pure noise events

The noise rate of DeepCore DOMs is about 650 Hz [120], so there is a non-negligible chance that the SMT3 trigger condition is met by pure noise. Noise events are removed by two methods:

- The event is scanned with a sliding 200 ns time window, searching for the time window which contains the largest integrated charge in the detector. The integrated charge and number of pulses found are the cut variables. To keep an event, a time window with an integrated charge larger than 2 PEs and more than 2 pulses is required. The cut keeps 70 % of the the ν_μ events.

- Events are examined for hints of some directionality by using pairs of pulses. Taking a sliding time window of 750 ns, 48 directional configurations are tested. For each direction, pairs of pulses with apparent velocities in the range of $[0.1,\ 1.0]$ m/ns are searched for. The variable upon which the cut is performed is the maximum number of pulses found among all searched directions. A minimum of three pulses are required to accept an event. Close to 88 % of ν_μ events pass this selection.

Number of DOMs with pulses

The number of DOMs that have recorded at least one pulse is used to remove events which have too little information to be reconstructed. The single-string fit has four parameters, requiring at least five DOMs with signal pulses. To use the number of DOMs with signal pulses, noise pulses have to be removed from the event. For this analysis, this is done in three different ways, which are combined for the selection:

- Focusing on *direct* pulses (as described in Section 6.2.2).

- Using pulses from DOMs in HLC mode only.

- Taking pulses that are causally connected to the DOMs that triggered the event. A detailed explanation of the algorithm, known as seeded R-T-cleaning, can be found here [147, p. 70].

The first two methods leave very little noise contamination, but can disregard much of the information of an event. The third one is more complete, but is bound to contain a larger

Cleaned readout	Minimum required	ν_μ efficiency
Direct pulses	5	28 %
HLC mode	5	61 %
Seeded R-T	8	

noise contribution. For an event to be considered, a minimum number of DOMs with pulses are required from each of the three selections simultaneously:

The rejection of events without direct pulses has a low signal efficiency when compared with the rest of the selection steps. Its use, however, reduces the impact of the uncertainties on the optical properties of the medium, as it will be shown in Section 7.2.3.

7.1.2 Rejection of atmospheric muons

Atmospheric muons are, by far, the largest source of background for neutrino searches in IceCube. At trigger level, they outnumber neutrinos by a factor of 10^6. Several algorithms that attempt to identify and suppress these events are implemented.

The bulk of the atmospheric muons recorded in IceCube arrive at the detector as minimally ionizing particles. A typical muon leaves a clear signature as it enters the instrumented volume of IceCube, and tagging it can be done by searching for a large charge deposited outside DeepCore. However, underfluctuations of the light yield of muons are not negligible. As a result, a small fraction of muons are "dim" enough to cross several layers of instrumentation undetected.

Because of the enormous difference in rates, "dim" muons are observed in greater numbers than the neutrinos of interest for this analysis. It is the rejection of these muons which requires the use of sophisticated case-tailored algorithms. Only then a sample with high neutrino purity can be extracted.

Time evolution of light deposition

A neutrino interaction always initiates a cascade of some sort at the the point where it interacts. Cascades, both electromagnetic and hadronic, produce more light per unit length along the travel direction than a muon (see Section 6.1). Therefore, by analyzing the evolution of light deposition in a short time interval after the interaction, it is possible to discriminate muons that cross the detector from neutrino interactions which take place inside it. Figure 7.1a sketches the expected situation for muons and neutrinos.

The variable constructed from this idea is the ratio of the charge deposited during 600 ns after the trigger time t_0, to the total charge of the event,

$$Q_{\text{ratio}} \equiv \frac{\sum_{t_0}^{t_0+600\,\text{ns}} Q_i}{\sum Q}. \tag{7.2}$$

where the subscript i runs over the pulses of the event. The first two pulses of the event are discarded in order to avoid counting early noise.

For a particle traveling close to the speed of light, the time window results in a distance of about 180 m. A muon that crosses the detector can leave pulses over distances of 1 km. The distribution for muons and starting muon neutrinos are shown in Fig. 7.1b. A value larger than 0.4 is required in order to accept an event. The cut rejects 72 % of the atmospheric muons, while keeping 94 % of ν_μ events.

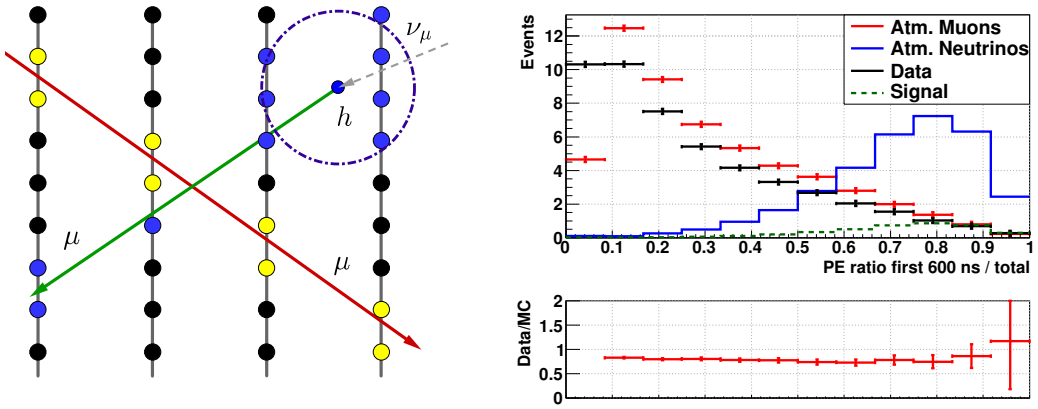

(a) Principle of the Q_{ratio} variable

(b) Distribution of Q_{ratio}

Figure 7.1: In (a) the expected light deposition of ν_μ starting (green-blue) and through-going (red-yellow) muons is depicted. Starting events have a larger relative light production around the interaction point. In (b) the distributions for signal, background and data are shown.

First DOM in HLC mode

Atmospheric neutrinos are expected to interact with the same probability over all of the detector volume. The location where their first pulse is observed depends only on the instrumentation density. Atmospheric muons, on the other hand, enter the detector, and thus have a higher chance to leave their first pulses in the outer-most DOMs. To construct a cut variable from this information it is necessary to look at the cleanest selection of pulses available, which is the one composed by the DOMs in HLC mode.

The position of the earliest DOM in HLC mode is taken as the earliest signature of a particle in the detector. The depth of this DOM and its radial distance to string 36, which is roughly at the center of the instrumented volume, are the variables tested. The distribution of the position of the first HLC in radius and depth is shown in Fig. 7.2. In order to accept an event, the first HLC has to be within a 200 m radius from string 36 and at a depth between [-2 445, -2 158] m. This depth covers DeepCore DOMs 11 to 59, and IceCube DOMs 43 to 59. The values selected reject 67 % of atmospheric muons and keep 70 % of the ν_μ sample.

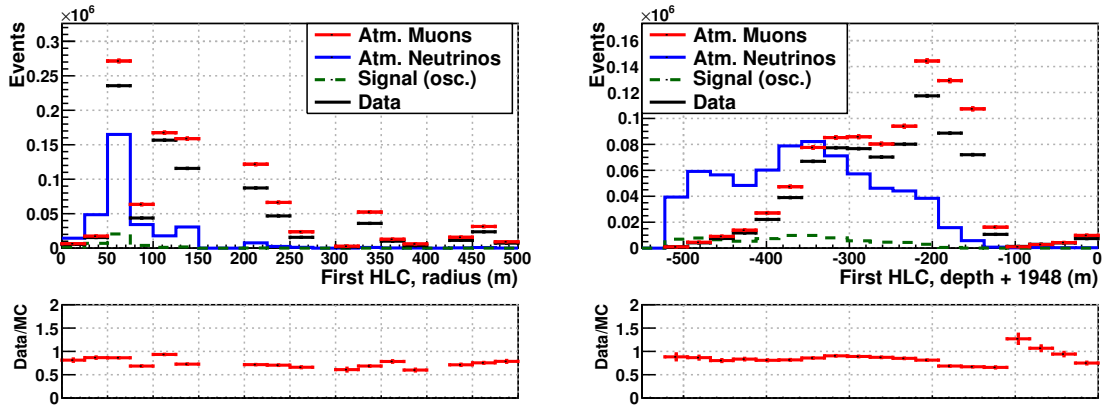

Figure 7.2: Distributions of the position of the earliest DOM in HLC mode in distance to string 36 (left) and depth (right).

Clustered pulses in the veto region

Dim muons can enter the detector without leaving pulses in DOM pairs, making the HLC tagging strategy insufficient. Nevertheless, in some cases they leave signatures close enough in time such that they can be traced to a single light source. Figure 7.3a shows how a cluster of pulses can be missed by the local coincidence logic, but identified by looking at all DOMs, even those not in HLC mode. A cluster search, trying to identify situations where this might happen, is done over all pulses in the veto region before the time of the trigger. The idea was develped and used for previous analysis of DeepCore data [148].

The veto region is scanned to search for pulses which could come from the same source. The search volume is limited to a cylinder of 250 m of radius and 150 m of height. The distribution of the largest clustered charge found is shown in Fig. 7.3b. If a cluster with an integrated charge of 3 PEs or more is found, the event is rejected. The cut keeps 94 % of ν_μ events, rejecting about 40 % of the atmospheric muon sample.

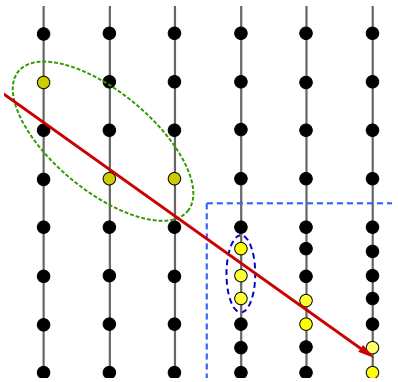

(a) Isolated pulses from a muon

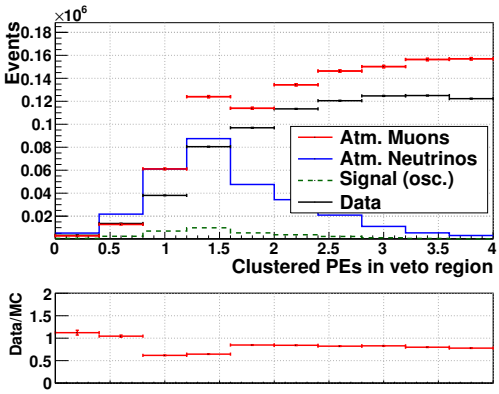

(b) Distribution of clustered charge

Figure 7.3: In (a) a muon enters the DeepCore volume after leaving traces in the veto region. The DOMs that trigger the experiment are marked in blue. In (b) the distributions of clustered charge for data, atmospheric muons and atmospheric neutrinos are shown.

Isolated pulses connected to the trigger

A complementary strategy for identifying dim muons is to integrate the charge of isolated pulses that can have a causal connection with the first DOM in HLC mode, as depicted in Fig. 7.4a. Unlike for the previous search, the pulses do not have to be clustered in a small volume. The description of the algorithm and its optimization can be found in [149].

The region where these pulses are searched for is given by the conditions

$$\begin{aligned} 750\,\mathrm{m} &> \Delta t_i\, c\,, \\ \frac{d_i}{c} - 500\,\mathrm{ns} &> \Delta t_i\,, \quad \text{and} \\ 1850\,\mathrm{ns} - \frac{d_i}{c} > \Delta t_i &> -150\,\mathrm{ns} - \frac{d_i}{c}\,. \end{aligned} \tag{7.3}$$

Here d_i is the distance to the reference DOM, and $\Delta t_i \equiv t_0 - t_i$ is the time difference between the pulses. No directional information is required for the search. The charge distributions for data and simulation are shown in Fig. 7.4b. In order to accept an event, the integrated charge

in the above defined region has to be smaller than 5 PE. An atmospheric muon rejection of 84 % is achieved, while keeping 69 % of ν_μ events.

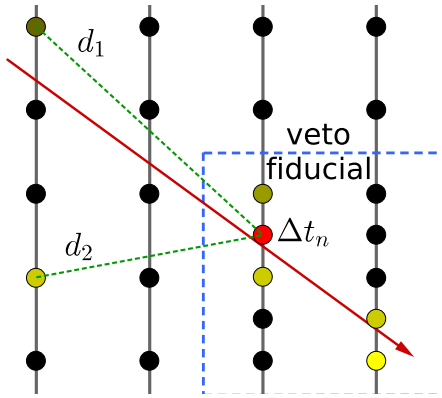

(a) Isolated pulses from a muon, noise

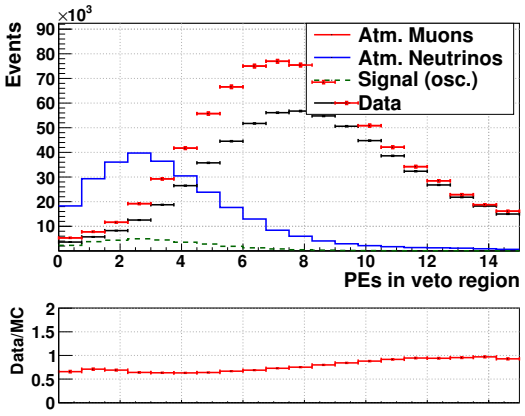

(b) Integrated isolated charge

Figure 7.4: In (a) a muon leaves an isolated pulse in the veto region, at a distance d_1, before the trigger. A pulse from noise is also present. To the right, in (b), the distributions of the integrated charge of all the pulses which fulfill the conditions in Eq. 7.3 are shown.

Isolated pulses from "blind" directions

The methods described before still fail to tag a substantial fraction of the atmospheric muons. The reason is that there are paths or corridors for which the detector has very little instrumentation, and thus a small probability to see a cluster of pulses or a large integrated charge. The detector is almost blind when looking at these directions. The DeepCore dedicated strings are not aligned in these blind directions, and dim events which are not seen in the veto region can leave a strong signal in the fiducial volume of DeepCore. Figure 7.5a shows the possible blind directions for an event which is first seen by one of the dedicated DeepCore strings.

To solve this particular problem, a search for isolated pulses from these blind directions was introduced for this analysis. The search starts by identifying the DeepCore string with the largest deposited charge. The average arrival time and z position of the signal are used to fix a point along a hypothetical muon track. The hypothetical track is rotated in zenith and azimuth. The azimuth steps are chosen to be aligned with the blind directions, while the zenith is scanned in small steps of 0.02 radians in the interval $[0, \pi/2]$.

For the defined direction, all the DOMs within a 75 m radius of the hypothetical track are analyzed. The DOMs which contain a pulse inside the time window given by $[t_0 - 150, t_0 + 250]$ ns, where t_0 is the expected time of arrival given the track hypothesis, are counted. The highest DOM count found is the variable used for the comparison. The distribution of this variable for the data and simulation are shown in Fig. 7.5b. Due to noise, neutrino events can have up to one DOM found by the algorithm. Events with more than one DOM found are rejected, resulting in the rejection of 28 % of the atmospheric muons, while keeping 94 % of ν_μ events.

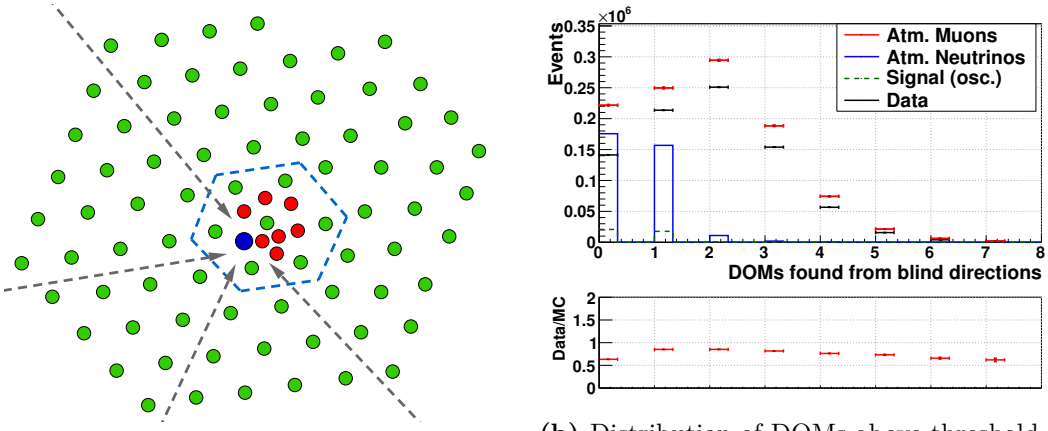

(a) Blind directions for a DeepCore event

(b) Distribution of DOMs above threshold from blind directions

Figure 7.5: The blind corridors available for an example DeepCore event are shown in (a) as dashed lines. The blue dot marks the first strong signal observed. The shaded area shows the fiducial volume. The distribution of the number of DOMs above threshold for blind directions is shown in (b).

Hints from directional reconstructions

The zenith reconstruction used as one of the observables in this analysis uses only direct hits. Muon neutrinos following up-going or horizontal trajectories have a good chance of having some of their emitted photons arriving unscattered. On the other hand, a muon traveling from the top towards the bottom of the detector can only be detected through scattered photons; the DOM acceptance drops to zero for these directions. Using direct hits only naturally removes muons traveling downwards, but it is still possible that the scattered photons fake a hyperbolic pattern and result in a wrong zenith angle estimation. In order to avoid this, the fitted zenith angles from two additional track reconstructions which make use of a selection of pulses with less restrictions were included. These are the *Line-Fit* and *Pandel* algorithms as presented in [150].

The behavior of the two reconstructions is shown in Fig. 7.6. If any of the two finds that the most likely path for a particle in the event is a down-going one, the event is rejected. The selection yields a rejection of 50 % of the atmospheric muon sample, while keeping 52 % of ν_μ events.

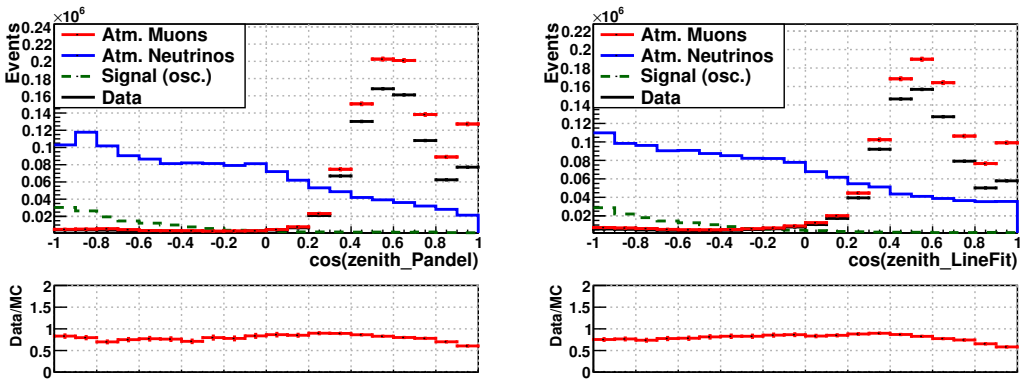

Figure 7.6: Distribution of zenith angle estimators obtained from track reconstructions. The algorithms use a selection of pulses wich include scattered photons.

7.1.3 Event quality

Applying the selection criteria described until now yields a sample with a roughly equal number of atmospheric muons and neutrinos. Using this as starting point, high event quality is the goal for the next steps. For this analysis, event quality is mainly defined by the number of direct pulses it produced, but other useful variables are included as well.

Reconstruction quality

The variable Q_{fit} is used to quantify the quality of the directional reconstruction described in Section 6.3 and used in the final level. It is defined like a reduced χ^2, as

$$Q_{\text{fit}} = \frac{\chi^2_{\text{mod}}}{N_{\text{pulses}} - P}, \tag{7.4}$$

where P stands for the number of parameters fitted and χ^2_{mod} is defined in Eq. 6.28. Despite the similarities with a reduced χ^2, the scale of the fit quality is dominated by the second term in Eq. 6.28, which is related to the charge. A large weight for this term was found to yield the best results for the directional reconstruction. How the scale is modified by the term can be seen from the distribution of the fit quality, shown in Fig. 7.7. The fit quality is different for events reconstructed using a single string and multiple strings, so the cut values also differ. For an event to be selected, the value of Q_{fit} must be smaller than 20 and 60 for single- and multi-string reconstructions, respectively. These cuts remove 98 % of the atmospheric muons with direct hits found, while keeping 55 % of ν_μ events.

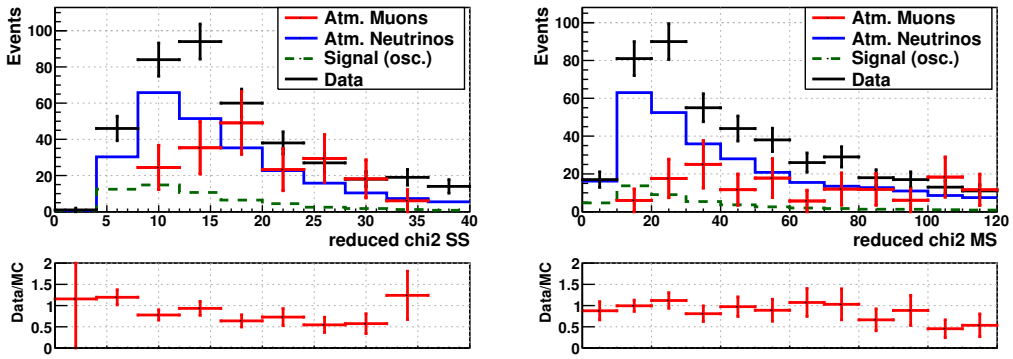

Figure 7.7: Distribution of the fit quality parameter Q_{fit} for single-string (left) and multi-string (right) reconstructions.

Ratio between fit hypotheses

Track and cascade or bright point hypotheses are fit for every event, given that there are enough direct pulses to do so. Using these fits, the ratio between fit qualities can be calculated as

$$Q_{\text{ratio}} = \frac{\chi^2_{\text{cascade}}/(N_{\text{DOMs}} - 3)}{\chi^2_{\text{track}}/(N_{\text{DOMs}} - 4)}\,. \tag{7.5}$$

Following this definition, a small value of Q_{ratio} means that the event is more "track-like". Here again the cut value needs to be determined for single- and multi-string reconstructions separately. The Q_{ratio} distribution for muon neutrino and electron neutrino events is shown

in Fig. 7.8. Events with a Q_{ratio} smaller than 0.6 and 0.8, for single- and multi-string fits, respectively, are kept. The cut keeps 51 % of the ν_μ sample, rejecting 92 % of atmospheric muons.

The reconstructed length of the track was also tested for discriminating ν_μ CC events from cascade events. The results were not as satisfactory as those obtained from the hypotheses ratio.

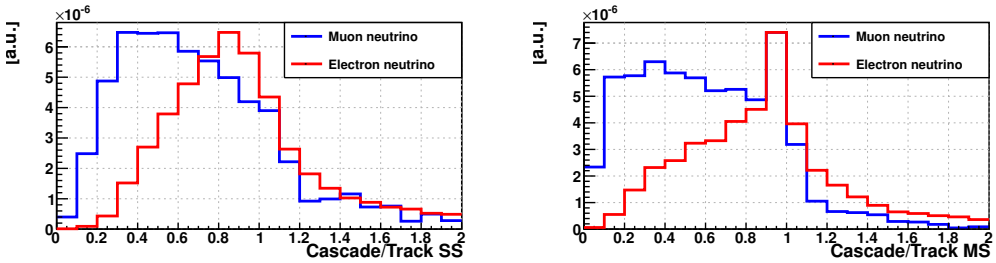

Figure 7.8: Distribution of the particle hypotheses ratio Q_{ratio} for CC ν_μ and ν_e interactions. Single-string fits on the left side, multi-string fits on the right.

7.1.4 Range of observables included

There are two further cuts that are made before the final sample is obtained. They are necessary because of limitations of the simulation being used, and could be removed if the underlying problems are solved. These are cuts on the reconstructed variables used for the comparison between data and simulation.

Reconstructed energy

The simulation of neutrino events was done for an energy range between 4 GeV and 190 GeV. The detector is not sensitive to neutrinos with energies below 4 GeV, which justifies the selected lower bound. Besides that, from the discussion at the end of Chapter 2, we know that the cross-sections for the different final states below 10 GeV are rather uncertain. On the high energy end, events with neutrino energies higher than 190 GeV are not included in the simulation used for the final analysis, even though they can be produced by atmospheric neutrinos. They were simulated using a different set of tools, and were found to make up a significant fraction of the sample only at reconstructed energies higher than about 150 GeV.

To avoid introducing the problems described above, a cut on the reconstructed energy is used. The final sample considers only events with a reconstructed energy in the range of $[7 - 100]$ GeV. The signal from oscillations becomes smaller as the energy increases, thus the restriction does not affect the sensitivity of the analysis.

Reconstructed zenith angle

As it can be seen from the figures accompanying the event selection, the atmospheric muon simulation does not describe the data with good precision. For producing the estimates in the figures only a baseline model was used, leaving out the consequences of uncertainties in the modeling of the cosmic rays interactions. The level of understanding of the flux of atmospheric muons in IceCube does not match that of the neutrino one. If atmospheric muons are included, they are bound to decrease the significance of the measurement.

The best way to deal with them is to remove them completely from the sample, which is only achieved successfully for the up-going region. Even with the veto, the down-going region of the parameter space has a large atmospheric muon component, and thus is not used in the analysis. Here again no effects are expected from oscillations, so there is no impact on the sensitivity. Only events with a reconstructed zenith angle larger than $\pi/2$ are included in the final sample. Restricting the energy and zenith angle range results in a rejection of 95 % of atmospheric muons, while keeping 52 % of the ν_μ sample.

7.1.5 Event selection summary

Table 7.1 summarizes the data selection. All variables and passing conditions are shown. The signal efficiency of the cut and the effectiveness in rejection of atmospheric muons are also included.

Appart from the selection of direct photons, which was already addressed, the quality cuts have the smallest ν_μ efficiency. Despite this, using them increases the sensitivity to the oscillation parameters by about 40 %. These cuts select events with reliable energy and zenith angle reconstructions, which has a large impact on the outcome of the analysis.

Some of the variables used in the selection could be correlated, as it can be deduced by their description. One example are the veto algorithms. They exploid the same information in different ways, but their results have been seen to overlap for some particular class of events. Due to time constraints, the correlations were not studied as part of this analysis. Nevertheless, a careful analysis of the collective behavior of the variables could improve the number of useful ν_μ events kept.

Table 7.1: Summary of the selection variables used with the corresponding cut values. N_{DOMs} refers to number of DOMs above threshold. The time of the trigger is denoted t_0. SS and MS stand for single-string and multi-string fits, respectively.

Test or variable	Passing condition	μ rejection	ν_μ eff.
Trigger $N_{\text{HLC-DOMs}}$	$\geqslant 3$	-	
Filter $N_{\text{HLC-DOMs}}$	$\simeq 1$	96 %	99 %
max $(\sum Q)$ in 200 ns	> 2 PE & > 2 pulses	45 %	70 %
max (N_{pulses}) with directionality	$\geqslant 3$	27 %	88 %
N_{DOMs} with *direct* pulses	$\geqslant 5$	57 %	28 %
$N_{\text{HLC-DOMs}}$	$\geqslant 5$	96 %	99 %
N_{DOMs} in seeded R-T search	$\geqslant 8$		
$\sum Q$ in first 200 ns / $\sum Q_{tot}$	$\geqslant 0.4$	72 %	94 %
Position of first HLC DOM	$r < 200$ m $-2\,445$ m $> z > -2\,158$ m	67 %	70 %
$\sum Q$ of causally connected pulses	< 5 PE	84 %	69 %
max $(\sum Q_{\text{clustered}})$ in veto before t_0	< 3 PE	39 %	94 %
max (N_{DOMs}) from blind directions	< 2	28 %	97 %
$\cos\theta_{\text{fit}}$ from Pandel and LineFit	< 0	50 %	52 %
Q_{fit}	< 20 (SS), < 60 (MS)	98 %	55 %
Q_{ratio}	< 0.6 (SS), < 0.8 (MS)	92 %	51 %
E_{reco} (observable for analysis)	7 GeV $< E <$ 100 GeV	95 %	52 %
$\cos\theta_{\text{reco}}$ (observable for analysis)	< 0		

7.2 Description of the final sample

7.2.1 The ν_μ CC component

The true energy and zenith angle distributions for the ν_μ component of the final sample are shown in Fig. 7.9. They include the expectations for the case of no oscillations and the case resulting from using the best known oscillation parameters. For a year of livetime, about 1 500 events are expected, with close to 500 of them disappearing due to oscillations.

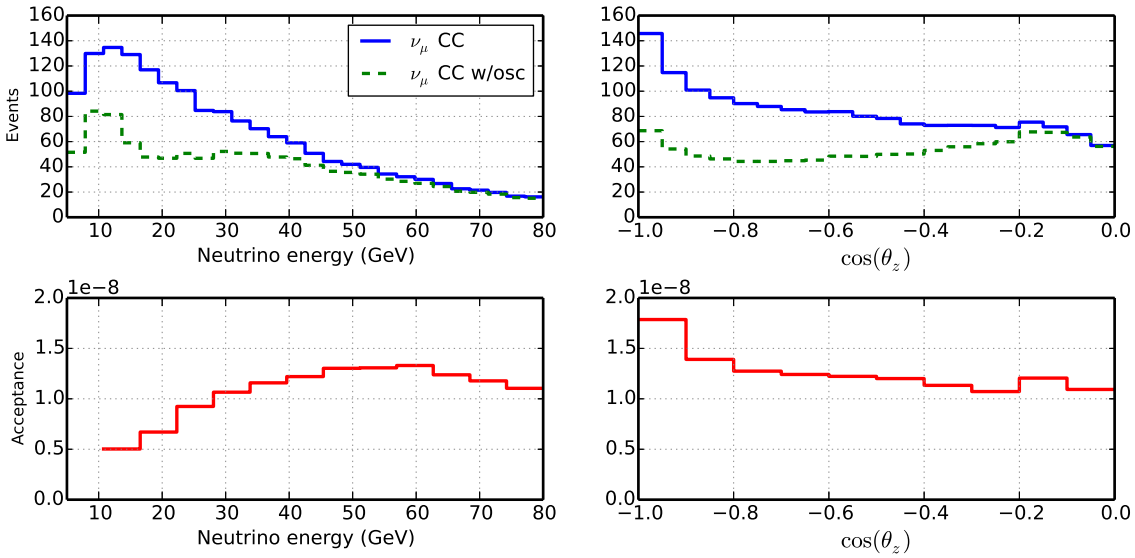

Figure 7.9: Energy (top) and zenith angle (bottom) distribution of the final sample, as given by simulations. The cases with and without oscillations are shown. Below each distribution, the acceptance of the event selection is shown.

The neutrino energy distribution of the ν_μ sample peaks at a value of about 12 GeV. At those energies the oscillation minimum is estimated to be around $\cos\theta_z = -0.5$ (see Fig. 5.10). As the energy goes up, the minimum moves towards the vertical up-going paths. Being able to observe the movement of the minimum position allows making a more precise determination of the mass-splitting with respect to the case where such movement is not observable. As the resolution of the reconstruction algorithms used degrades with energy, the analysis can only see a hint of this movement (discussed in the next Chapter).

The acceptance as a function of zenith angle and energy are shown also in Fig. 7.9. The highest efficiency is reached for $E_\nu \sim 50$ GeV. For lower energies, it drops by half. The energy threshold for very vertical incoming neutrino directions is lower than that for horizontal neutrino directions. Combining this with the spectral shape returns a zenith angle distribution that peaks at the up-going direction. This is a desired effect. The disappearance probability is expected to be the largest for the travel distances L associated with these zenith angles.

Characteristics of the events selected

Muon neutrino interactions where the cascade takes most of the energy and only a short muon is produced are removed by the selection steps. This changes the y distribution of the sample, but modifies the overall $\nu_\mu/\bar{\nu}_\mu$ ratio only slightly. Figure 7.10 shows both variables for the events that interact in the detector volume and for those that pass the selection criteria.

The y distribution of ν_μ starts close to constant, which changes to a distribution that peaks near $y = 0.15$ after the selection is applied. For the antineutrinos the change is not as large, although a similar effect takes place. The neutrino to antineutrino ratio $\nu_\mu/\bar{\nu}_\mu$ can be seen in the right panel of the same figure. As said, the ratio is not strongly modified by the selection: it is larger than two for all energies and it slightly rises with energy.

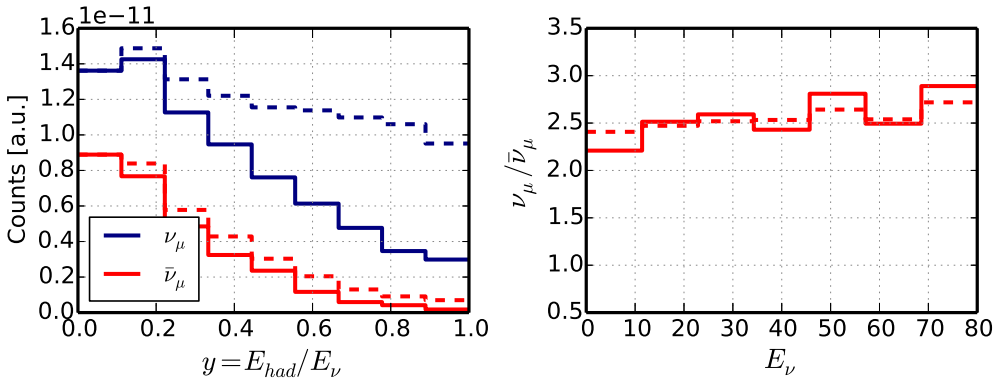

Figure 7.10: On the left, the y distribution for neutrinos and antineutrinos is shown. The figure to the right shows the ratio of ν_μ to $\bar{\nu}_\mu$ as a function of energy. Dashed lines correspond to all events which interact in the detector's volume (no selection applied); solid lines include only events in the final sample. Solid lines have been rescaled to match dashed lines at $y = 0$.

The final sample distribution of ν_μ CC events as a function of the muon range is shown in Fig. 7.11. More than 80 % of the selected muon neutrinos have a muon with a range larger than 25 m, which allows obtaining a good angular reconstruction, as shown in Fig. 7.12. Neutrinos and antineutrinos have a similar distribution, which is connected to selection effects, as demonstrated by the y variable in Fig. 7.10.

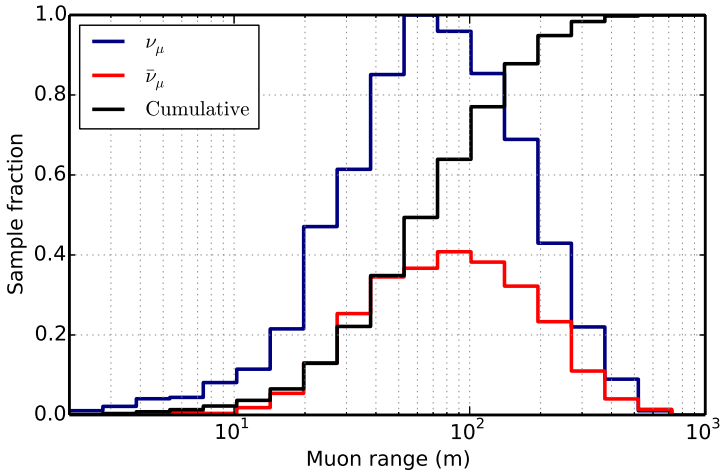

Figure 7.11: Expected distribution of the muon range for the CC ν_μ events in the final sample. The cumulative distribution includes both ν_μ and $\bar{\nu}_\mu$.

Reconstructed variables

The zenith angle and energy resolutions achieved can be seen in Fig. 7.12. The Figure shows the median error of the zenith angle reconstruction with respect to the neutrino and muon direction. The values are almost identical, and this can be understood from the selection effect shown in Fig. 7.10. Events with small y (large kinematic angle between the muon and the parent neutrino) are removed from the sample, keeping only those where the direction of both particles is smaller than the error of the reconstruction algorithm. The error on the zenith angle starts at around 14 degrees for the neutrinos with the lowest energies in the sample, crossing the 10 degree boundary at around 12 GeV, where the sample peaks. The energy estimator of the full sample has a bias of about 2 GeV at the lowest energies, which drops to 1 GeV already at 20 GeV. The resolution is of 50 % at 10 GeV, and improves to 40 % for higher energies.

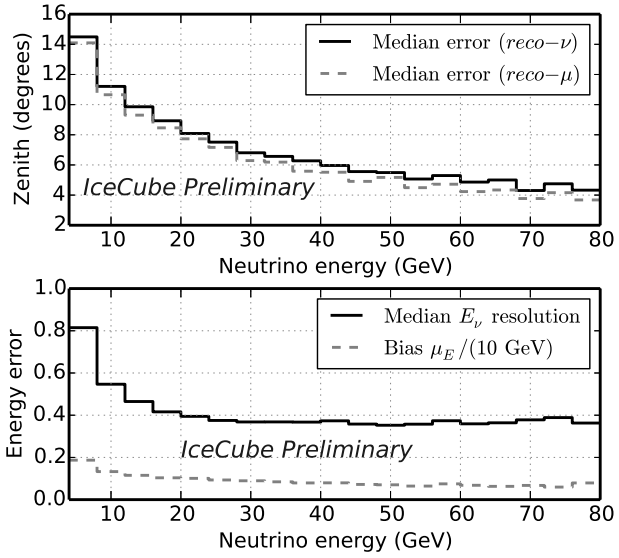

Figure 7.12: Performance of reconstructions for the ν_μ CC component of the final sample. Top: median zenith error in degrees as a function of neutrino energy, compared with neutrino and muon directions. Bottom: resolution and bias of the energy estimator as a function of the true neutrino energy. Units are given in the label.

7.2.2 Detailed composition of the sample

The different contributions as expected for the final sample, oscillations included, are listed in Table 7.2. The reconstructed energy and zenith angle distribution are shown in Fig. 7.13. The muon neutrino purity is 72 %, and is always the largest contribution over the parameter space covered by the observables. The strong peak at 10 GeV from the true energy distribution of Fig. 7.9 has been diluted due to the energy resolution. The contamination of atmospheric muons is expected to be about 7 %. The events have a strong energy dependence, and are mainly misreconstructed around the horizon.

The neutrino background amounts to 21 % of the final sample. From the neutrino background, the ν_τ component contribution is of 49 events per year, mostly from very vertical directions. This means that close to 10 % of the events that oscillate from ν_μ to ν_τ interact and leave a signature strong enough so that they are selected to be part of the final sample. Electron neutrinos and neutral current interactions appear very similar to the reconstruction algorithms, and compared with the other contributions, their distributions have little structure.

Table 7.2: Expected composition of the final sample. Calculated using the baseline simulation and the best known values for oscillation parameters, as shown in Table 4.1.

Component	Events per year	Fraction
CC $\nu_\mu + \bar{\nu}_\mu$	1063	0.72
CC $\nu_e + \bar{\nu}_e$	170	0.12
CC $\nu_\tau + \bar{\nu}_\tau$	49	0.03
All flavor NC	92	0.06
Atmospheric μ	110	0.07

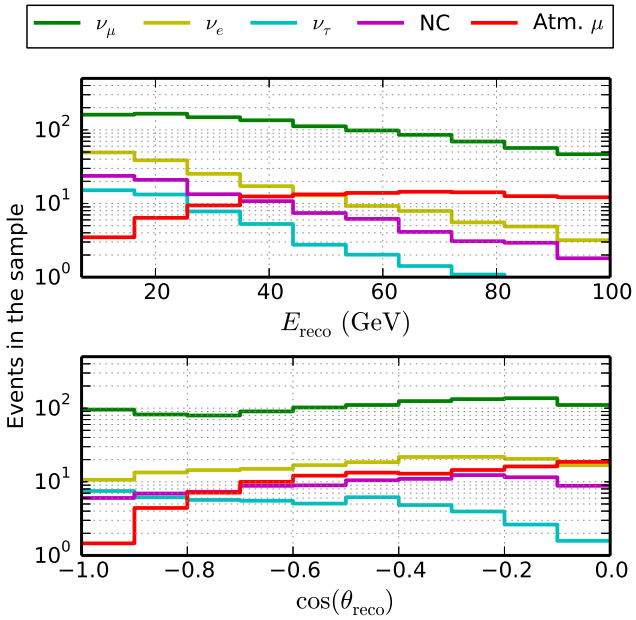

Figure 7.13: Reconstructed energy (top) and zenith angle (bottom) distribution of the final sample, as given by simulations. Oscillations with the values from Table 4.1 are included.

7.2.3 Effects of systematic uncertainties

The oscillation effect leading to the disappearance of ν_μ is known to be strong, guaranteeing an observation (see Section 4.1). However, in order to contribute to the field, one needs to properly account for possible sources of biases, which can distort the observations. A description of the systematic uncertainties considered and how the affect they affect the ν_μ component in the relevant distributions of energy and zenith angle follows.

The neutrino flux in DeepCore

The absolute scale of the atmospheric muon neutrino flux in the energy range between 10 GeV and 100 GeV has been measured to an accuracy of about 30 %. The electron neutrino component of the flux has been studied even less, which is reflected in an uncertainty of 50 % in its overall scale (see Fig. 5.5). The effect expected from oscillations is a deficit of up to 40 % of events in specific regions of the L/E parameter space. Demanding a normalization with such large uncertainties has a very small effect in the outcome of the measurement. Because of these issues, the normalization is left unconstrained in the analysis, allowing it to partially absorb the effect of other variations. The comparison between data and simulation depends only on the shape of the distributions.

The knowledge on the spectral index of atmospheric neutrinos has an uncertainty of $E^{\pm 0.05}$ [128]. The effect of these variations on the ν_μ component of the final sample can be seen in Fig. 7.14. The reconstructed energy shows the expected effect, with variations as large as 5 %. The zenith angle distribution changes only by 2 %, mainly for trajectories that cross the entire Earth.

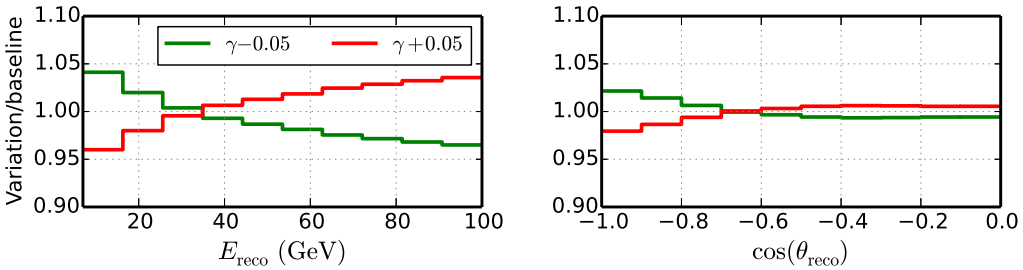

Figure 7.14: Impact of variations of the spectral index of atmospheric neutrinos on the final sample. The change in spectral index is applied on the same sample; no error bars are shown.

Detector

On the detector side the main source of uncertainty is the determination of the light collection efficiency of the DOMs. The impact of the overall efficiency is degenerated with the light yield of charge particles. In-situ internal studies have estimated this efficiency with an uncertainty of 10 %. The relative increase in quantum efficiency of DeepCore dedicated DOMs with respect to IceCube DOMs is known with a precision of 3 %.

Figure 7.15 demonstrates how a set of ν_μ simulation changes when the DOM efficiency varies. In the left panel, the overall efficiency has been modified. The first order effect is a change of ±6 % in the number of events in the sample, which is absrobed by the freedom to renormalize it. Besides that, the variation can modify the number of tracks seen from vertical directions. The relative difference in quantum efficiency between DOM types, right panel of Fig. 7.15 affects the event rate by less than 1 %. Varying this parameter does not change the distributions of interest significantly.

The South Pole ice

The optical properties of the South Pole ice are necessary to simulate the propagation of the photons that IceCube records. The uncertainties on these properties, discussed already in 5.2.3, can introduce large variations on the shape of the energy and zenith angle distributions of the neutrino sample, which are the observables that this analysis uses. This was one of the big motivations for using direct photons.

Figure 7.16 shows the variations for different ice models, comparing the results of this analysis (left) with the first oscillation analysis of IceCube [151] (right), which was not based on direct photons and used only the zenith angle information. The use of direct photons diminishes the average variation on $\cos\theta_{\mathrm{reco}}$ by more than half, from 7 % to 3 % (comparing WHAM models).

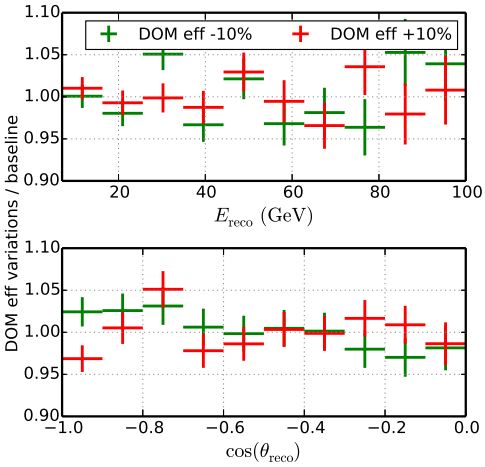

(a) Overall DOM efficiency

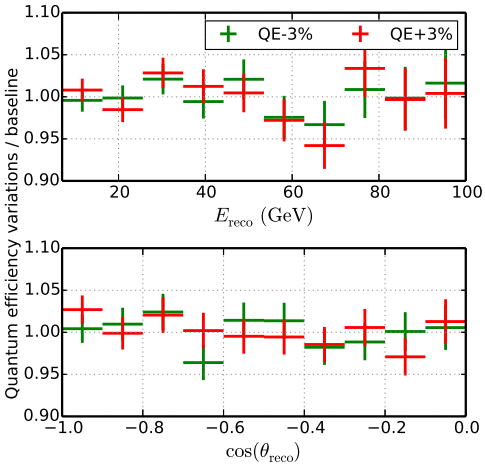

(b) DOM $\mathrm{eff}_{\mathrm{DeepCore}}$/DOM $\mathrm{eff}_{\mathrm{IceCube}}$

Figure 7.15: Ratio of the distribution of reconstructed variables after variations of (a) the DOM efficiency and (b) the relative efficiency of IceCube and DeepCore DOMs. Obtained from simulation.

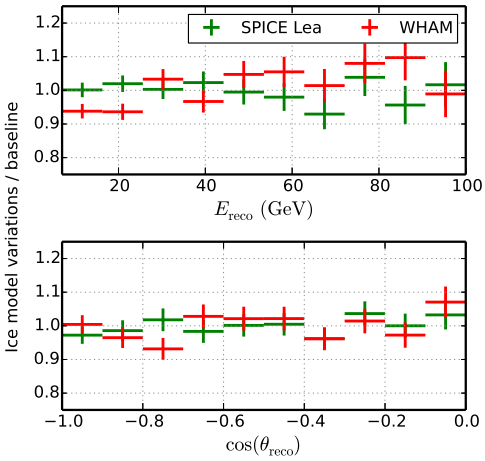

(a) This analysis

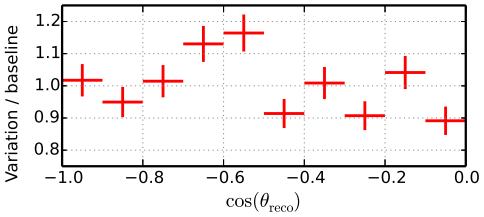

(b) First oscillation analysis

Figure 7.16: Ratio of the distribution of the reconstructed variables using different ice models with respect to the baseline model. In (a) the results for this analysis are shown. They can be compared with the results from the first oscillation analysis conducted with IceCube DeepCore [151], shown in (b). The ice models are described in [123, 124].

Borehole ice

To deploy the DOMs, columns of ice have to be melted. The water freezes back in a few weeks, forming ice with very different properties than the one that surrounds them. The borehole ice is approximated as a medium filled with bubbles, and described by the effective scattering α. Simulations show that the change in scattering has the same effect as modifying the angular acceptance of the DOMs. Figure 7.17 shows the effect, together with the variations that this introduces on the final ν_μ sample. The most noticeable change is a distortion of the zenith angle distribution, coming from energies below 20 GeV. The impact decreases rapidly with energy.

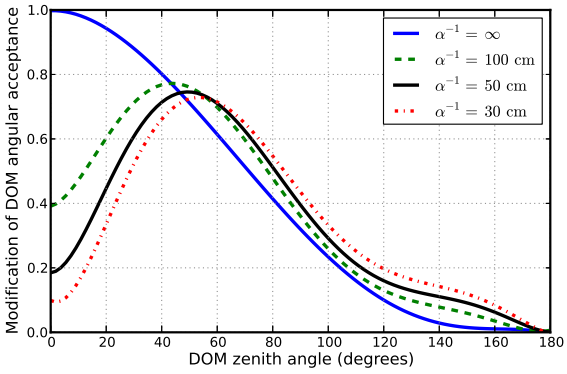

(a) Angular acceptance

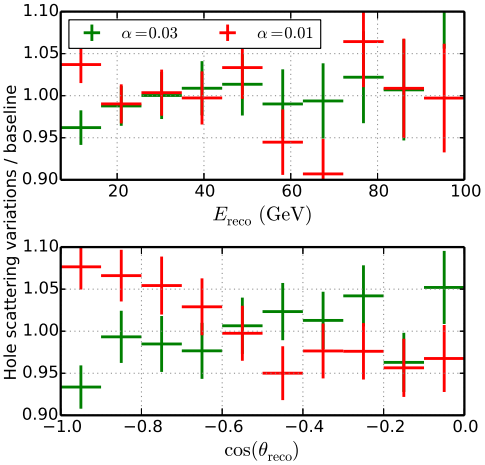

(b) First oscillation analysis

Figure 7.17: Impact of the description of the borehole ice on the angular acceptance of the DOMs, in (a), and on the final ν_μ sample. From simulation.

7.3 Fitting the oscillation parameters

The method to measure neutrino oscillations followed in this work is to compare the data with simulation templates. The parameters in the simulation are varied and the set that is most likely to explain the data is taken. The simulation is done by reproducing the interaction and detection steps, as described in Chapter 5, and then passing the events through the same analysis as the data. The resulting events are used to fill a two-dimensional histogram with the reconstructed energy and zenith angle on the axes. The performance of the reconstructions varies depending on the true parameters of the neutrino, and reproducing them in full in the simulation is the most straight-forward way of correctly accounting for them.

7.3.1 Statistical method

The method used to determine the oscillation parameters that the data favor is the binned maximum likelihood in the presence of nuisance parameters [152]. The two observables that modify the effect are the neutrino energy and the travel distance, while the two physical parameters of interest are the mixing angle θ_{23} and the mass difference $|\Delta m^2_{32}|$. The two-neutrino approximation, shown in Eq. 3.30, is used to calculate transition probabilities. As

discussed in Section 3.3.3, the mixing angle θ_{13} goes to zero for oscillations in matter, which allows the two-neutrino approximation to be accurate.

The likelihood used for the fit is composed of a Poisson and a Gaussian term, as

$$\mathcal{L}(\lambda, x, w; \mu, \sigma) = \prod_{i=1}^{n} \frac{\lambda_i^{x_i} e^{-\lambda_i}}{x_i} \prod_{j=1}^{m} \frac{1}{\sqrt{2\pi\sigma_j^2}} e^{-\frac{(w_j-\mu_j)^2}{2\sigma_j^2}} . \tag{7.6}$$

The Poisson term contains the probability for the prediction λ_i of a particular simulation set to explailn the data x_i in the i-th bin is calculated. The probabilities are multiplied, returning a value that can be compared with different λ_i hypotheses. The nuisance parameters included, denoted by the subscript j, enter in the Gaussian term. They appear because the simulation depends on their mean values μ, which are known to a precision σ which can be insufficient for our purposes. Their true value, however, is of no interest for this study. We account for them by allowing the hypotheses on their value w to change, penalizing their deviation from their mean value in units of their uncertainty.

The expression of Eq. 7.6 can be simplified by taking its logarithm. Also, since we are interested in comparing hypotheses, the absolute value of the likelihood is irrelevant, and constant factors can be eliminated. The simplified equation is then given by

$$LLH = \sum_{i=1}^{n} x_i \ln \lambda_i(\vec{\vartheta}, \vec{w}) - \lambda_i(\vec{\vartheta}, \vec{w}) - \frac{1}{2} \sum_{j=1}^{m} \frac{(w_j - \mu_j)^2}{\sigma_j^2} . \tag{7.7}$$

Here the same notation is used, with the exception that the dependence of the prediction on the oscillation parameters $\vec{\vartheta}$ and the nuisance parameters $\vec{w}$ is explicitly shown. Each of the events that end up in one of the bins of the histogram are weighted by the oscillation and nuisance parameters before they are summed up.

Data binning

The flux diminishes with energy. Because of this the histogram is binned in the logarithm of the estimated energy $\log_{10}(E_{\text{reco}}/\text{GeV})$. As the effect from oscillations depends on travel distance, and this is proportional to the cosine of the zenith angle (see Eq. 5.2), the binning is done in $\cos\theta_{\text{reco}}$.

Since the likelihood makes use of Poisson statistics, there is no minimum number of events per bin required. A finer binning allows to see more details of the data, but increases the number of calculations required to perform a fit. The effects on the sensitivity for using different number of bins were tested in a simulation sample, were it was found that after 8 bins the gain in sensitivity is marginal. Therefore, 8 bins are used for both axes.

Minimization

The only remaining step is to maximize Eq. 7.7 and thus find the parameters $\vec{\vartheta}$ and $\vec{w}$ that describe the data best. In order to properly do so, it is necessary to continuously modify the parameters involved and obtain new predictions for the mean values at each bin, λ_i. Because of the number of variables involved, the MINUIT computational package [153] was used for the task. The program performs a smart scan of the parameter space, and returns a set of values which yield the maximum likelihood that could be found.

7.3.2 Confidence regions

The precision of the measurement is determined by studying how much the likelihood changes as a function of the variables of interest in the vicinity of the best fit. When the fit is performed on variables that have no physical boundaries and no priors, the Wilks' theorem [154] shows that it is possible to assume that the distribution of the log-likelihood difference,

$$LLH_{\text{diff}} = -2\ (LLH_{\text{fit}} - LLH_{\text{alt}})\ , \tag{7.8}$$

between the best fit and an alternative point near it follows a χ^2 distribution, with a number of degrees of freedom that corresponds to the difference of the number of parameters fitted for both tests.

Once the map of likelihood values has been obtained the likelihood ratio is trivial to calculate. However, the problem being addressed in this analysis does not strictly fulfill the requirements of Wilks' theorem: there are physical limits to the values that some of the quantities can take, and prior knowledge is being enforced on some of the nuisance parameters. Whether the LLH_{diff} follows a χ^2 distribution has to be tested.

Figure 7.18 shows the LLH_{diff} distribution of pseudo-experiments, compared with the χ^2 distribution expected to describe them. Two situations are shown: ruling out the case of no oscillations and determining the confidence regions if certain oscillation parameters are measured.

- In the left panel, the pseudo-experiments are drawn from a sample that does not contain oscillations. No oscillations is the null hypothesis; the alternate hypotheses allow for oscillation parameters to be fit. The distribution follows a χ^2 with two degrees of freedom, thus Wilks' theorem is valid.

- The pseudo-experiments for the right panel are drawn from a sample that contains oscillations, calculated using the best known paremeters of Table 4.1. The null hypothesis is given by the input oscillation parameters, while the alternate hypotheses are obtained by fitting their values. As it can be seen in the Figure, the pseudo-experiments are not described by a χ^2 function with two degrees of freedom, but seem to fall in between the distributions given by a χ^2 with one and two degrees of freedom.

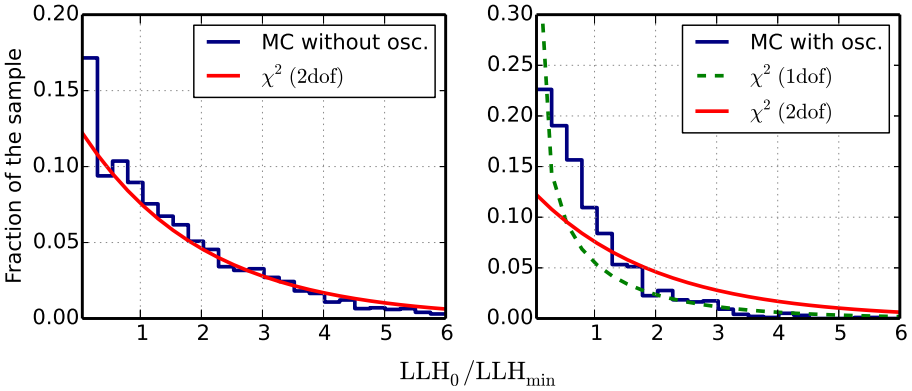

Figure 7.18: Distribution of the test statistic for 1000 pseudo-experiments. The distribution of the test statistic is compared with a χ^2 distribution. Description in the text.

Using the LLH_{diff} yields confidence regions which are bigger than they should be in certain regions. There are other alternatives for obtaining the confidence regions, which correctly deal with this type of situations, such as the one proposed by Feldman and Cousins [155]. However, they are computationally expensive as they require comparing the test statistic distribution of pseudo-experiments at each point of interest in the parameter space. As the LLH_{diff} over-estimates the errors, and it has been used by other experiments measuring the same effects [67, 156], it is used to obtain the final result.

7.3.3 Including systematic uncertainties in the fit

The effect of systematic uncertainties, with the exception of one to be discussed later, is accounted for by associating each source of error with a nuisance parameter, presented next. The energy-zenith angle distribution of the simulation depends on the value that the nuisance parameters take, and they are included in the maximization of the likelihood. The set of nuisance parameters can acquire any possible combination of values, which automatically takes correlations and degeneracies into account. Parameters with prior knowledge include a Gaussian term to the likelihood, as shown in Eq. 7.7. If there is no prior information about the parameter, no such term is added.

The sources of uncertainty that are included in the study are those related to the flux and the ones connected to the detection process. They are listed in Table 7.3, together with their allowed range and/or prior.

Table 7.3: List of systematic uncertainties included in the analysis as nuisance parameters with their corresponding ranges and priors.

Nuisance parameter	Prior
Atm. μ contamination	up to 10%
Atm. ν flux	None
Atm. ν_e/ν_μ	$\sigma = 20\%$
Spectral index from [112]	$\sigma = 0.05$
Photo collection efficiency	$\sigma = 10\%$
Efficiency increase of HQE DOMs	$\sigma = 3\%$
Scattering in ice columns [1/cm]	$\sigma = 0.02$
Bulk ice properties	See [124]

With the exception of the last item listed, the uncertainties are a function of a single variable. The value of this variable can be modified each time that the likelihood is calculated, allowing for a continuous minimization. The inclusion of the top four, related to the flux, implies modifying the relative weight of the events in the sample. The next three, on the other hand, are related to the detection process, and any change in their values would require resimulating all events. Since this is technically hard to achieve, a different approach was taken, where only simulations of parameter changes in discrete steps are required.

Parametrizing detection uncertainties

The number of photons N_γ that a DOM detects can be expressed as

$$N_\gamma = f \cdot g \cdot h \cdot N_0 \,, \tag{7.9}$$

where N_0 is the number of photons starting right outside the ice column traveling in the direction of the DOM. The functions f, g and h describe the overall efficiency of the IceCube DOMs, the relative efficiency between IceCube and DeepCore DOMs, and the optical properties of the ice column where the DOM sits, respectively. This formula is exact for photons only, but an approximation can be drawn from it for the case of full events.

Taking a reference simulation, variations are produced in which only one of the effects is changed. The sets are interpolated afterwards. The interpolation cannot be done on an event-by-event basis, as intrinsic variations and threshold effects will add and remove events from the sample. Instead, the interpolations are done on the bin contents of the histogram of observables.

The two-dimensional histogram used for the final analysis of the data has to be calculated for each simulation set. This means that all sets have to be put through the same analysis steps as the baseline simulation. During the fitting procedure, any change to the reference simulation, like a modification of the mixing angle, needs to be performed also on all the other simulation sets.

Once the changes to all sets have been made, the two-dimensional histogram used for the analysis is populated. One histogram is required for each simulation set. For each of the bins, a polynomial function F is found, which describes the change in counts as a function of the variation introduced. As in Eq. 7.9, F depends on the overall efficiency of the DOM. Figure 7.19 demonstrates how a fit for F is obtained for the effects of variations in the DOM efficiency in a particular bin.

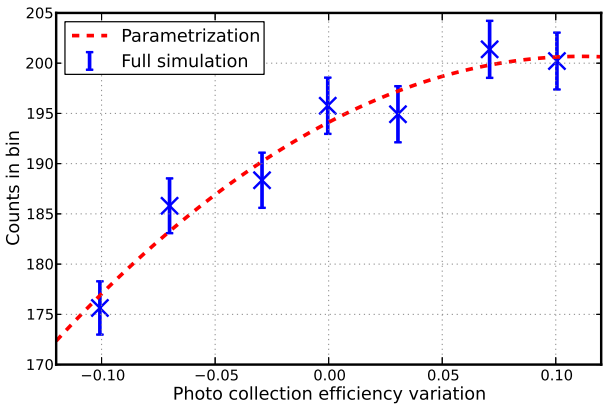

Figure 7.19: Fit of the impact of a given variation, light yield in this particular case, on the number of events in the i-th bin.

The functions G and H, for relative efficiency and angular acceptance, can be determined in the same way as the DOM efficiency. The number of events in the i-th bin of the energy-zenith angle histogram is then given by

$$N_i = F_i \cdot G_i \cdot H_i \cdot N_{i,\text{baseline}} \,. \tag{7.10}$$

Because of how the functions are defined, the formulation assumes that each detector effect can be parameterized and applied independently. According to simulation tests, the assumption is valid. The scheme presented can reproduce the results of full simulations with good accuracy.

Accounting for discrete optical descriptions of the medium

The path that a photon follows depends on the optical properties of the medium, which are defined by a set of 60 scattering and 60 absorption coefficients [123]. Besides that, the full description involves quantities related to the global tilt and anisotropies of the ice. Different approaches have been used within the IceCube Collaboration in order to model the optical properties of the ice [123,124]. The practical outcome is that there are different reasonable ice descriptions. They are used as an indicator of the uncertainty on the ice description. However, because of how the models are defined, it is not possible to make a smooth transition between them, like it is done for the case of nuisance parameters.

Three different models of the ice are used as an estimate of the uncertainty. The baseline corresponds to the one presented in [124]. The alternative models are a variation of [124] and an update of the one presented in [123]. This is included in the final result by following the steps shown next:

1. The baseline simulation, all nuisance parameters included, is used to determine the best fit value and the 68 % and 90 % confidence levels of the data.

2. Simulation sets are produced with different ice models. The effects of oscillations, as calculated from the best fit (Step 1), are included.

3. The newly created sets are treated as data and analyzed using the baseline simulation. The 68 % and 90 % confidence contours are also calculated.

4. Using the best fit of Step 1, the uncertainty on the boundary of the confidence regions is determined by summing the differences in quadrature.

5. The confidence regions from Step 1 are increased, point by point, to account for the uncertainty found in Step 4.

The resulting confidence intervals can only be larger than the original ones, increasing solely on regions where the models give results that differ. These results can also be used to study whether the entire method indeed reduces the effect of the medium properties, a much desired effect. This is analyzed in the next Chapter, when the results are presented.

Throughout this Chapter we discussed how the data have been selected, and the steps that are taken to analyze them. Requiring a clear signal and direct photons in the detector was used as a way of reducing the impact of systematic effects, a central part of the strategy. While this results in robust observables, the benefits have to be weighted with the number of events that are lost. For an analysis aiming for precision, such as the one presented here, they result in a sensitivity gain. The effects of this strategy can be seen in the following Chapter, where the results of analyzing a year of data are presented.

8 Results from the $\nu_\mu + \bar{\nu}_\mu$ disappearance measurement

8.1 Analysis of the data

The muon disappearance analysis described in the previous Chapter was applied to the data acquired by the IceCube DeepCore detector between May 2011 and April 2012. The period corresponds to a livetime of 343 days, during which a total of 1 487 events were selected. The shape of the two-dimensional distributions in reconstructed energy and zenith angle of these events were studied as a function of the oscillation and nuisance parameters. The results are a set of values for the best fit point, together with their confidence regions.

8.1.1 Comparisons between data and simulation

The distributions of data and simulation for the observables used in the analysis are compared next. The predictions from simulation have been produced using the baseline values of the nuisance parameters and the best fit point derived from the data, which is presented in Section 8.1.2. The simulation histograms are accompanied by error bands, which demonstrate the impact of the systematic uncertainties.

The normalization is free in the analysis but it has been fixed for the figures to match the region of $[0 > \cos\theta_{\text{reco}} > -0.25]$. The motive behind this is the perception of the comparisons. If the normalization is left free, the case of oscillations will have more events than the case of no oscillations in some regions, as the fit tries to match the total number of events. This is counterintuitive: the effect being searched for is that of *disappearance*. In order to avoid the confusion, the normalization was fixed. A similar solution was used in [157].

Distributions used for the fit

The full two-dimensional histogram in energy and zenith angle used for the fit is shown in Fig. 8.1a. The histogram is displayed in energy bands, following the binning used for the analysis. All of the energy bands are correctly described by the simulation, which is reflected by a χ^2/d.o.f. value of 48.8/54. Here the degrees of freedom are approximated as the number of bins used minus the number of nuisance and oscillation parameters obtained minus one.

The ratios of data and simulation without oscillations for each of the energy bands of Fig. 8.1a are shown in Fig. 8.1b. The disappearance effect can be followed in the Figure. At the highest energy bin both the oscillations and no-oscillations hypotheses overlap for all zenith angles. As we go down in energy, the deviation from unity starts growing, allowing one to separate the two possibilities. The bin that comprises the range between 20 GeV and 28 GeV shows the strongest effect. After that, there is a hint that the minimum starts moving. Instead of a stronger dip, the vertical region ($\cos\theta_{\text{reco}} < -0.8$) now appears flat. The effect expected, if L/E could be determined exactly, is a rise at around $\cos\theta_{\text{reco}} \sim -0.8$. However, the resolution of the reconstructions at $E_\nu = 10$ GeV and lower becomes large, so that the minimum cannot be resolved.

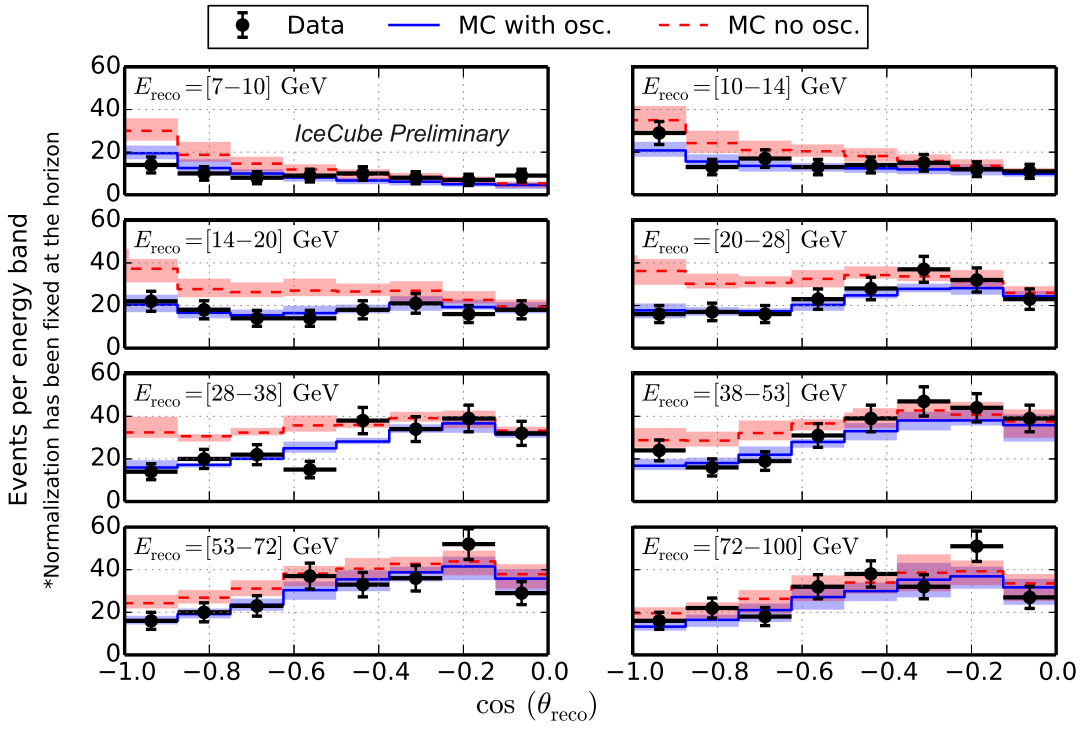

(a) Data comparisons: energy and zenith

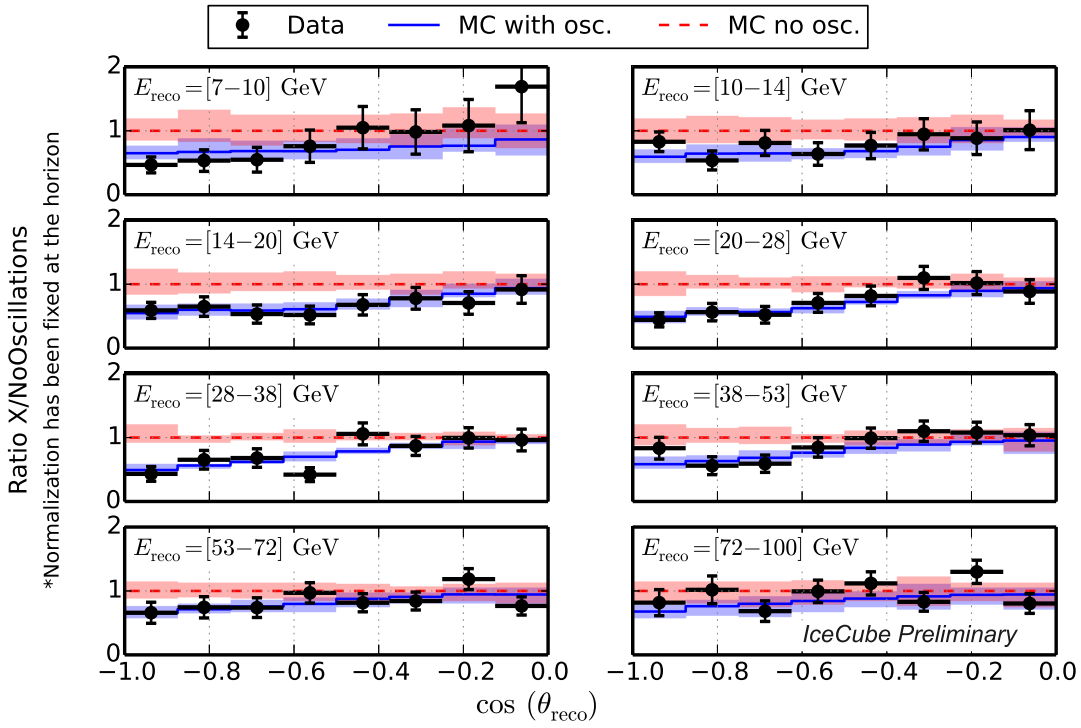

(b) Ratios to the no-oscillations case

Figure 8.1: In (a), the comparison between data and simulation for the full two-dimensional histogram used in the likelihood analysis. In (b), the ratios of data and simulation to the case of no oscillations.

Projections in one dimension

Figure 8.2a compares data and simulation as a function of the reconstructed energy. For the highest energies included, close to 100 GeV, the data agree with both predictions. Oscillations create a strong decrease between 10 GeV and 40 GeV, and the predictions match the data accurately. At the lowest energies, below 10 GeV, both predictions are within systematic uncertainties. The histogram of the data as a function of the reconstructed zenith angle variable is shown in Fig. 8.2b. At the horizon, $\cos(\theta_{\text{reco}}) = 0$, the predictions for the case of oscillations and no oscillations are almost identical in shape, which partly justifies fixing the normalization to this region. The disappearance effect starts growing when moving towards events that cross the entire Earth, as expected.

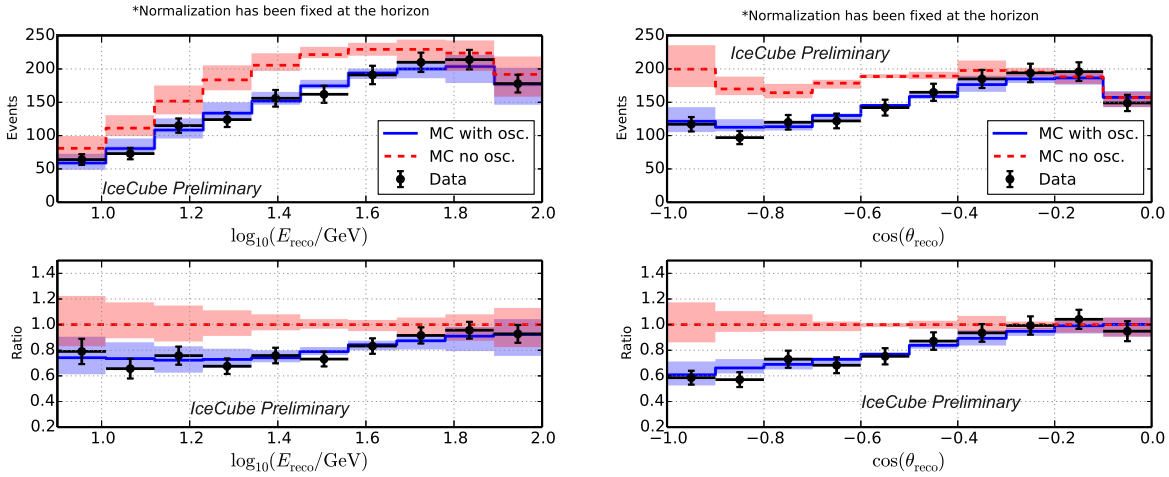

(a) Energy. **(b)** Zenith angle.

Figure 8.2: Top: comparison between data and simulation with and without oscillations as a function of (a) energy and (b) zenith angle. Bottom: ratio of data and simulation without oscillations.

Another illustrative way of looking at the results is by constructing the data histogram as a function of L/E. Even though the best fit is not obtained in this way, the variable can be used to corroborate that the data fit the model. Figure 8.3 shows the distribution of the data and the ratio of the two hypotheses. The minimum is reached slightly below $L_{\text{reco}}/E_{\text{reco}} \simeq 400\,\text{km/GeV}$, and the prediction starts rising for larger values.

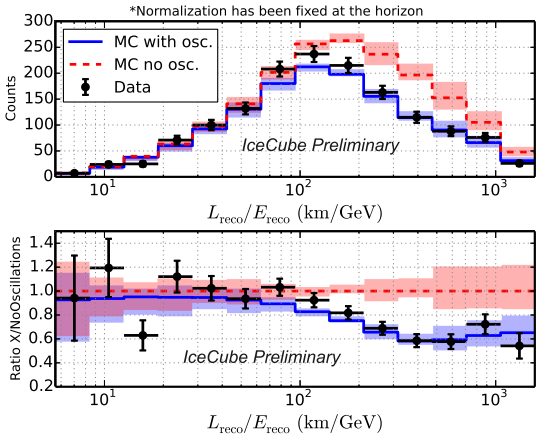

Figure 8.3: Top: comparison between data and simulation with and without oscillations as a function of L/E. Bottom: ratio of data and simulation without oscillations.

8.1.2 Best fit point and confidence intervals

The data were analyzed using the two-neutrino scheme in vacuum. Figure 8.4 shows the best fit point, as well as the 68 % and 90 % confidence intervals, as obtained from the likelihood scan. All the sources of uncertainty listed in Table 7.3 are included. The individual parameters that describe the data best are

$$\begin{aligned} \sin^2 2\theta_{23} &= 1.0 \; (> 0.94 \text{ at } 68\,\% \text{ C.L.}) \,, \\ \Delta m^2_{32} &= 2.4^{+0.6}_{-0.4} \cdot 10^{-3} \;\; \text{eV}^2 \,, \end{aligned} \tag{8.1}$$

where the errors have been estimated from the profile likelihood of each parameter.

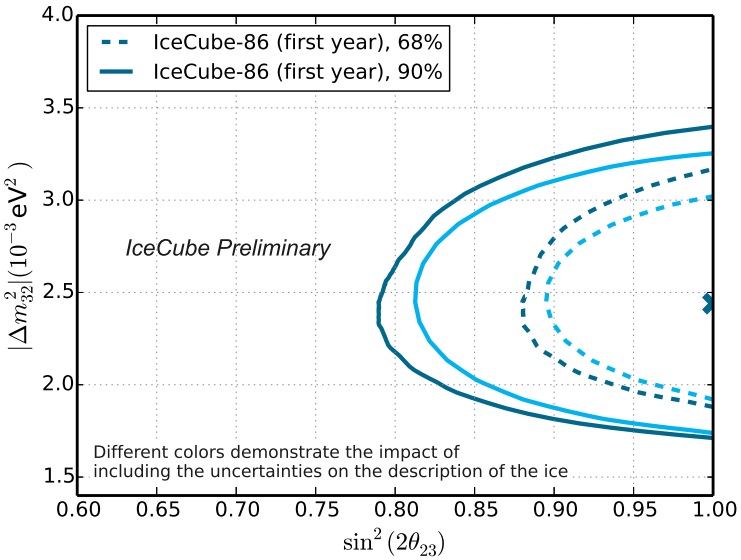

Figure 8.4: Confidence regions obtained with a year of data. The two sets of contours correspond to (light) neglecting the optical properties of the ice and (dark) including them.

The best fit in Eq. 8.1 was obtained using the physical constraint that $\sin^2 2\theta_{23}$ cannot be larger than 1. If this is removed, the value for the parameter moves to 1.12. This is expected: if the true value were to be 1, any experiment has a 50 % probability of deriving a value larger than 1. The unconstrained value of 1.12 is still within $1\,\sigma$ from the boundary, thus within expectations.

Systematic uncertainties of the fit

The impact of the uncertainties on the ice model can be seen in Fig. 8.4, which contains two sets of contours:

(i) light blue, with no modification of optical properties, and

(ii) dark blue, implementing the re-analysis of toy simulation obtained using the optical properties of the models in [123, 124].

After including the different models of the optical properties of the ice, the area covered by the 68 % C.L. grows by about 25 %. The increase of the error on the single parameters is about 20 %.

The values for the nuisance parameters at the best fit point are compiled in Table 8.1. The contamination of atmospheric muons is below 10 %, as expected from the simulation. All the parameters with prior knowledge are fit very close to the expectation shown in Table 7.3. The largest relative change, which is below half a standard deviation, comes from the photon collection efficiency, favoring a slightly higher value.

Once all these effects are taken into account, the difference between the case of oscillations and no-oscillations amounts to six standard deviations. This is estimated from the difference in likelihoods between the case of no oscillations and the best fit point.

Table 8.1 does not contain a deviation for the normalization of the atmospheric neutrino flux. The parameter that the fit outputs is correlated with most of the other systematic effects included, and cannot be taken as a good estimator of the true scale of the flux. It is planned to properly include the flux normalization in further updates to the analysis. The atmospheric muon flux also shows no deviation. The amount of simulation used only allowed for estimating an upper limit on the contamination of the sample, of 10 %.

Table 8.1: Values taken by the nuisance parameters at the best fit point between data and simulation. The deviations from the expectation is also shown.

Nuisance parameter	Value at best fit	$\frac{\text{Fit}-\mu}{\sigma}$
Atm. μ contamination	7.6%	-
Atm. ν flux	1.08	-
Atm. ν_e/ν_μ	1.02	< 0.01
Spectral index	2.66	0.2
Photo collection efficiency	1.02	0.3
Efficiency increase of HQE DOMs	1.35	< 0.01
Scattering in ice columns [1/cm]	0.018	0.15

8.1.3 Sensitivity to sub-leading effects

The sub-leading effects of the analysis are those listed in Chapter 5 as other possible studies. A brief discussion of their impact on the final sample used in this analysis follows.

Different oscillation patterns for ν_μ and $\bar{\nu}_\mu$

The final sample is a mixture of neutrinos and antineutrinos. Dividing the sample as a function of the $\nu : \bar{\nu}$ content would allow to study CPT violation from the possible differences in their oscillation patterns.

The ratio of $\nu_\mu : \bar{\nu}_\mu$ interactions in the detector volume, as a function of neutrino energy, starts with an almost constant $2:1$ ratio, as shown in the right panel of Fig. 7.10. The value is not modified after the selection steps are performed, so energy is not a good variable for obtaining a sample with varying $\nu_\mu/\bar{\nu}_\mu$ contributions.

The y distribution for neutrinos and antineutrinos is the only possibility left. When all interactions are taken, as shown in Fig. 7.10, the relative contribution of both samples gets close for small y values. However, after the selection is performed, the shape of the resulting distributions is too similar. Even if the y variable of each event could be recovered, this sample would not be suitable for such study. Possible CPT violation effects have no impact on the results obtained; the sample is uniformly dominated by ν_μ.

Appearance of ν_τ

The number of events in the final sample which are attributed to CC ν_τ interactions from $\nu_\mu \rightarrow \nu_\tau$ oscillations is about 50. Given that the sample contains about 1 500 events, a difference of 50 could mean an impact slightly bigger than one standard deviation. The full likelihood calculation, where the nuisance parameters are left to float but the ν_τ contribution is excluded, reduces the significance of the difference to about 0.8 standard deviations. The oscillation parameters retrieved are the same. With one year of data, the analysis presented here is not sensitive to the appearance of ν_τ.

Matter effects and neutrino mass hierarchy

As stated before, neutrinos dominate over antineutrinos by a 2:1 ratio over the entire sample, changing only slightly with energy. If the mass hierarchy is normal, the sample has the potential of being affected by matter effects, which would distort the oscillation pattern. Such a distortion could be seen in the ratio of expected events for the two hierarchies. For the final sample of this analysis, such a ratio is given in Fig. 8.5, as obtained from simulations.

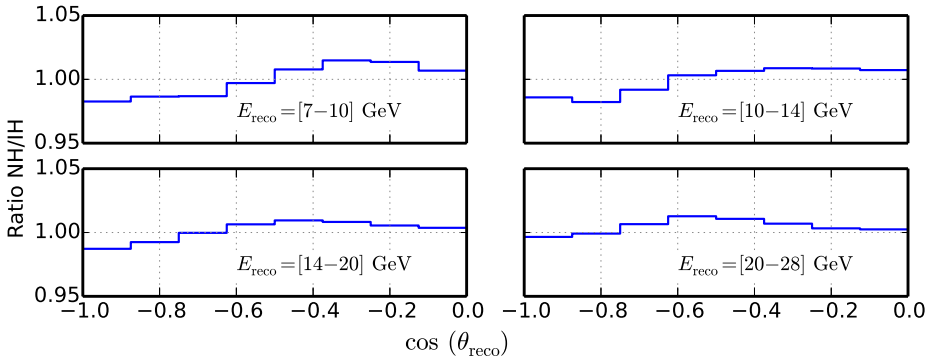

Figure 8.5: Ratio of the counts expected from the two different hierarchies, N_{NH}/N_{IH}, for the final sample is shown for different energies. Systematic uncertainties are several times larger than the maximum deviation expected.

The effect is rather small, with a maximum observable difference of about 2 %. This deviation is smaller than the effect of any of the systematic uncertainties of the detector. The analysis as it stands is not sensitive to the correct ordering of the neutrino masses.

8.2 Comparison of results

The final 90 % confidence interval for a year of data, with all sources of errors included, is shown in Fig. 8.6. The contour is depicted together with the corresponding regions allowed by MINOS, Super-Kamiokande and T2K, the most sensitive experiments in the field. The results, while in agreement, are not yet competitive with those of these experiments. Nevertheless, the measurement is performed at a neutrino energy that has only been recently explored by neutrino telescopes [151].

The fourth contour included in the figure corresponds to the extrapolation to 5 years of livetime using the current method. All of the systematic effects have been included. The sensitivity corresponds to the "sit and wait" scenario, in which no improvements are made. The results from IceCube DeepCore could enter a competitive regime within the next years, even if no modifications are made to the analysis presented here.

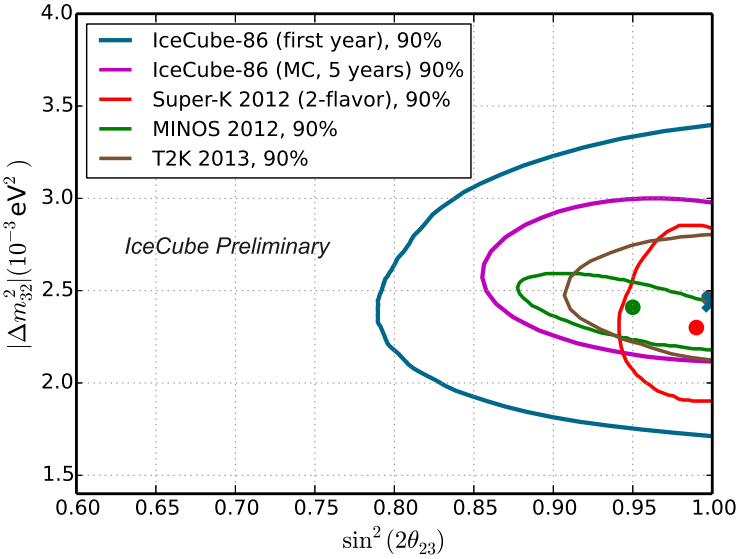

Figure 8.6: Comparison of the final results obtained in this analysis with MINOS [67], Super-Kamiokande [64], and T2K [156] results. The projection for the same analysis on 5 years of data is also included.

8.3 Evaluation of the method

8.3.1 Revisiting the analysis method

It is worthwhile to discuss some of the most important items used to achieve the results presented. Put together for the purpose of this measurement, they are by themselves a big part of the results of this work.

Direct light

The selection and reconstruction of the sample relies heavily on the identification of direct photons. Much of the agreement between data and simulation, and the independence to optical properties of the ice, comes from exploiting them. Note, however, that the use of non-scattered signals is not a novel idea. Several studies of the IceCube Collaboration have used them to determine how much individual reconstructions can be trusted. The main difference between previous efforts and the method described in Chapter 5 is that, for the latter one, a reconstruction is not necessary. There is not even a need for a particle hypothesis. The identification of direct photons is done by knowing the possible patterns that can appear. Its implementation is rather general and can be applied to any event topology.

Identification of muons from "blind" directions

A particularly useful method for reducing background, developed for this analysis, is the search for atmospheric muons that enter through the corridors formed by the alignment of the IceCube strings. These events proved resilient to being detected by any other existent method, even those which specifically aimed to remove them. The key difference in the tagging strategy implemented here is that only a discrete number of directions are scanned,

which are known to be problematic. Also, for each direction the full muon hypothesis is constructed, allowing one to restrict the search to a small time window around the expected arrival time.

Reconstruction of tracks and cascades

Having a set of non-scattered photons allows performing a directional fit that focuses mainly on the time of arrival of the signals. This removes pressure on the amount of light observed at the sensors, at least for this particular parameter. Missing photons typically have a small impact on the resolution that can be achieved, as long as the total number pulses detected is larger than the threshold of 5. The influence of noise and scattered photons on the reconstruction is controlled by the precise timing demands.

The estimation of the energy of a neutrino depends largely on how bright the event seems to the detector. Differences in the medium description have a much larger impact here. The characteristics of the sample help in controlling them, since it is composed by events that pass close to at least one string, thus having a large probability of depositing a considerable amount of light. The innovation on the energy reconstruction comes from dividing the secondary particles in track-like and cascade-like, and estimating the energy of each component individually. Within the limitations of the detector, this method, developed by A. Terliuk [143], gives reasonable results and allowed gaining sensitivity to the oscillation parameters.

Systematic uncertainties

Systematic uncertainties can be dealt with in different ways depending on the statistical method used to analyze the data. The implementation of nuisance parameters in the formulation of the likelihood has the advantage of returning a preferred value, which can be used as a gauge of how well the data are understood. Also, the variations of the value can be used to study the impact of a particular uncertainty. The method is not new, but how it was implemented in this analysis is. The generation of independent simulation sets to be parameterized at the final level histogram was introduced for this study, and proved to give good results.

The items listed can be ported to other studies within the IceCube experiment, and even other neutrino telescopes. Moreover, elements such as an analysis around a robust variable, and the parameterization of systematic uncertainties, can be used in experiments where direct calibration is complicated and/or faint signals are expected.

8.3.2 Possible improvements for future studies

The rapid gain in statistics translates into a strong constraint of the parameter space of the mass-splitting and an improvement on the mixing angle precision. However, in the 5 year prediction both parameters start being limited by uncertainties. The neutrino flux is the main one, with detector effects taking the second place. Possibilities that could result in a partial removal of these limitations are presented next.

The event selection

The selection of events was based on the existence of direct photons, but also on the removal of cascade-like events. However, if the cascades can be correctly tagged it is not necessary

to remove them fully. Neutral current events can be used to anchor the true neutrino flux because they are not affected by oscillations. Another benefit of including cascades in the sample is that it might result in a stronger signal of ν_τ appearance.

There is also gain to be made by introducing new veto ideas. The veto algorithms presented are powerful, but end up reducing the signal by half. Developments on new techniques to identify classes of atmospheric muons could translate in an increase of the neutrino sample without reducing its quality. With more uncorrelated case-tailored variables it would not be necessary to cut hard on all of them.

Energy estimation

The current scheme for reconstructing the neutrino energy considers two secondary particles, which are fit individually. Ongoing studies have demonstrated that describing the neutrino interaction point in a single likelihood, which includes a track and a cascade, results in a 30 % improvement on the resolution. Moreover, it strongly suppresses misreconstructed events [143].

Detector related uncertainties

From the detection point of view, it has been demonstrated that reasonable variations of the description of the medium have very little impact in this particular analysis. In contrast, the overall light collection efficiency of the DOMs has a small but non-trivial impact. Internal studies within the IceCube Collaboration attempt to use individual muons to determine this properties to better accuracy. Minimally ionizing muons have a constant Cherenkov light emission (see Sec. 6.1.1), which allows for direct calibration of the DOMs. Future analyses of the data might benefit from these results.

Atmospheric neutrino flux

Even with one year of data, the spectral index of the atmospheric neutrino flux is of importance, compared to statistical uncertainties. Improvements on the knowledge of this quantity can come from (i) including more precise measurements of the cosmic ray composition and spectrum, from experiments like AMS [110], and (ii) implementing a more accurate modeling of the hadronic cross-sections, which could result from LHC measurements in the forward direction.

On the experimental side, the flux is being measured by IceCube itself, using different techniques and channels at slightly higher energies than this analysis. Even in the context of oscillation analyses, including a larger energy region can help in constraining the shape of the flux from the data.

Energy range covered

The very lowest energies that the detector can access were not used for this analysis. The accuracy of the reconstruction algorithms decreases with energy, which partly explains why they are removed. However, even if the reconstruction tools were improved, there is a limiting factor that comes from correctly modeling interactions below 10 GeV. The problem, as discussed at the end of Chapter 3, is that these interactions are not well understood. Improvements in the field could allow removing the restriction, and thus including a region where the oscillatory effect is changing rapidly. The transition region is of relevance to other

experiments as well. The MINERvA [131] and T2K [132] collaborations have recently published results on cross-section measurements at these energies. Although the measurements are still limited by the number of interactions collected, there is ongoing activity on the field.

Each one of the items listed is an active area of research, either within the IceCube Collaboration or others. As of the time of writing, real improvements on more than one of the topics mentioned have become available. It might very well be that the projections given in Fig. 8.6 will turn out to be rather conservative. The following section briefly looks back at the method developed, one of the main contributions of this work.

9 Summary and Outlook

The goals of this work were the identification of possibilities and challenges for neutrino oscillation studies with IceCube DeepCore and the development of tools and a strategy to perform a measurement. The results are a full reconstruction of neutrino interactions between $E_\nu = [10, 100]\,\text{GeV}$, and the definition of high quality events with reduced sensitivity to medium optical properties. The performance of both was tested in simulation and corroborated in data, giving satisfactory results.

The methods developed allowed to measure the disappearance pattern of muon neutrinos, focusing on the determination of θ_{23} and Δm^2_{32} in the energy range between 10 GeV and 100 GeV, exploiting the zenith and energy dependence of the effect. The results of the analysis, shown in Fig. 8.6, are compatible with the world's average and show a remarkable agreement between data and simulation. They contribute to the field, and point to a good understanding of the data.

Since the beginning of this work, the IceCube DeepCore detector has entered a stable phase. The detector has been operational for almost three years in its full configuration, and will continue taking data for at least three times that period. The understanding of the detector is improving continuously, together with novel ways of looking at the data. Combining this with the demonstration of its capabilities contained in this work assures that meaningful contributions to the field of neutrino oscillations, and other particle physics topics, will be made by the experiment.

The neutrino, as abundant as it is, is still the elementary particle about which we know the least. Its nature, absolute mass scale, correct mass ordering and whether it violates *CP* conservation are the unknowns that we are aware of. The study of neutrino oscillations can address the two latter ones, and much effort is being put by the community in this direction. The next generation of neutrino experiments being proposed contains either the mass ordering, *CP* violation, or both items as their main goals [158].

The IceCube detector could also contribute to the determination of the correct mass hierarchy. This, however, requires not only the tools described in this work, but also to lower the detector's energy threshold. The Precision IceCube Next Generation Upgrade (PINGU) [159] is a proposal along these lines, which seeks to deploy an additional array of sensors within the DeepCore subarray. Ongoing studies within the IceCube-PINGU effort indicate that effects from the mass hierarchy could be observed after three to five years of data.

Neutrino physics is moving towards precision measurements. The neutrino has already led us to reconsider our understanding of fundamental particles, and even quantum mechanics. There can be nothing but excitement in thinking about the other insights on Nature that it might give us.

Bibliography

[1] L. M. Brown. The idea of the neutrino. *Phys. Today*, 31:23, 1978.

[2] G. W. A. Newton. History of the Unraveling of the Natural Decay Series. *Radiochimica Acta*, 70/71:31–37, 1995.

[3] R. Lewin Sime. *Lise Meitner: A Life in Physics*. University of California Press, Berkeley, 1st edition, 1996.

[4] E. Fermi. Tentativo di una Teoria Dei Raggi β. *Nuovo Cimento*, 11(1):1–19, 1934. doi:10.1007/BF02959820.

[5] C. L. Cowan et al. Detection of the Free Neutrino: A Confirmation. *Science*, 124:103–104, 1956. doi:10.1126/science.124.3212.103.

[6] G. C. Hanna and B. Pontecorvo. The β-Spectrum of H^3. *Phys. Rev.*, 75:983–984, 1949. doi:10.1103/PhysRev.75.983.3.

[7] S. C. Curran, J. Angus, and A. L. Cockroft. The Beta-Spectrum of Tritium. *Phys. Rev.*, 76:853–854, 1949. doi:10.1103/PhysRev.76.853.

[8] L. Landau. On the conservation laws for weak interactions. *Nucl. Phys.*, 3(1):127 – 131, 1957. doi:10.1016/0029-5582(57)90061-5.

[9] A. Salam. On parity conservation and neutrino mass. *Nuovo Cimento*, 5:299–301, 1957. doi:10.1007/BF02812841.

[10] T. D. Lee and C. N. Yang. Parity Nonconservation and a Two-Component Theory of the Neutrino. *Phys. Rev.*, 105:1671–1675, 1957. doi:10.1103/PhysRev.105.1671.

[11] R. P. Feynman and M. Gell-Mann. Theory of the Fermi Interaction. *Phys. Rev.*, 109:193–198, 1958. doi:10.1103/PhysRev.109.193.

[12] E. C. G. Sudarshan and R. E. Marshak. Chirality Invariance and the Universal Fermi Interaction. *Phys. Rev.*, 109:1860–1862, 1958. doi:10.1103/PhysRev.109.1860.2.

[13] B. Pontecorvo. Inverse beta processes and nonconservation of lepton charge. *Sov. Phys. JETP*, 7:172–173, 1958.

[14] B. Pontecorvo. Mesonium and Antimesonium. *Sov. Phys. JETP*, 6:429, 1958.

[15] G. Danby et al. Observation of High-Energy Neutrino Reactions and the Existence of Two Kinds of Neutrinos. *Phys. Rev. Lett.*, 9:36–44, 1962. doi:10.1103/PhysRevLett.9.36.

[16] Z. Maki, M. Nakagawa, and S. Sakata. Remarks on the unified model of elementary particles. *Prog. Theor. Phys.*, 28:870–880, 1962. doi:10.1143/PTP.28.870.

[17] V. N. Gribov and B. Pontecorvo. Neutrino astronomy and lepton charge. *Phys. Lett.*, B28:493, 1969. doi:10.1016/0370-2693(69)90525-5.

[18] R. Davis et al. In *Proceedings of the Neutrino '72 Europhysics Conference*, volume 1, page 29, Baltonfuered, Hungary, 1972.

[19] D. N. Abdurashitov et al. Results from SAGE. *Phys. Lett.*, B328:234–248, 1994. doi:10.1016/0370-2693(94)90454-5.

[20] P. Anselmann et al. GALLEX Collaboration. GALLEX solar neutrino observations: The Results from GALLEX-I and early results from GALLEX-II. *Phys. Lett.*, B314:445–458, 1993. doi:10.1016/0370-2693(93)91264-N.

[21] K. S. Hirata et al. Kamiokande-II Collaboration. Constraints on neutrino oscillation parameters from the Kamiokande-II solar neutrino data. *Phys. Rev. Lett.*, 65:1301–1304, 1990. doi:10.1103/PhysRevLett.65.1301.

[22] R. L. Helmer et al. SNO Collaboration. First results from the sudbury neutrino observatory. *Nucl. Phys. B*, 111(1):122–127, 2002. doi:10.1016/S0920-5632(02)01693-6.

[23] F. Reines et al. Evidence for High-Energy Cosmic-Ray Neutrino Interactions. *Phys. Rev. Lett.*, 15:429–433, 1965. doi:10.1103/PhysRevLett.15.429.

[24] C. V. Achar et al. Detection of muons produced by cosmic ray neutrinos deep underground. *Phys. Lett.*, 18:196–199, 1965. doi:10.1016/0031-9163(65)90712-2.

[25] T. Kajita et al. Super-Kamiokande, Kamiokande Collaboration. Atmospheric neutrino results from Super-Kamiokande and Kamiokande: Evidence for neutrino(mu) oscillations. *Nucl. Phys. Proc. Suppl.*, 77:123–132, 1999, arXiv:hep-ex/9810001. doi:10.1016/S0920-5632(99)00407-7.

[26] T. Patzak et al. DONUT Collaboration. First direct observation of the tau-neutrino. *Europhys. News*, 32:56–57, 2001.

[27] D. Griffiths. *Introduction to elementary particles*. John Wiley & Sons, Inc, New York, 2008.

[28] C. Giunti and C. W. Kim. *Fundamentals of Neutrino Physics and Astrophysics*. Oxford University Press, Oxford, 2007.

[29] P. Hernandez. Neutrino physics. 2010, arXiv:1010.4131.

[30] J. Beringer et al. Particle Data Group. Review of Particle Physics (RPP). *Phys. Rev.*, D86:010001, 2012 and 2013 partial update for the 2014 edition. doi:10.1103/PhysRevD.86.010001.

[31] S. Schael et al. ALEPH, DELPHI, L3 , OPAL, SLD, LEP Electroweak Working Group, SLD Electroweak Group, SLD Heavy Flavour Group Collaboration. Precision electroweak measurements on the Z resonance. *Phys. Rept.*, 427:257–454, 2006, arXiv:hep-ex/0509008. doi:10.1016/j.physrep.2005.12.006.

[32] M. Goldhaber, L. Grodzins, and A. W. Sunyar. Helicity of neutrinos. *Phys. Rev.*, 109:1015–1017, 1958. doi:10.1103/PhysRev.109.1015.

[33] C. Kraus et al. Final results from phase II of the Mainz neutrino mass searchin tritium β decay. *Eur. Phys. J. C*, 40(4):447–468, 2005. doi:10.1140/epjc/s2005-02139-7.

[34] V. N. Aseev et al. Upper limit on the electron antineutrino mass from the Troitsk experiment. *Phys. Rev. D*, 84:112003, 2011. doi:10.1103/PhysRevD.84.112003.

[35] G. Drexlin et al. Current Direct Neutrino Mass Experiments. 2013, arXiv:1307.0101.

[36] K. N. Abazajian et al. Cosmological and Astrophysical Neutrino Mass Measurements. *Astropart. Phys.*, 35:177–184, 2011, arXiv:1103.5083. doi:10.1016/j.astropartphys.2011.07.002.

[37] J. A. Formaggio and G. P. Zeller. From eV to EeV: Neutrino Cross Sections Across Energy Scales. *Rev. Mod. Phys.*, 84:1307, 2012, arXiv:1305.7513.

[38] J. Feltesse. Introduction to Parton Distribution Functions. *Scholarpedia*, 5(11):10160, 2010. doi:10.4249/scholarpedia.10160.

[39] E. Majorana and L. Maiani. A symmetric theory of electrons and positrons. In G. Bassani, editor, *Ettore Majorana Scientific Papers*, pages 201–233. Springer, 2006.

[40] C. Giunti. Neutrino wave packets in quantum field theory. *J. High Energy Phys.*, 0211:017, 2002, arXiv:hep-ph/0205014. doi:10.1088/1126-6708/2002/11/017.

[41] B. Kayser. On the quantum mechanics of neutrino oscillation. *Phys. Rev. D*, 24:110–116, 1981. doi:10.1103/PhysRevD.24.110.

[42] J. Rich. The Quantum mechanics of neutrino oscillations. *Phys. Rev.*, D48:4318–4325, 1993. doi:10.1103/PhysRevD.48.4318.

[43] E. K. Akhmedov. Do charged leptons oscillate? *J. High Energy Phys.*, 0709:116, 2007, arXiv:0706.1216. doi:10.1088/1126-6708/2007/09/116.

[44] C. Giunti and C. W. Kim. Quantum mechanics of neutrino oscillations. *Found. Phys. Lett.*, 14:213–229, 2001, arXiv:hep-ph/0011074. doi:10.1023/A:1012230026160.

[45] S. Nussinov. Solar neutrinos and neutrino mixing. *Phys. Lett.*, B63:201–203, 1976.

[46] Boris Kayser et al. On a theory of neutrino oscillations with entanglement. *Phys. Rev.*, D82:093003, 2010, arXiv:1006.2372. doi:10.1103/PhysRevD.82.093003.

[47] Evgeny Kh. Akhmedov and Joachim Kopp. Neutrino oscillations: Quantum mechanics vs. quantum field theory. *J. High Energy Phys.*, 1004:008, 2010, arXiv:1001.4815. doi:10.1007/JHEP04(2010)008, 10.1007/JHEP10(2013)052.

[48] S. Bilenky. *Introduction to the Physics of Massive and Mixed Neutrinos.* Springer, Heidelberg, 2010.

[49] L. Wolfenstein. Neutrino oscillations in matter. *Phys. Rev. D*, 17:2369–2374, 1978. doi:10.1103/PhysRevD.17.2369.

[50] F. J. Botella, C. S. Lim, and W. J. Marciano. Radiative Corrections to Neutrino Indices of Refraction. *Phys. Rev.*, D35:896, 1987. doi:10.1103/PhysRevD.35.896.

[51] T. Ohlsson and H. Snellman. Three flavor neutrino oscillations in matter. *J. Math. Phys.*, 41:2768–2788, 2000, arXiv:hep-ph/9910546. doi:10.1063/1.533270.

[52] M. Blennow and A. Smirnov. Neutrino propagation in matter. *Adv. High Energy Phys.*, 2013:972485, 2013, arXiv:1306.2903. doi:10.1155/2013/972485.

[53] M.C. Banuls, G. Barenboim, and J. Bernabeu. Medium effects for terrestrial and atmospheric neutrino oscillations. *Phys. Lett.*, B513:391–400, 2001, arXiv:hep-ph/0102184. doi:10.1016/S0370-2693(01)00723-7.

[54] S. Mikheyev and A. Smirnov. Resonant amplification of $\hat{\mathrm{I}}\frac{1}{2}$ oscillations in matter and solar-neutrino spectroscopy. *Nuovo Cimento*, 9(1):17–26, 1986. doi:10.1007/BF02508049.

[55] S. Mikheev and A. Smirnov. Resonance Amplification of Oscillations in Matter and Spectroscopy of Solar Neutrinos. *Sov. J. Nucl. Phys.*, 42:913–917, 1985.

[56] M. Freund and T. Ohlsson. Matter enhanced neutrino oscillations with a realistic earth density profile. *Mod. Phys. Lett.*, A15:867–874, 2000, arXiv:hep-ph/9909501. doi:10.1016/S0217-7323(00)00086-4.

[57] P. I. Krastev and A. Y. Smirnov. Parametric effects in neutrino oscillations. *Phys. Lett.*, B226:341–346, 1989. doi:10.1016/0370-2693(89)91206-9.

[58] E. K. Akhmedov. Parametric resonance in neutrino oscillations in matter. *Pramana*, 54:47–63, 2000, arXiv:hep-ph/9907435. doi:10.1007/s12043-000-0006-4.

[59] E. K. Akhmedov. Neutrino oscillations: Theory and phenomenology. *Nucl. Phys. Proc. Suppl.*, 221:19–25, 2011, arXiv:hep-ph/0610064. doi:10.1016/j.nuclphysbps.2011.03.086.

[60] G. L. Fogli et al. Global analysis of neutrino masses, mixings and phases: entering the era of leptonic CP violation searches. *Phys.Rev.*, D86:013012, 2012, arXiv:1205.5254. doi:10.1103/PhysRevD.86.013012.

[61] K. Kodama et al. DONUT Collaboration. Final tau-neutrino results from the DONuT experiment. *Phys. Rev. D*, D78:052002, 2008, arXiv:0711.0728. doi:10.1103/PhysRevD.78.052002.

[62] Y. Fukuda et al. Super-Kamiokande Collaboration. The Super-Kamiokande detector. *Nucl. Instrum. Methods*, A501:418–462, 2003. doi:10.1016/S0168-9002(03)00425-X.

[63] K. Abe et al. Super-Kamiokande Collaboration. A Measurement of the Appearance of Atmospheric Tau Neutrinos by Super-Kamiokande. *Phys. Rev. Lett.*, 110:181802, 2013, arXiv:1206.0328. doi:10.1103/PhysRevLett.110.181802.

[64] A. Himmel. Super-Kamiokande Collaboration. Recent Atmospheric Neutrino Results from Super-Kamiokande. In *7th International Conference on Interconnection between Particle Physics and Cosmology (PPC 2013)*, 2013, arXiv:1310.6677.

[65] D. G. Michael et al. MINOS Collaboration. Observation of muon neutrino disappearance with the MINOS detectors and the NuMI neutrino beam. *Phys. Rev. Lett.*, 97:191801, 2006, arXiv:hep-ex/0607088. doi:10.1103/PhysRevLett.97.191801.

[66] S. van der Meer. A directive device for charged particles and its use in an enhanced neutrino beam. 1961. doi:10.5170/CERN-1961-007.

[67] P. Adamson et al. MINOS Collaboration. Measurement of Neutrino and Antineutrino Oscillations Using Beam and Atmospheric Data in MINOS. *Phys. Rev. Lett.*, 110:251801, 2013, arXiv:1304.6335. doi:10.1103/PhysRevLett.110.251801.

[68] K. Abe et al. T2K Collaboration. The T2K experiment. *Nucl. Instrum. Methods A*, 659:106–135, 2011, arXiv:1106.1238. doi:10.1016/j.nima.2011.06.067.

[69] M. Apollonio et al. CHOOZ Collaboration. Search for neutrino oscillations on a long baseline at the CHOOZ nuclear power station. *Eur. Phys. J.*, C27:331–374, 2003, arXiv:hep-ex/0301017. doi:10.1140/epjc/s2002-01127-9.

[70] K. Abe et al. T2K Collaboration Collaboration. Evidence of Electron Neutrino Appearance in a Muon Neutrino Beam. *Phys. Rev.*, D88:032002, 2013, arXiv:1304.0841. doi:10.1103/PhysRevD.88.032002.

[71] R. Acquafredda et al. OPERA Collaboration. The OPERA experiment in the CERN to Gran Sasso neutrino beam. *J. Instrum.*, 4:P04018, 2009. doi:10.1088/1748-0221/4/04/P04018.

[72] S. Amerio et al. ICARUS Collaboration Collaboration. Design, construction and tests of the ICARUS T600 detector. *Nucl. Instrum. Methods*, A527:329–410, 2004. doi:10.1016/j.nima.2004.02.044.

[73] N. Agafonova et al. OPERA Collaboration. Observation of a first ν_τ candidate in the OPERA experiment in the CNGS beam. *Phys. Lett.*, B691:138–145, 2010, arXiv:1006.1623. doi:10.1016/j.physletb.2010.06.022.

[74] E. Medinaceli for the Opera Collaboration. Latest results of the OPERA experiment. Presented at the XXIV Workshop on Weak Interactions and Neutrinos, Natal, Brazil, 2013.

[75] J. Boger et al. SNO Collaboration. The Sudbury neutrino observatory. *Nucl. Instrum. Methods*, A449:172–207, 2000, arXiv:nucl-ex/9910016. doi:10.1016/S0168-9002(99)01469-2.

[76] B. Aharmim et al. SNO Collaboration. Electron energy spectra, fluxes, and day-night asymmetries of B-8 solar neutrinos from measurements with NaCl dissolved in the heavy-water detector at the Sudbury Neutrino Observatory. *Phys. Rev.*, C72:055502, 2005, arXiv:nucl-ex/0502021. doi:10.1103/PhysRevC.72.055502.

[77] J. Bahcall, A. Serenelli, and S. Basu. New solar opacities, abundances, helioseismology, and neutrino fluxes. *Astrophys. J.*, 621:L85–L88, 2005, arXiv:astro-ph/0412440. doi:10.1086/428929.

[78] Alimonti G. et al. Borexino Collaboration. The Borexino detector at the Laboratori Nazionali del Gran Sasso. *Nucl. Instrum. Methods A*, 600:568–593, 2009, arXiv:0806.2400. doi:10.1016/j.nima.2008.11.076.

[79] G. Bellini et al. Borexino Collaboration. Final results of Borexino Phase-I on low energy solar neutrino spectroscopy. 2013, arXiv:1308.0443.

[80] S. A. Dazeley. KamLAND Collaboration. An Update on progress at KamLAND. 2002, arXiv:hep-ex/0205041.

[81] T. Araki et al. KamLAND Collaboration. Experimental investigation of geologically produced antineutrinos with KamLAND. *Nature*, 436:499–503, 2005. doi:10.1038/nature03980.

[82] K. Ichimura. KamLAND Collaboration. Recent Results from KamLAND. Presented at ICHEP08, Philadelphia, USA, 2008, arXiv:0810.3448.

[83] C. Bemporad. CHOOZ Collaboration. A Long-Base Search for Neutrino Oscillations at a Reactor; the CHOOZ Experiment. In D. Lellouch, G. Mikenberg, and E. Rabinovici, editors, *International Europhysics Conference on High Energy Physics*, pages 834–839. Springer, 1999.

[84] G. Mention. Double-Chooz: A search for Theta(13). *Nucl. Phys. Proc. Suppl.*, 145:182–185, 2005. doi:10.1016/j.nuclphysbps.2005.04.002.

[85] X. Guo et al. Daya-Bay Collaboration. A precision measurement of the neutrino mixing angle θ_{13} using reactor antineutrinos at Daya-Bay. 2007, arXiv:hep-ex/0701029.

[86] J. K. Ahn et al. RENO Collaboration. RENO: An Experiment for Neutrino Oscillation Parameter θ_{13} Using Reactor Neutrinos at Yonggwang. 2010, arXiv:1003.1391.

[87] H. Minakata. If θ_{13} is large, then what? *J. Phys. Conf. Ser.*, 408:012034, 2013, arXiv:1110.4237. doi:10.1088/1742-6596/408/1/012034.

[88] F. P. An et al. Daya-Bay Collaboration. Observation of Electron-Antineutrino Disappearance at Daya Bay. *Phys. Rev. Lett.*, 108:171803, 2012. doi:10.1103/PhysRevLett.108.171803.

[89] J. K. Ahn et al. RENO Collaboration. Observation of Reactor Electron Antineutrinos Disappearance in the RENO Experiment. *Phys. Rev. Lett.*, 108:191802, 2012. doi:10.1103/PhysRevLett.108.191802.

[90] B. Pontecorvo. Neutrino Experiments and the Problem of Conservation of Leptonic Charge. *Sov. Phys. JETP*, 26:984–988, 1968.

[91] K. N. Abazajian et al. Light Sterile Neutrinos: A White Paper. 2012, arXiv:1204.5379.

[92] C. Giunti and M. Laveder. Statistical Significance of the Gallium Anomaly. *Phys. Rev.*, C83:065504, 2011, arXiv:1006.3244. doi:10.1103/PhysRevC.83.065504.

[93] H. Kwon et al. Search for Neutrino Oscillations at a Fission Reactor. *Phys. Rev.*, D24:1097–1111, 1981. doi:10.1103/PhysRevD.24.1097.

[94] G. Zacek et al. CALTECH-SIN-TUM COLLABORATION Collaboration. Neutrino Oscillation Experiments at the Gosgen Nuclear Power Reactor. *Phys. Rev.*, D34:2621–2636, 1986. doi:10.1103/PhysRevD.34.2621.

[95] A. A. Kuvshinnikov et al. Measuring the anti-electron-neutrino + p $\rightarrow$ n + e+ cross-section and beta decay axial constant in a new experiment at Rovno NPP reactor. (In Russian). *JETP Lett.*, 54:253–257, 1991.

[96] G. S. Vidyakin et al. Limitations on the characteristics of neutrino oscillations. *JETP Lett.*, 59:390–393, 1994.

[97] Z. D. Greenwood et al. Results of a two position reactor neutrino oscillation experiment. *Phys. Rev.*, D53:6054–6064, 1996. doi:10.1103/PhysRevD.53.6054.

[98] Y. Declais et al. Study of reactor anti-neutrino interaction with proton at Bugey nuclear power plant. *Phys. Lett.*, B338:383–389, 1994. doi:10.1016/0370-2693(94)91394-3.

[99] T. A. Mueller et al. Improved Predictions of Reactor Antineutrino Spectra. *Phys. Rev.*, C83:054615, 2011, arXiv:1101.2663. doi:10.1103/PhysRevC.83.054615.

[100] G. Mention et al. The Reactor Antineutrino Anomaly. *Phys. Rev.*, D83:073006, 2011, arXiv:1101.2755. doi:10.1103/PhysRevD.83.073006.

[101] C. Athanassopoulos et al. LSND Collaboration. Evidence for anti-muon-neutrino to anti-electron-neutrino oscillations from the LSND experiment at LAMPF. *Phys. Rev. Lett.*, 77:3082–3085, 1996, arXiv:nucl-ex/9605003. doi:10.1103/PhysRevLett.77.3082.

[102] B. Armbruster et al. KARMEN Collaboration. Upper limits for neutrino oscillations muon-anti-neutrino to electron-anti-neutrino from muon decay at rest. *Phys. Rev.*, D65:112001, 2002, arXiv:hep-ex/0203021. doi:10.1103/PhysRevD.65.112001.

[103] E. D. Church et al. Statistical analysis of different muon-anti-neutrino to electron-anti-neutrino searches. *Phys. Rev.*, D66:013001, 2002, arXiv:hep-ex/0203023. doi:10.1103/PhysRevD.66.013001.

[104] C. Giunti and M. Laveder. 3+1 and 3+2 Sterile Neutrino Fits. *Phys. Rev.*, D84:073008, 2011, arXiv:1107.1452. doi:10.1103/PhysRevD.84.073008.

[105] J. M. Conrad et al. Sterile Neutrino Fits to Short Baseline Neutrino Oscillation Measurements. *Adv. High Energy Phys.*, 2013:163897, 2013, arXiv:1207.4765. doi:10.1155/2013/163897.

[106] R. Dharmapalan et al. MiniBooNE+ Collaboration. A new investigation of electron neutrino appearance oscillations with improved sensitivity in the MiniBooNE+ experiment. In *Snowmass 2013 Proceedings*, 2013, arXiv:1310.0076.

[107] M. Wallraff for the IceCube Collaboration. Search for sterile neutrinos with the IceCube Neutrino Observatory. In *International Cosmic Ray Conference*, 2013, arXiv:1309.7008.

[108] T. K. Gaisser. Cosmic rays and particle physics. *Comments Nucl. Part. Phys.*, 11:25, 1982.

[109] M. Ackermann et al. Fermi-LAT Collaboration. Detection of the Characteristic Pion-Decay Signature in Supernova Remnants. *Science*, 339:807, 2013, arXiv:1302.3307. doi:10.1126/science.1231160.

[110] S. Haino for the AMS Collaboration. Precision measurement of the proton flux with AMS. In *International Cosmic Ray Conference*, 2013.

[111] C. Wiebusch. *The Detection of faint light in deep underwater neutrino telescopes*. PhD thesis, Rheinisch-Westfaelische Technische Hochschule (RWTH) Aachen, 1995.

[112] M. Honda et al. Calculation of atmospheric neutrino flux using the interaction model calibrated with atmospheric muon data. *Phys. Rev.*, D75:043006, 2007, arXiv:astro-ph/0611418. doi:10.1103/PhysRevD.75.043006.

[113] G. D. Barr et al. A Three - dimensional calculation of atmospheric neutrinos. *Phys. Rev.*, D70:023006, 2004, arXiv:astro-ph/0403630. doi:10.1103/PhysRevD.70.023006.

[114] G. Battistoni et al. The FLUKA atmospheric neutrino flux calculation. *Astropart. Phys.*, 19:269–290, 2003, arXiv:hep-ph/0207035. doi:10.1016/S0927-6505(02)00246-3.

[115] R. Enberg, M. Reno, and I. Sarcevic. Prompt neutrino fluxes from atmospheric charm. *Phys. Rev.*, D78:043005, 2008, arXiv:0806.0418. doi:10.1103/PhysRevD.78.043005.

[116] M. G. Aartsen et al. IceCube Collaboration. Measurement of the Atmospheric ν_e flux in IceCube. *Phys. Rev. Lett.*, 110:151105, 2013, arXiv:1212.4760. doi:10.1103/PhysRevLett.110.151105.

[117] A. Achterberg et al. IceCube Collaboration. First Year Performance of The IceCube Neutrino Telescope. *Astropart. Phys.*, 26:155–173, 2006, arXiv:astro-ph/0604450. doi:10.1016/j.astropartphys.2006.06.007.

[118] R. Abbasi et al. IceCube Collaboration. The Design and Performance of IceCube DeepCore. *Astropart. Phys.*, 35:615–624, 2012, arXiv:1109.6096. doi:10.1016/j.astropartphys.2012.01.004.

[119] K. Hanson and O. Tarasova. IceCube Collaboration. Design and production of the IceCube digital optical module. *Nucl. Instrum. Methods*, A567:214–217, 2006. doi:10.1016/j.nima.2006.05.091.

[120] R. Abbasi et al. IceCube Collaboration. Calibration and Characterization of the IceCube Photomultiplier Tube. *Nucl. Instrum. Methods*, A618:139–152, 2010, arXiv:1002.2442. doi:10.1016/j.nima.2010.03.102.

[121] R. Abbasi et al. The IceCube data acquisition system: Signal capture, digitization, and timestamping. *Nucl. Instrum. Methods A*, 601:294–316, 2009, arXiv:0810.4930. doi:10.1016/j.nima.2009.01.001.

[122] C. Wiebusch. IceCube Collaboration Collaboration. Physics Capabilities of the IceCube DeepCore Detector. In *International Cosmic Ray Conference*, 2009, arXiv:0907.2263.

[123] M. Ackermann et al. IceCube Collaboration. Optical properties of deep glacial ice at the South Pole. *J. Geophys. Res.*, 111(D10):13203, 2006. doi:10.1029/2005JD006687.

[124] M. G. Aartsen et al. IceCube Collaboration. Measurement of South Pole ice transparency with the IceCube LED calibration system. *Nucl. Instrum. Methods*, A711:73–89, 2013, arXiv:1301.5361. doi:10.1016/j.nima.2013.01.054.

[125] S. Agarwalla et al. Exploring the Earth matter effect with atmospheric neutrinos in ice. 2012, arXiv:1212.2238.

[126] E. Kh. Akhmedov, S. Razzaque, and A. Yu. Smirnov. Mass hierarchy, 2-3 mixing and CP-phase with Huge Atmospheric Neutrino Detectors. *J. High Energy Phys.*, 1302:082, 2013, arXiv:1205.7071. doi:10.1007/JHEP02(2013)082, 10.1007/JHEP07(2013)026.

[127] G. Giordano, O. Mena, and I. Mocioiu. Atmospheric neutrino oscillations and tau neutrinos in ice. *Phys. Rev.*, D81:113008, 2010, arXiv:1004.3519. doi:10.1103/PhysRevD.81.113008.

[128] K. Daum et al. Frejus Collaboration. Determination of the atmospheric neutrino spectra with the Frejus detector. *Z. Phys.*, C66:417–428, 1995. doi:10.1007/BF01556368.

[129] M. Sajjad Athar et al. Atmospheric neutrino flux at INO, South Pole and Pyhásalmi. *Phys. Lett.*, B718:1375–1380, 2013, arXiv:1210.5154. doi:10.1016/j.physletb.2012.12.016.

[130] C. Andreopoulos et al. The GENIE Neutrino Monte Carlo Generator. *Nucl. Instrum. Methods*, A614:87–104, 2010, arXiv:0905.2517. doi:10.1016/j.nima.2009.12.009.

[131] L. Fields et al. MINERvA Collaboration. Measurement of Muon Antineutrino Quasi-Elastic Scattering on a Hydrocarbon Target at $E_\nu \sim 3.5$ GeV. *Phys. Rev. Lett.*, 111:022501, 2013, arXiv:1305.2234. doi:10.1103/PhysRevLett.111.022501.

[132] K. Abe et al. T2K Collaboration. Measurement of the Inclusive NuMu Charged Current Cross Section on Carbon in the Near Detector of the T2K Experiment. *Phys. Rev.*, D87:092003, 2013, arXiv:1302.4908. doi:10.1103/PhysRevD.87.092003.

[133] D. Heck et al. *CORSIKA: a Monte Carlo code to simulate extensive air showers.* Forschungszentrum Karlsruhe GmbH, 1998. http://inspirehep.net/record/469835/files/FZKA6019.pdf.

[134] R. S. Fletcher et al. SIBYLL: An event generator for simulation of high-energy cosmic ray cascades. *Phys. Rev.*, D50:5710–5731, 1994. doi:10.1103/PhysRevD.50.5710.

[135] D. Chirkin and W. Rhode. Muon Monte Carlo: A High-precision tool for muon propagation through matter. 2004, arXiv:hep-ph/0407075.

[136] S. Agostinelli et al. Geant4 - a simulation toolkit. *Nucl. Instrum. Methods A*, 506(3):250 – 303, 2003. doi:10.1016/S0168-9002(03)01368-8.

[137] L. Raedel. Simulation Studies of the Cherenkov Light Yield from Relativistic Particles in High-Energy Neutrino Telescopes with Geant4. Master's thesis, Rheinisch-Westfaelische Technische Hochschule (RWTH) Aachen, 2012.

[138] M. Kowalski. *Search for neutrino-induced cascades with the AMANDA-II detector.* PhD thesis, Humboldt Univerzität zu Berlin, 2004. http://edoc.hu-berlin.de/docviews/abstract.php?id=10715.

[139] I. Tamm. Radiation emitted by uniformly moving electrons. In B. Bolotovskii, V. Frenkel, and R. Peierls, editors, *Selected Papers*, pages 37–53. Springer Berlin Heidelberg, 1991.

[140] C. James and M. Pleinert. ECAP. Private communication.

[141] T. A. Gabriel et al. Energy dependence of hadronic activity. *Nucl. Instrum. Methods*, A338:336–347, 1994. doi:10.1016/0168-9002(94)91317-X.

[142] J. A. Aguilar et al. ANTARES Collaboration. A fast algorithm for muon track reconstruction and its application to the ANTARES neutrino telescope. *Astropart. Phys.*, 34:652–662, 2011, arXiv:1105.4116. doi:10.1016/j.astropartphys.2011.01.003.

[143] A. Terliuk. IceCube Collaboration. Energy reconstruction of ν_μ events in DeepCore . Internal report, DESY, 2013. Master's thesis in preparation.

[144] S. Euler for the IceCube Collaboration. Atmospheric neutrino oscillations with DeepCore. In *International Cosmic Ray Conference*, volume 4, page 67, 2011.

[145] M.G. Aartsen et al. IceCube Collaboration. Energy Reconstruction Methods in the IceCube Neutrino Telescope. 2013, arXiv:1311.4767.

[146] T. Messarius for the IceCube Collaboration. A software trigger for the AMANDA neutrino detector. In *International Cosmic Ray Conference*, volume 4, page 56, 2005, arXiv:astro-ph/0509330.

[147] O. Schulz. *The design study of IceCube DeepCore: Characterization and veto studies.* PhD thesis, Ruperto-Carola-University of Heidelberg, 2010.

[148] M. G. Aartsen et al. IceCube Collaboration Collaboration. The IceCube Neutrino Observatory Part IV: Searches for Dark Matter and Exotic Particles. In *International Cosmic Ray Conference*, 2013, arXiv:1309.7007.

[149] S. Euler. *Observations of Oscillations of Atmospheric Neutrinos with the IceCube Neutrino Observatory.* PhD thesis, Rheinisch-Westfaelische Technische Hochschule (RWTH) Aachen, 2013.

[150] J. Ahrens et al. AMANDA Collaboration. Muon track reconstruction and data selection techniques in AMANDA. *Nucl. Instrum. Methods*, A524:169–194, 2004, arXiv:astro-ph/0407044. doi:10.1016/j.nima.2004.01.065.

[151] M. G. Aartsen et al. IceCube Collaboration. Measurement of Atmospheric Neutrino Oscillations with IceCube. *Phys. Rev. Lett.*, 111:081801, 2013, arXiv:1305.3909. doi:10.1103/PhysRevLett.111.081801.

[152] N. Reid. Likelihood Inference in the Presence of Nuisance Parameters, arXiv:0312079.

[153] F. James and M. Roos. Minuit: A System for Function Minimization and Analysis of the Parameter Errors and Correlations. *Comput. Phys. Commun.*, 10:343–367, 1975. doi:10.1016/0010-4655(75)90039-9.

[154] S. S. Wilks. The Large-Sample Distribution of the Likelihood Ratio for Testing Composite Hypotheses. *Annals Math. Statist.*, 9(1):60–62, 1938. doi:10.1214/aoms/1177732360.

[155] G. Feldman and R. Cousins. A Unified approach to the classical statistical analysis of small signals. *Phys. Rev.*, D57:3873–3889, 1998, arXiv:physics/9711021. doi:10.1103/PhysRevD.57.3873.

[156] K. Abe et al. T2K Collaboration. Measurement of Neutrino Oscillation Parameters from Muon Neutrino Disappearance with an Off-axis Beam. *Phys. Rev. Lett.*, 211803, 2013, arXiv:1308.0465. doi:10.1103/PhysRevLett.111.211803.

[157] S. Adrian-Martinez et al. ANTARES Collaboration. Measurement of Atmospheric Neutrino Oscillations with the ANTARES Neutrino Telescope. *Phys. Lett.*, B714:224–230, 2012, arXiv:1206.0645. doi:10.1016/j.physletb.2012.07.002.

[158] M. Blennow et al. Quantifying the sensitivity of oscillation experiments to the neutrino mass ordering. 2013, arXiv:1311.1822.

[159] M. G. Aartsen et al. IceCube-PINGU Collaboration. PINGU Sensitivity to the Neutrino Mass Hierarchy. In *Snowmass 2013 Proceedings*, 2013, arXiv:1306.5846.

List of Figures

List of Tables

Acknowledgments

The work contained in these pages would have not been possible without the guidance and support of my advisor in DESY, Rolf Nahnhauer. His experience as an experimentalist and his involvement were crucial at all stages of this thesis. My gratitude goes to him and to Christian Spiering for giving me the chance to be part of the IceCube group at DESY. Also, I would like to thank Hermann Kolanoski for his supervision, in particular on the later stages of this work.

Special thanks go to Juergen Brunner. Many of the essential ideas used in this study were developed by him for the ANTARES detector. It was his initiative to transfer this knowledge to IceCube, with very satisfactory results.

I whish to express my gratitude to the IceCube group at DESY for their technical advise. Also to my colleagues from the IceCube Collaboration for their valuable input on analysis methods.

Many thanks to those who read, corrected and made suggestions to improve this thesis: Rolf Nahnhauer, Hermann Kolanoski, Meike de With, Alexandra Parascho, David Altmann, Thorsten Gluesenkamp, Angel Cruz, Achim Stoessl, Lars Mohrmann and Timo Karg. I cannot imagin how I could have done this without your help.

On a last personal note, I want to thank my family and friends whom, even if far away, always supported me.

I would also like to acknowledge the financial support from the Consejo Nacional de Ciencia y Tecnología (CONACYT) from Mexico and the Sonderforschungsbereich SFB 676 in Hamburg.

Selbständigkeitserklärung

Ich erkläre, dass ich die vorliegende Arbeit selbständig und nur unter Verwendung der angegebenen Literatur und Hilfsmittel angefertigt habe.

Berlin, den 11.02.2014 Juan Pablo Yáñez Garza